

Modeling and Analysis of a Class of Linear Reluctance Actuators for Advanced Precision Motion Systems

by

Michael Pumphrey

A thesis submitted to the Department of Mechanical Engineering

in partial fulfilment of the requirements for the degree of

Master of *Engineering*

at the

Memorial University of Newfoundland

May 2023

Supervisor: Dr. Mohammad Al Janaideh

St. John's

Newfoundland

Abstract

Reluctance actuators (RA) are a type of electromagnetic actuator that offer high forces for short range motions. The RA takes advantage of the electromagnetic reluctance force property in air gaps between the stator core and mover parts. The mover accelerates because the stator generates the magnetic flux that produces an attractive magnetic attraction between the stator and mover. Hysteresis and other non-linearities in the magnetic flux have an impact on the force and have a nonlinear gap dependency. It is demonstrated that the RA has the capacity to produce a force that is effective and suitable for millimeter-range high-acceleration applications. One application for the RA is the short-stroke stage of photolithography machines for example. The RA is available in a wide variety of configurations, such as C-Core, E-Core, Maxwell, and Plunger-type designs. The RA requires precise dynamic models and control algorithms to help linearize the RA for better control and optimization. Some nonlinear dynamics include magnetic hysteresis, flux fringing, and eddy currents. The RA is shown to have a much higher force density than any other traditional actuator, with the main disadvantage being the nonlinear and hysteretic behaviour which makes it hard to control without proper dynamic and control models in place. It is important to model the RA accurately for better control. The output

force can be significantly impacted by unequal offsets or asymmetries between the mover and stator. In the thesis that follows, a review of RA systems is performed, an investigation that shows the importance of including the mean path length (MPL) term for higher accuracy, a technique for calculating the force of various asymmetrical instances for the C-core RA is demonstrated. This thesis documents currently available knowledge of the RA such as available applications, configurations, dynamic models, measurement systems, and control systems for the RA. The findings presented can allow for future control systems to be designed to counteract multi-axial asymmetric issues of the RA.

Acknowledgements

Without a few people, this work would not have existed, thus I would like to thank them. My sincere thanks go out to my supervisor, Professor Mohammad Al Janaideh, who have supported me, mentored me, and helped me grow academically. You were constantly at my side, ready to assist, encourage, and remove any obstacles that would have prevented me. No amount of thanks will do.

I want to thank Professor Geoff Rideout for giving me the greatest knowledge, resources, and expertise. You also introduced me to fresh concepts that I may use to further in my study. Being a student in your classes has always been an honour for me.

I also want to thank Dr. Natheer Alatawneh who provided his expert knowledge in magnetics and mechatronics to help guide our team on technical matters. He was always available for questions and provided excellent feedback to help out in the publishing of our articles. Thanks for all your help.

I would want to convey my gratitude to Memorial University of Newfoundland

for providing all the necessary tools for us to carry out our research to the highest standards.

My parents, who I will always have my deepest gratitude for their unending support. I appreciate you helping me understand the importance of education and supporting me at every turn. You mean the world to me; thank you for your blessings and unwavering love.

Last but not least, I want to thank my girlfriend and daughter since they are the real drivers of all of my research's successes. You support me when things are tough. I dedicate this work to them in thanks for all that they have done.

— Michael Pumphrey May 2023

Contents

Abstract	ii
Acknowledgements	iv
List of Symbols and Abbreviations	x
List of Tables	xiv
List of Figures	xvi
1 Introduction & Background	1
1.1 Main Objectives & Motivations	5
1.2 Thesis Outcomes & Contributions	6
1.3 Thesis Outline	6
2 Review of Modeling and Control of Linear Reluctance Actuators in Precision Motion Systems	7
2.1 Available Applications	7
2.2 Configurations of RA	9
2.2.1 C-Core	9

2.2.2	E-Core	11
2.2.3	Plunger	12
2.2.4	Maxwell	12
2.2.5	Hybrid	14
2.2.6	Additional Components	15
2.2.7	Core & Mover Material	17
2.2.8	Thermal Management	18
2.3	Available Dynamic Models of RA	19
2.3.1	Flux Fringing & Eddy Current Considerations	21
2.3.2	Design Considerations	23
2.3.3	Finite Element Modeling Methods	27
2.4	Available Measurement Systems	28
2.4.1	Flux Sensing	28
2.4.2	Force Sensing	31
2.4.3	Acceleration Sensing	33
2.4.4	Position Sensing	34
2.5	Available Control Systems	38
2.5.1	Feedforward and Feedback	38
2.5.1.1	Current Sensing	38
2.5.1.2	Gap Sensing	39
2.5.1.3	Flux Sensing	40
2.5.1.4	Force Sensing	42
2.5.2	Controller Algorithm & Identification	43
2.5.3	Feedback Linearization	50

2.5.4	Iterative Learning Control	51
2.5.5	Hysteresis Considerations	52
2.6	Discussion	55
2.7	Conclusions of the Chapter	56
3	Investigating the effect of the Mean Path Length on RA Output	
	Force Characterization	58
3.1	Introduction	59
3.2	Modeling of RA	61
3.2.1	C-Core RA	61
3.2.2	E-Core RA	63
3.3	Results and Discussion	65
3.3.1	Simulation results	66
3.3.2	Simulation Results Discussion	71
3.3.3	Experimental Results	72
3.4	Conclusions of the Chapter	75
4	Modeling and Analysis with	
	Asymmetrical Air Gaps	77
4.1	Introduction	78
4.2	Analytical Model	79
4.2.1	Case 0 Derivation	80
4.2.2	Case 1 Derivation	81
4.2.3	Case 2 Derivation	84
4.2.4	Case 3 Derivation	85

4.3	Simulation Results	87
4.3.1	Case 0	87
4.3.2	Case 1	89
4.3.3	Case 2	90
4.3.4	Case 3	92
4.3.5	Case 0F	93
4.3.6	Case 1+2	94
4.3.7	Case 1+2+3	96
4.4	Experimental Design	97
4.5	Discussion	103
4.6	Conclusions of this Chapter	105
5	Conclusions and Future Work	107
	Bibliography	110
A	Configurations and Setups of the Reluctance Actuator Examples	128

List of Symbols and Abbreviations

RA	Reluctance Actuator
FEA	Finite Element Analysis
AC	Alternating Current
ILC	Iterative Learning Control
MPL	Mean Path Length
DOF	Degrees of Freedom
DC	Direct Current
CoFe	Cobalt-Iron
MEC	Magnetic Equivalent Circuit
FEM	Finite Element Method
MR	Magnetoresistive
GMR	Giant Magnetoresistive
FPGA	Field-Programmable Gate Array
2D	Two-Dimensional
FPS	Frames Per Second
FF	Feedforward
PI	Proportional-Integral
PD	Proportional-Derivative
PID	Proportional-Integral-Derivative
SMR	Shaped Model Reference
SCVCC	Sensing Coil Voltage Control Circuitry
RMS	Root Mean Squared
EMF	Electromotive Force
FOPI	Fractional Order Proportional-Integral
IFT	Iterative Feedback Tuning
FIR	Finite Impulse Response
MIIFC	Model-Free Inversion-Based Iterative Feedforward Control
IS-MRC	Input Shape Model Reference Control
IS	Input Shaper

ZV	Zero Vibration
R2R-BO	Run-to-Run Bayesian Optimization
ISMC	Integral Sliding Mode Control
IIC	Inversion-Based Iterative Control
PI	Prandtl-Ishlinskii
DIM	Direct Inverse Model
JA	Jiles-Atherton
EMC	Equivalent Magnetic Circuit
MMF	Magnetomotive Force
AWG	American Wire Gauge
IC	Integrated Circuits
MIMO	Multi-Input Multi-Output
RBF	Radial Basis Function
AI	Artificial Intelligence

l	Path length of magnetic flux.	$[m]$
μ	The permeability of the material.	$[N/A^2]$
μ_r	The relative permeability of the material.	$[N/A^2]$
μ_0	The permeability of free space which is constant at $\mu_0 = 4\pi \times 10^{-7}$.	$[N/A^2]$
σ	The electrical conductivity of the material.	$[S/m]$
B	The magnetic flux density.	$[T]$
H	The magnetic field strength.	$[A/m]$
B_s	The magnetic flux density saturation limit.	$[T]$
H_c	The magnetic coercivity.	$[A/m]$
P_L	The power dissipation for the Lorentz actuator.	$[W]$
P_R	The power dissipation for the reluctance actuator.	$[W]$
ρ_L	The average mass density for the Lorentz actuator.	$[kg/m^3]$
ρ_R	The average mass density for the reluctance actuator.	$[kg/m^3]$
ρ	The specific resistance.	$[\Omega]$
F	The output force.	$[N]$
m	The mass.	$[kg]$
g or a	The air gap displacement.	$[m]$
H_c	The average magnetic field intensity through the core.	$[A/m]$
H_g	The average magnetic field intensity through the air gap.	$[A/m]$
B_c	The average magnetic flux density through the core.	$[T]$
B_g	The average magnetic flux density through the air gap.	$[T]$

A	The cross-sectional area.	$[m^2]$
ϕ	The magnetic flux.	$[Wb]$
l_m or l_c	The mean path length of the core.	$[m]$
N	The number of coil turns.	$[-]$
i	The electrical current.	$[A]$
F_e	The elastic force.	$[N]$
F_f	The frictional force.	$[N]$
F_{mag}	The magnetic force.	$[N]$
a	The acceleration.	$[m/s^2]$
\mathcal{F}	The flux fringing factor.	$[-]$
A_{gi}	The effective cross-sectional area.	$[m^2]$
A_{g0i}	The initial cross-sectional area.	$[m^2]$
l_{gi}	The air gap displacement for the i^{th} gap.	$[m]$
l_w	The electrical coil winding length or the tooth width from the stator.	$[m]$
$\dot{\phi}$	The rate of change of magnetic flux.	$[Wb/s]$
i_e	The electrical eddy current.	$[A]$
k_e	The electrical conductance constant.	$[\Omega^{-1}]$
I	The excitation current.	$[A]$
I_0	The bias current.	$[A]$
\tilde{I}	The current difference.	$[A]$
C	Geometrical constant.	$[-]$
g_0	The initial air gap displacement.	$[m]$
σ	The electrical skin depth.	$[m]$
f	The excitation frequency.	$[Hz]$
E	The electric field.	$[V/m]$
\bar{B}	The mean magnetic flux density.	$[T]$
S	Contour area.	$[m^2]$
v_s	Sense coil output voltage.	$[V]$
H_{hyst}	The magnetic hysteresis influence on the magnetic field strength.	$[A/m]$
\mathcal{R}_C or R_C	The magnetic reluctance of the C-core.	$[H^{-1}]$
\mathcal{R}_g	The magnetic reluctance of the air gap.	$[H^{-1}]$
Φ_C	The magnetic flux of the C-core.	$[Wb]$
B_C	The magnetic flux density of the C-core.	$[T]$
A_C	The cross-sectional area of the C-core.	$[m^2]$
W_C	The stored energy in the field in terms of Φ_c and i of the C-core.	$[W]$
F_C	The output force of the C-core.	$[N]$
B_{Ca}	The magnetic flux density of the approximated C-core.	$[T]$
F_{Ca}	The output force of the approximated C-core.	$[N]$

\mathcal{R}_{ul}	The magnetic reluctance of the upper lump in the E-core.	$[H^{-1}]$
\mathcal{R}_{cl}	The magnetic reluctance of the center lump in the E-core.	$[H^{-1}]$
\mathcal{R}_{bl}	The magnetic reluctance of the bottom lump in the E-core.	$[H^{-1}]$
l_{c1}	The center tooth mean path length of the E-core.	$[m]$
l_{c2}	The upper and lower tooth mean path length of the E-core.	$[m]$
Φ_E	The magnetic flux of the E-core.	$[Wb]$
W_E	The stored energy in the field in terms of Φ_c and i of the E-core.	$[W]$
F_E	The output force of the E-core.	$[N]$
B_{Ea}	The magnetic flux density of the approximated E-core.	$[T]$
F_{Ea}	The output force of the approximated E-core.	$[N]$
L or h	The mover length or height.	$[m]$
F_{FEA}	The generated output force of the FEA model.	$[N]$
ε_C	The error between the analytical and FEA C-core model.	$[\%]$
ε_{Ca}	The error between the approximated analytical and FEA C-core model.	$[\%]$
ε_E	The error between the analytical and FEA E-core model.	$[\%]$
ε_{Ea}	The error between the approximated analytical and FEA E-core model.	$[\%]$
w	The width of the core.	$[m]$
t	The thickness of the core.	$[m]$
b	The breadth of the core.	$[m]$
c	Additional air gap displacement from asymmetries in the air gap.	$[m]$
θ	Angular offset in either $x-$, $y-$, or $z-$ axis.	$[rad]$
P_1	Magnetic permeance of the upper air gap.	$[H]$
R_1	Magnetic reluctance of the upper air gap.	$[H^{-1}]$
R_2	Magnetic reluctance of the lower air gap.	$[H^{-1}]$
k	Lower air gap displacement after offset.	$[m]$
R_I	Magnetic reluctance of the I-Beam.	$[H^{-1}]$
R_T	The total magnetic reluctance.	$[H^{-1}]$
F_1	The output force of the upper air gap.	$[N]$
F_2	The output force of the lower air gap.	$[N]$
A_G	The augmented cross-sectional area of the C-core for Case 3.	$[m^2]$

A_s	A removed section of the cross-sectional area of the C-core for Case 3.	$[m^2]$
A_T	A removed section of the cross-sectional area of the C-core for Case 3.	$[m^2]$
χ	Geometric displacement parameters of the C-core for Case 3.	$[m]$
ϵ	Geometric displacement parameters of the C-core for Case 3.	$[m]$
λ	Geometric displacement parameters of the C-core for Case 3.	$[m]$
A_1^*	The augmented cross-sectional area of the C-core after polynomial correction for the upper area.	$[m^2]$
A_1^*	The augmented cross-sectional area of the C-core after polynomial correction for the lower area.	$[m^2]$
A^*	The augmented cross-sectional area of the C-core after polynomial correction for Case 2.	$[m^2]$
A_G^*	The augmented cross-sectional area of the C-core after polynomial correction for Case 3.	$[m^2]$
A_f^*	The augmented cross-sectional area of the C-core after polynomial correction for Case 0F.	$[m^2]$
\bar{a}	Effective air gap displacement.	$[m]$
a_R	Air gap displacement effect on the reluctance equation.	$[m]$
\bar{k}	Lower effective air gap displacement after offset.	$[m]$
k_R	Lower air gap displacement effect on the reluctance equation.	$[m]$

List of Tables

2.1	Comparison of coercivity, H_c , and saturation flux density, B_s , for various materials.	18
2.2	Highlighting the pros and cons of measurement sensing systems . . .	37
2.3	Comparison of control performance (mean error, maximum error, and standard deviation) of various flux controllers of a RA system.	49
3.1	The parameters of the C-core and E-core RA.	66
4.1	Setup trials to simulate and compare with the analytic solution for verification.	97

List of Figures

1.1	The path with the higher reluctance (a) will allow less magnetic flux to flow	2
2.1	(a) 1 DOF single stroke positioning system and a (b) 1 DOF dual stroke positioning system with short-stroke and long-stroke positioning.	8
2.2	The mover in (a) has teeth which helps reduce flux fringing effects. The mover in (b) is a version of the I-beam that is elongated so the area the flux traverses is rectangular and not square. Movers with curved surfaces (c) were introduced by Nikon and invented by Kazuya Ono to help limit parasitic torques under asymmetrical air gaps, from US Patent 6,906,334	10
2.3	(a) C-Core RA and (b) E-Core RA schematic.	10
2.4	The tape-wound cut core topology allows for the grain orientations to align with the magnetic flux path which increases the core permeability, increasing efficiency.	11
2.5	Schematic of a 2DOF E-Core RA design invented by Hol from ASML. The coil is separated into two sections, allowing a torque to be generated, from US Patent 8,472,010.	12

2.6	Plunger style RA which features the mover between the stator teeth which is constrained to only move vertically towards the middle stator tooth.	13
2.7	Maxwell style RA which features the mover between the teeth of the stator along with a fixed permanent magnet as the center tooth. . . .	13
2.8	A Maxwell RA XY positioning stage is showcased which offers translational degrees of freedom in x and y direction and is powered through four Maxwell RAs.	14
2.9	Hybrid style RA examples (a), (b).	15
2.10	RA setup with connected voice coil actuators to provide relative motion between mover and stator cores as shown in (a), and (b).	16
2.11	Gravity compensated RA.	17
2.12	Variables such as the electrical current, i , and the air gap displacement, g , are used in the modeling of the actuator along with geometric parameters	21
2.13	Flux fringing at various gap lengths [1].	22
2.14	Eddy current generation in lamination layers.	23
2.15	A current-biased E-Core RA through a dual core setup.	24
2.16	A flux-biased hybrid RA with the addition of a permanent magnet to bias the magnetic flux in the Maxwell configuration [2]. Presented by Lu.	25
2.17	A flux-biased hybrid RA with the addition of a magnetic coil to bias the magnetic flux.	25
2.18	The magnetic flux representation of a C-Core RA which shows the direction, as well as the concentration of the flux in a cross-section view of the RA. COMSOL was used to generate the figure.	28

2.19	An E-Core RA with an AC flux sense coil measuring the mean flux density in the center tooth.	31
2.20	An E-Core RA with three piezoelectric load cells connected to the stator which will allow measurements of the force and two moments. .	33
2.21	An E-Core RA with an accelerometer mounted to the mover which will allow measurements of the acceleration.	33
2.22	A block diagram for RA controller with current sensing feedback and feedforward loop.	39
2.23	A block diagram for RA controller with a current sensing feedback and feedforward loop with a gap sensing feedforward path.	40
2.24	A block diagram for RA controller with a flux feedback and feedforward loop.	40
2.25	A block diagram for RA controller with a flux feedback and feedforward loop with gap sensing.	41
2.26	A block diagram for a RA controller with a flux feedback and feedforward loop, and a current feedback and feedforward loop.	41
2.27	A block diagram for a RA controller with a force feedback and feedforward loop.	42
2.28	A block diagram for a RA controller with a force feedback and feedforward loop and a current feedback and feedforward loop.	43
2.29	SVCC controller schematic.	44
2.30	Cascaded flux based RA linearization schematic.	44
2.31	The injected trapezoidal force profiles with the SCVCC feedforward controller and Hall feedback, and the corresponding error after several iterations at a fixed air gap of 0.7 mm.	45

2.32	Comparison of RA force errors in current and voltage based feedforward control. Error 1 shows no hysteresis compensation, Error 2 shows with hysteresis compensation based on the parametric hysteresis inverse, and Error 3 shows with hysteresis compensation and additional air gap disturbance $\Delta g = 1 \times 10^{-5} \sin(40\pi \times t)$	45
2.33	Schematic of the PI plus inverse Duhem hysteresis feedforward controller.	46
2.34	Experimental results with a 0.05 Hz triangular wave tracking of a RA with (a) feedback control alone, (b) using unoptimized feedforward control, (c) using the optimized feedforward control. The tracking errors (d) show E1 which represents no hysteresis compensation, E2 represents the unoptimized hysteresis compensation, and E3 is the optimized hysteresis model which has less error than the other models by a magnitude of 5.33 and 1.62 respectively.	47
2.35	IS-MRC control schematic.	48
2.36	Using a ZV shaper eliminates residual vibrations by shaping the input as shown in the step response.	48
2.37	A block diagram of a controller with feedback linearization.	50
2.38	RA flux density controller with feedback linearization.	50
2.39	Block diagram for a feedback linearization controller on a dual-stage hybrid RA.	51
2.40	A closed-loop ILC block diagram.	52
2.41	Hysteresis loop model of cobalt-iron magnetic flux density B vs. magnetic field strength H	53
3.1	(a) Schematic diagram of C-core reluctance with (b) Equivalent magnetic circuit.	63

3.2	(a) Schematic diagram of E-core reluctance with (b) Equivalent magnetic circuit considering two parallel paths.	64
3.3	The BH-curve with the relative permeability for ferromagnetic materials (a) Iron-Cobalt-Vanadium (Hiperco-50); (b) Electrical Steel (M-19); and (c) the relative permeability as a function of the magnetic flux.	67
3.4	The magnetic flux B_C of the C-core RA with input current i of 1.5 A at air gap g of 0.55 mm for ferromagnetic materials (a) Hiperco-50; and (b) M-19.	68
3.5	The comparison of C-core RA between the magnetic force of FEA, model (3.5), and model (3.6) for (a) Hiperco-50; and (b) M-19.	68
3.6	The relative force error of C-core RA in (3.16) for (a) Hiperco-50; and (b) M-19.	69
3.7	The magnetic flux B_E of the E-core RA with input current i of 1.5 A at air gap g of 0.55 mm for ferromagnetic materials (a) Hiperco-50; and (b) M-19.	70
3.8	The comparison of E-core RA between the magnetic force of FEA, model (3.14), and model (3.15) for (a) Hiperco-50; and (b) M-19.	70
3.9	The relative force error of E-core RA in (3.18) for (a) Hiperco-50; and (b) M-19.	71
3.10	Schematic diagram of the experimental setup to measure the magnetic force of the (a) C-core and (b) E-core RA. The measured signals are collected using dSPACE Board DS1104.	73
3.11	The comparison of C-core RA between the experimental measured magnetic force, the magnetic force model (3.5), and model (3.6) for (a) Hiperco-50; and (b) M-19.	73

3.12	The relative force error of C-core RA for (a) Hiperco-50; and (b) M-19.	74
3.13	The comparison of E-core RA between the experimental measured magnetic force, the magnetic force model (3.5), and model (3.6) for (a) Hiperco-50; and (b) M-19.	74
3.14	The relative force error of E-core RA for (a) Hiperco-50; and (b) M-19.	75
4.1	Case 0 is the ideal case with symmetrical air gaps. Whereas Case 1, 2, and 3, have angular disturbances in the z , y , and x axis respectively. .	79
4.2	Case 1, (a) Schematic representation of the C-Core RA and (b) COMSOL flux density distribution FEA of C-Core.	80
4.3	Geometric representation of tilted air gap for the Case 1 reluctance derivation, with a rotation in the z -axis of the I-beam.	82
4.4	The RA is modelled as a magnetic circuit (a), with the air gaps being represented (b) as a set of infinite reluctances in parallel.	83
4.5	Geometric representation of tilted air gap for the Case 2 reluctance derivation, with a rotation in the y -axis of the I-beam.	84
4.6	Geometric representation (a) of tilted cross-section for the Case 3 reluctance derivation, with a rotation in the x -axis of the I-beam. The air gap cross-section (b) is shown to not be square due to the tilted I-beam.	86
4.7	BH Curve for the Hiperco 50 0.014" annealed at 1411°F in which the I-beam and C-core are comprised of. This curve is used in the simulation and analytical models.	88
4.8	COMSOL model of the Case 0 RA, for an air gap separation of 0.5mm.	88

4.9	The analytical and COMSOL models for Case 0, are shown to match with a maximum error of 1.26% between forces in the top air gap, with a direct current of 1A and 0.25 – 2mm of gap separation.	89
4.10	COMSOL model for Case 1 RA, for an air gap separation of 0.5mm and an angle of 1.2° in the z -axis.	90
4.11	Comparing the COMSOL results with the analytically derived equation for the top force and fitting the ratio to a 3D surface with the use of Matlab’s Curve Fitting Toolbox, the correction factor equation for the new area can then be derived. The same is produced for the bottom force equation.	91
4.12	The COMSOL and analytical model of the top gap force of Case 1 are compared for various current ranging from 0.5 - 2A and z -angle disturbances. This confirms that the equations work for various current input with the biggest error being 2.3%.	91
4.13	COMSOL model for Case 2, with a gap separation of 0.25mm and an angle of 1.2° in the y -axis.	92
4.14	COMSOL model for Case 3, with a gap separation of 0.25mm and an angle of 1.2° in the x -axis.	93
4.15	COMSOL model of the Case 0F RA, which features 5mm fillets, for an air gap separation of 0.5mm.	93
4.16	Total analytical I-beam output force comparison of all considered cases at a current of $I = 1A$ and a 0.5 – 2mm of gap separation.	94
4.17	(a) Case 1 can be converted to the combination of Case 1+2 with the introduction of the effective air gap, \bar{a} , along with the derived polynomial correction factors and influence on the reluctance.	95

4.18	COMSOL model for Setup #3 which features $\theta_x = 25\text{mrad}$, $\theta_y = 20\text{mrad}$, and $\theta_z = 5\text{mrad}$	98
4.19	The (a) C-box and (b) I-box house the C-core and I-beam respectively. The F-bracket (c) houses the force sensors and is what the I-box pushes against. Solidworks cross-sectional model (c) of the experimental assembly is also shown. All housing components are 3D printed.	98
4.20	The experimental setup is shown with the 3D printed components F-Bracket, C-Box, and I-Box along with the 4 force sensors connected to the breadboard that is then connected to the dSPACE board (DS1104).	100
4.21	The (a) front, (b) back of C-Core element with the coils are shown and an inside view (c) of the C-Core inside the C-Box.	100
4.22	The modular I-box design (a) allows for certain I-beam cases to be inserted into the back (b), making experimenting easier for each case. The I-beam can then be inserted (c) and held in place with pins.	100
4.23	The C-Core setup (a) without fillets, and (b) with fillets.	101
4.24	The experimental results are shown for Case 0 and compared to the analytical solution. The error is shown to be relatively low between the analytical and experimental model with a maximum error of 11.1%.	101
4.25	The experimental results are shown for Case 1 and compared to the analytical solution. The error is shown to be relatively low between the analytical and experimental model with a maximum error of 11.6%.	102
4.26	The experimental results are shown for Case 2 and compared to the analytical solution. The error is shown to be relatively low between the analytical and experimental model with a maximum error of 10.3%.	102

4.27	The experimental results are shown for Case 3 and compared to the analytical solution. The error is shown to be relatively low between the analytical and experimental model with a maximum error of 10.7%.	103
4.28	The experimental results are shown for Case 0F and compared to the analytical solution. The error is shown to be relatively low between the analytical and experimental model with a maximum error of 9.7%.	103
4.29	The analytical and experimental results for the multi-axis Case 1+2+3, are shown for (a) $a = 1\text{mm}$, (b) $a = 1.5\text{mm}$ to match with a maximum error of (a) 10.5%, (b) 11.4% for a range of 1-2A of current.	104
A.1	The four standard types of RA are the (a) C-core, (b) E-core, (c) Maxwell, and (d) the plunger type. Components can be added also such as springs in (e), (f), (g), and (h). Mechanical amplification systems such as levers or flexures can be added such as (i), (j), (k), and (l). Two RAs can be used for a dual-core setup as seen in (m), (n), (o), and (p) to allow bidirectional motion of the mover between the cores. Permanent magnets can be added for a hybrid setup which incorporates additional flux as shown in (q), (r), (s), and (t).	129

Chapter 1

Introduction & Background

An actuator is a device or a component of a system that provides motion. The reluctance actuator (RA) gets its name from the principle of reluctance, which is the opposition to magnetic flux (the magnetic domain's resistance equivalent). Higher reluctance means it is harder for the magnetic flux to flow as shown in Fig. 1.1. The RA is usually comprised of two main components: the stator or yoke, and the mover or armature. The stator includes an electrical coil wrapped around a ferromagnetic core that when energized generates a magnetic flux due to Ampere's law. The resulting flux will propagate and create a closed loop path between the stator and the mover element. The air gap between the stator and mover resists the flow of flux due to the high reluctance in this region. Reluctance is found from dividing the path l , by the permeability μ times the cross-sectional area A . Therefore, the reluctance $R = \frac{l}{\mu A}$. Air has a relatively low permeability, which gives air a relative permeability of $\mu_r = \mu_{air}/\mu_0 = 1$ which is the ratio of the material's permeability to the permeability of free space. This leads to a relatively high reluctance since $R \propto 1/\mu$. Naturally, the system acts in a way based off Maxwell's equations to reduce the reluctance in the

system by generating a reluctance force between the stator and mover. The force is dependent on the magnetic flux and the reluctance in the air gap nonlinearly.

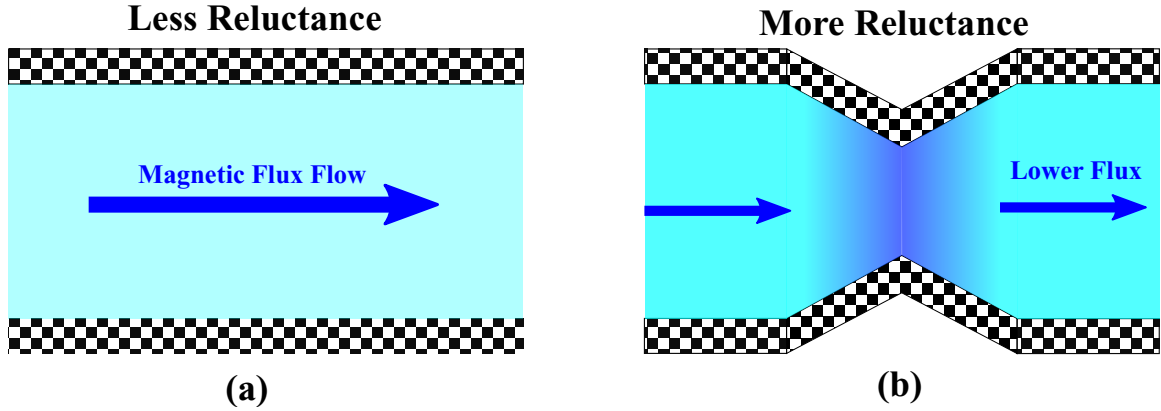


Figure 1.1: The path with the higher reluctance (a) will allow less magnetic flux to flow when compared to a path with lower reluctance (b).

The importance of the RA is that it can provide a relatively high force density and lower energy dissipation when compared to more common actuators, such as the Lorentz actuator. One obstacle, however, is the nonlinear current-force relationship, which can be difficult to predict and control. The RA has many applications where high acceleration is needed for motion systems. Some applications that could benefit include: semiconductor manufacturing, robotics, CNC fabrication, biomedical, microscopy, chemistry, spectrometry imaging, nano-structure scanning, micro and nano-manufacturing, spectroscopy, and non-linear and ultrafast optics. Having higher forces allow for higher acceleration, leading to an increased throughput when it comes to manufacturing.

RAs are shown to provide a force density 10 times higher than the traditional voice coil actuators [3]. This allows the RA to have a more compact design and not require large cooling systems since the power dissipation is low. RAs also provide superior vibration isolation since the mover component is not mechanically attached to

the actuator core. Some challenges in control of the RA which include the nonlinear current-force relationship and the gap dependency since changing the gap displacement would also change the reluctance of the gap which changes the force nonlinearly as can be seen in the analytical equations for the force. Many researchers have documented ways to model, predict, and counteract this nonlinear behaviour however. Some linearization techniques include current-biased, flux-biased, and operating point optimization. Another disadvantage is that the standard actuator configuration only generates attracting force, whereas bidirectional forces is preferable in motion control applications [4].

There are also many configurations of RA such as the C-Core, E-Core, Hybrid, and Plunger type designs. Components can also be added to help the required dynamics of the RA depending on the application. Additional components include springs, flexure hinges, mechanical levers, and permanent magnets. Springs and flexure hinges can add additional stiffness to the RA while a mechanical lever can amplify the output displacement of the actuator. Permanent magnets can be used to provide additional magnetic flux to the RA.

It is important to evaluate and simulate the physics of the RA in order to develop accurate dynamic models that can be used to develop controller and observer systems. The underlying physics of the RA is more complex than that of linear electromagnetic actuators. Using scientific principles the force output of the RA can be expressed in terms of the cross-sectional area, the electrical current through the coils, the number of coil turns, the material's relative permeability, and the air gap displacement. This will only give an approximation of the force however as the standard equation does not take into account other dynamics such as flux fringing, eddy currents, and hysteresis. Flux fringing along with eddy currents and hysteresis considerations are explained further in Section 2.3.1 and Section 2.5.5 respectively. There are models

that take into account these other dynamics and can be combined together to get a better physical representation of the RA. Finite element analysis (FEA) can also be utilized to accurately model the underlying physics of the RA. However, the main disadvantage of FEA is the processing time required to obtain accurate results and therefore cannot be used in control systems that require fast dynamic models.

In order to control the RA measurement devices are required to capture physical values to determine the position and force of the RA mover. With knowledge of certain variables other unknown variables can be determined with the use of equations and observer designs. The four main measurement systems used are flux, force, acceleration, and position. The magnetic flux can be measured with DC (direct current) or AC (alternating current) sensor devices. These devices can measure the flux inside RA with the use of Hall-effect and magneto-resistive properties. Force sensors such as strain gauges or load cells can be used to convert force into voltage readings. Another measurement that can be used is acceleration. Accelerometers can be attached to the RA mover and measure the acceleration which can be used to determine the overall force on the RA. Lastly, position sensors can be used to determine the air gap displacement with the use of inductive, optical, or ultrasonic sensors.

Controlling the RA requires a proper controller that can control the nonlinear nature of the RA. This can be a challenge but there has been plenty of control algorithms to help. Most RA setups require hybrid control systems that combine various control systems. Feedback control is most commonly used alongside feedforward control algorithms. Other considerations are including a hysteresis model and if it is an inverse model and whether an observer is used in the control design. Feedback linearization is commonly used to linearize the RA for use with conventional controller designs. This involves inverting the dynamic model of the RA. Another method is

iterative learning control (ILC). This method involves using past trial data to improve tracking performance for future trials. It uses this data to update future feedforward signals for better accuracy and decrease tracking error.

1.1 Main Objectives & Motivations

The main objectives of this thesis can be broken down as followed:

- Overall review: The first objective of the thesis would be to provide a comprehensive review of RAs, including their history, working principles, and types of RAs currently available. This review would serve as a foundation for the subsequent investigations and analyses.
- Investigation of the mean path length (MPL) term: The second objective of the thesis would be to investigate the significance of including the mean path length (MPL) term in the calculation of RA force. This investigation would demonstrate how the inclusion of the MPL term can improve the accuracy of RA force calculations.
- Demonstration of a technique for calculating force for asymmetrical instances: The third objective of the thesis would be to demonstrate a technique for calculating the force generated by various asymmetrical instances for the RA. This technique allow for a more accurate calculation of the RA force in practical applications.

These objectives would contribute significantly to the field of RA and enable the development of more efficient and effective RA systems for practical applications.

1.2 Thesis Outcomes & Contributions

Through the process of creating this thesis many papers have been published such as *Modeling and analysis of reluctance motion system with asymmetrical air gaps* [5], and *Investigating the effect of the Mean Path Length on Reluctance Actuator Output Force Characterization* [6] which were both published as journal articles in the Review of Scientific Instruments. A version of [5] was also accepted to the 31st Annual Newfoundland Electrical and Computer Engineering Conference (NECEC) and a presentation was given. The 3D printed experimentation apparatus for measuring the force for RAs was also a great outcome as it allows for static forces to be measured with the help of 3D printed parts along with testing various angular offset conditions.

1.3 Thesis Outline

The remainder of the thesis is structured as follows: A review of RA systems is performed and currently available knowledge of the RA such as available applications, configurations, dynamic models, measurement systems, and control systems for the RA are showcased in Chapter 2. Next, the importance of including the mean path length (MPL) in precision motion RA applications is showcased in Chapter 3. In Chapter 4 the asymmetrical cases for the RA are modelled and further analyzed with multi-axial cases to determine an accurate mathematical model which is tested experimentally. Finally in Chapter 5, conclusions and future work are presented.

Chapter 2

Review of Modeling and Control of Linear Reluctance Actuators in Precision Motion Systems

2.1 Available Applications

There are many potential applications for the RA. With efficient and accurate models, the RA can be controlled and work more efficiently than the traditional Lorentz actuators especially in short-stroke high-precision positioning applications [7]. These applications include: micro and nano-fabrication such as laser direct writing, nanoscale scratching, sub-micron lithography, and diamond turning machines [8]. The RA can also be used for rotation such as scanning tip-tilt mirrors [9–12]. Also, there are potential applications in advanced spacecrafts, data storage, scanning microscopy, vision and optical inspection, medical, and much more [8].

The main application that is most found in the literature is for use in the short-stroke stage in photolithography machines for the semiconductor manufacturing industry [2]. The progress of semiconductor technology has been shown to increase ex-

ponentially since the middle of the previous century which is called Moore’s Law [13]. To continue this advancement trend, better actuation systems are required to allow for higher throughput of the manufacturing process. Since the RA has higher force density potential than the current Lorentz actuators used in the photolithography industry, this could allow for higher throughput in the production of semiconductors from the higher acceleration output of the RA. Photolithography machines work with a long-stroke stage and a short-stroke stage where the long stroke usually works in the meter range with tracking errors in the micrometer range, while the short-stroke working in the millimeter range reduces these errors further down to the nanometer range [7]. Since the RA works effectively in the millimeter range, it is a great candidate for the short-stroke stage system. Fig. 2.1 depicts a 1 DOF (degrees of freedom) with a single stroke and with dual stroke (short-stroke and long-stroke).

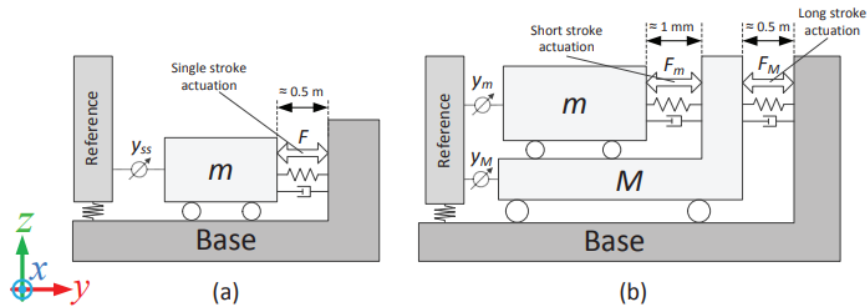


Figure 2.1: (a) 1 DOF single stroke positioning system and a (b) 1 DOF dual stroke positioning system with short-stroke and long-stroke positioning [7]

The main properties that the short-stroke stage should achieve are: high force predictability, low sensitivity to vibrations, minimized mass, and limited heat dissipations [7]. The current state-of-the-art Lorentz actuator are becoming inefficient at meeting these properties, especially maximal force and heat dissipations. The RA provides great properties over the Lorentz in these areas, however, the nonlinearities and position dependency pose problems that need to be overcome with the use of

advanced modelling and control [7]. In the past RA have been used for applications where larger errors could be tolerated such as use in active magnetic bearings [7, 14].

Long-stroke applications would not be viable for the standard RA design since it would leave the effective air-gap range due to the amount of force that is generated is reduced based off an inverse square of the air gap displacement. Therefore, the RA is better suited for short-stroke setups in the millimeter range where the force output is much higher.

2.2 Configurations of RA

The RA has many stator topologies with the standard four being the C-Core, E-Core, Hybrid, and the plunger-type. With these topologies, components such as springs, flexures, and magnets can be added to help design requirements. The stator and mover components are usually built using layers of laminations that are $\sim 100\mu\text{m}$ thick [2]. Depending on the task or the experiment under investigation the configuration of the RA can change. The mover is usually an I-beam or a rectangular prism but in some cases can have teeth similar to the stator [2] which helps eliminate flux fringing, have a rectangular magnetic flux cross-section [15], or be curved to help eliminate parasitic torques as shown in Fig. 2.2.

There are a lot of setups and combinations of components such as springs, flexures, multi-cores, and magnets for the RA. A chart of various configurations and examples can be seen in Fig. A.1 featured in Appendix A.

2.2.1 C-Core

The C-Core topology design features a stator with a block style ‘C’ shape with one or two coils as shown in Fig. 2.3(a). The mover is an I-beam which is a rectangular

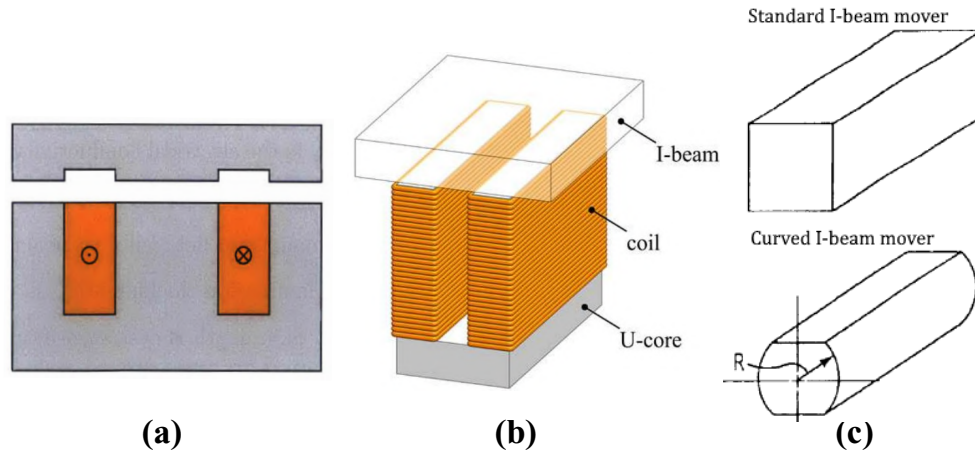


Figure 2.2: The mover in (a) [2] has teeth which helps reduce flux fringing effects. The mover in (b) [15] is a version of the I-beam that is elongated so the area the flux traverses is rectangular and not square. Movers with curved surfaces (c) were introduced by Nikon and invented by Kazuya Ono to help limit parasitic torques under asymmetrical air gaps, from US Patent 6,906,334 [16]

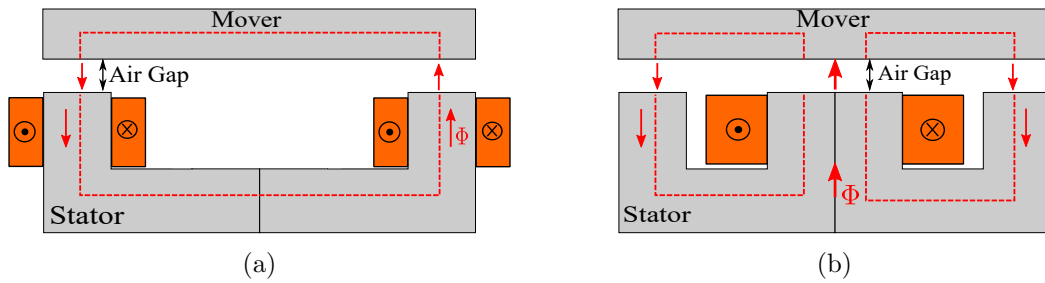


Figure 2.3: (a) C-Core RA and (b) E-Core RA schematic.

prism that allows flux to flow between the two teeth of the stator. Both stator and the mover and made out of ferromagnetic materials to allow magnetic flux to flow. The C-Core has been studied in papers such as in [2, 3, 7, 15, 17–25] all show similar derivations for the force equation. The standard C-Core with no added components, is one-directional with a nonlinear negative stiffness. Most papers focus on finding ways to linearize the C-Core due to the non-linearity with the use of various control methods. The benefits of the C-Core over other designs is the additional space in between the two teeth where a bearing or other components could be added. Also,

the C-Core provides lower mass when compared to other configurations.

2.2.2 E-Core

The E-Core design is similar to the C-Core with an added tooth in the middle giving it the style of the letter ‘E’ as shown in Fig. 2.3(b). The coil is usually featured on this middle tooth. E-Core setups are covered in the following papers [2,4,7,23,26–39]. Some setups will also add a permanent magnet as an added component on the middle tooth to help linearize the current-force relationship around zero current and to offset the actuator force. This can be seen in Fig. A.1-r. The advantages of the E-Core design is an increase in force density due to the additional tooth which induces higher flux flow as seen in Fig. 2.3(b).

Another generation of core topology is the tape-wound cut core. Most cores are created by stacking thin laminated sheets of ferromagnetic materials. The tape-wound cut core design is created by wrapping the ferromagnetic sheets around a bobbin and then cut in half which then can be placed side-by-side to create a special E-Core, so the internal laminations are oriented in the same direction as the magnetic flux in the complete path which increases the core permeability [2] as shown in Fig. 2.4.

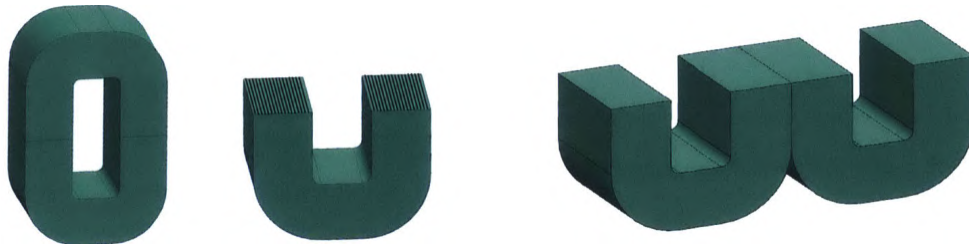


Figure 2.4: The tape-wound cut core topology allows for the grain orientations to align with the magnetic flux path which increases the core permeability, increasing efficiency [2].

The torque of the mover can also be controlled if the coils are split into two

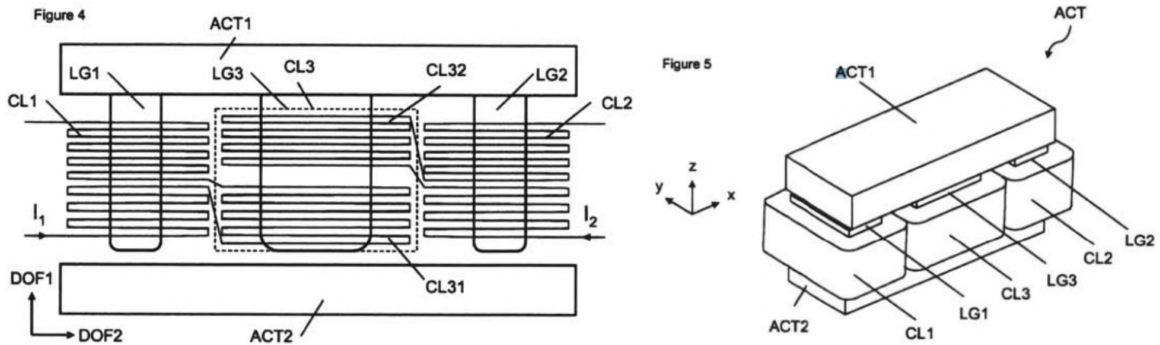


Figure 2.5: Schematic of a 2DOF E-Core RA design invented by Hol from ASML. The coil is separated into two sections, allowing a torque to be generated, from US Patent 8,472,010 [40]

independent coils which can potentially generate different forces in the left and right of the mover, which can generate a torque. As seen in Fig. 2.5, the middle coil is split and one section is connected to the first tooth coil, while the other section is connected to the last tooth in series [27].

2.2.3 Plunger

The plunger type RA features a mover that slides into the stator. This RA can be designed to have a force that is independent on the mover position. This style of actuator can be seen in Fig. 2.6. Plunger type RA can be found in papers such as [3, 30, 41–49].

2.2.4 Maxwell

The Maxwell configuration, also called the Maxwell normal stress RA [50], features a permanent magnet and is therefore also a hybrid RA and is even called a hybrid RA in some cases. However a hybrid RA can refer to any configuration that has a permanent magnet and therefore it is recommended to use the term Maxwell for this

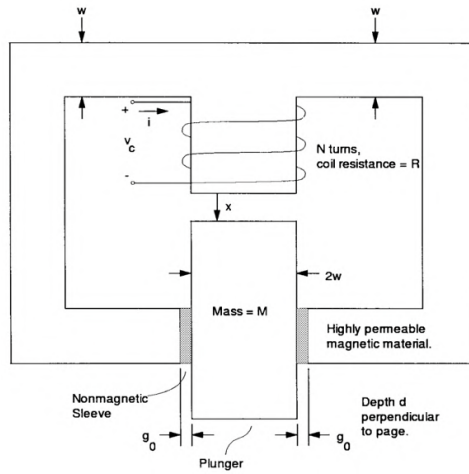


Figure 2.6: Plunger style RA which features the mover between the stator teeth which is constrained to only move vertically towards the middle stator tooth [30].

specific configuration. The Maxwell RA has been featured in papers such as [49–57]. The key feature of the Maxwell RA is that the mover is confined between the teeth of the stator with a permanent magnet as the middle tooth. A schematic showing the topology can be seen in Fig. 2.7.

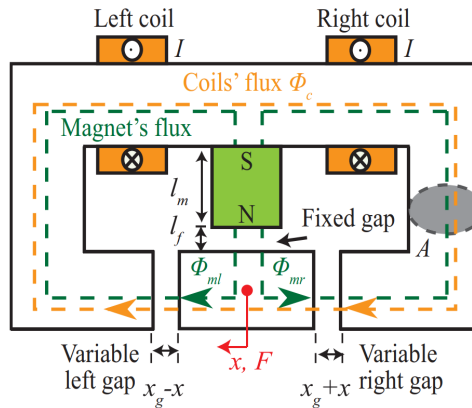


Figure 2.7: Maxwell style RA which features the mover between the teeth of the stator along with a fixed permanent magnet as the center tooth [53].

In [56, 57] a group of Maxwell RAs are used to control a 2DOF XY positioning stage with the addition of double parallelogram flexure mechanisms to offset the RA's

nonlinear negative stiffness and improve energy efficiency. The xy stage used in these papers offers the first documented RA xy stage and the layout of the system is shown in Fig. 2.8. The Maxwell RA has low inertia with a high force density and quick response since the excitation coils are concentrated around the yoke, increasing the natural frequency and reducing the mover's mass [50]. However, the travel range is limited to the space in between the stator teeth. The hybrid RA can offer up to 9.6 times the force when compared to standard voice coil actuators [54].

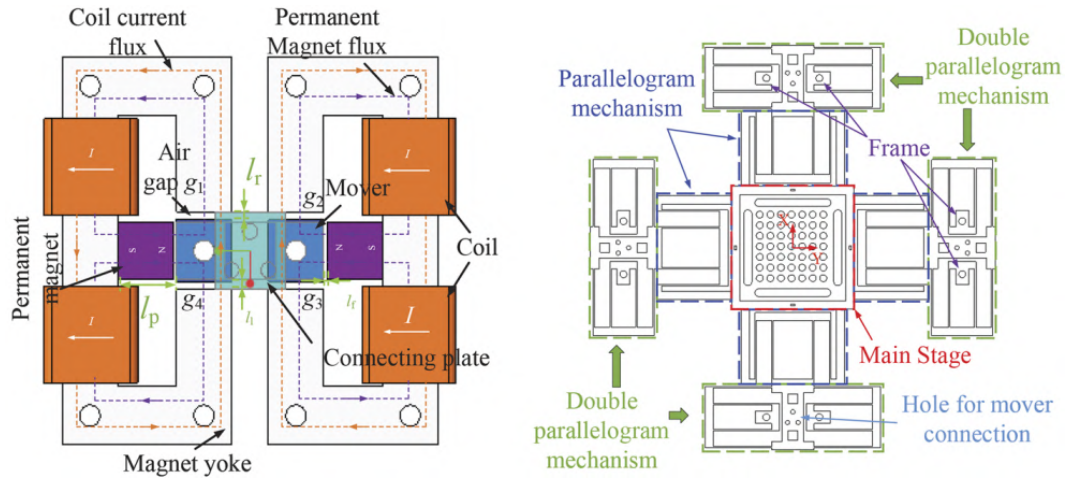


Figure 2.8: A Maxwell RA XY positioning stage is showcased which offers translational degrees of freedom in x and y direction and is powered through four Maxwell RAs [56, 57].

2.2.5 Hybrid

The hybrid type is an RA that features a permanent magnet connected to the stator and has a mover between the two teeth of the stator, offering bidirectional motion. The hybrid setup is mainly featured in the Maxwell RA configuration style as the Maxwell RA is a type of hybrid. However, not all hybrid's are Maxwell RA since the Maxwell is just a specific configuration. The additional permanent magnet helps offset

the force and the added bias will help linearize the current-force relationship [54]. The hybrid RA has been featured in papers such as [9–12, 49–55, 58]. The actuator force in hybrid RA comes from the combined magnetic flux of the coil with the flux of the permanent magnet [9]. Examples can be seen in Fig. 2.9.

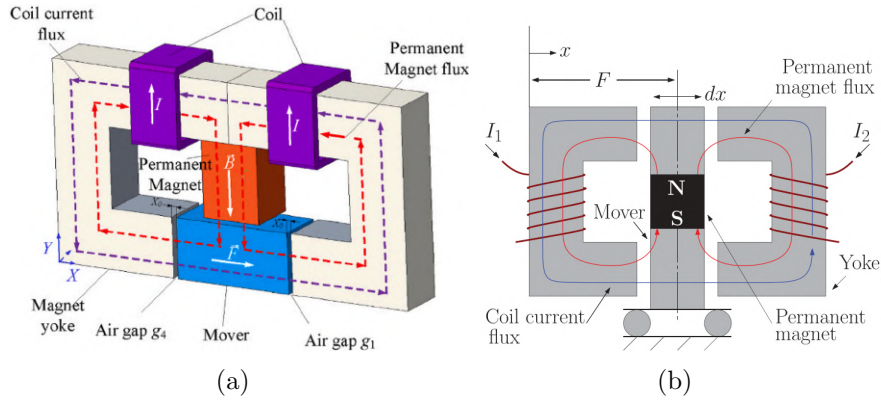


Figure 2.9: Hybrid style RA examples (a) [55], (b) [58].

2.2.6 Additional Components

Flexure mechanisms can be incorporated into the design. These mechanisms can help amplify the displacement which can improve the maximum displacement as seen in Fig. A.1-j [59, 60]. However, using flexures can inhibit vibrations into the RA, losing the advantage of vibration isolation. Flexures can be used to rotate the mover as seen in the special hybrid tip tilt actuator shown in Fig. A.1-l [9–12]. A mechanical lever system can also be used, for example in Fig. A.1-i a lever is connected to the mover to amplify the mover’s motion [20]. A flexure design also adds stiffness to the system such as being attached to the mover to counteract the nonlinear negative stiffness of the RA as seen in Fig. A.1-k [51–53]. In [56, 57] double parallelogram flexure mechanisms are used to offset the stiffness in an XY stage operated by Maxwell RAs

to provide 2DOF in x and y directions.

The system setup is also important such as the use of springs or bearing restraints onto the RA. Similar to the flexure hinges, springs can be added to the RA at various locations on the mover to increase the stiffness and offset the nonlinear displacement-force relationship of the RA as seen in Fig. A.1-e,f,g,h [18, 19, 28, 41, 42]. Voice coil actuators are often used in RA experiments to allow the mover to be accurately moved and to get into the proper air gap position and also offer bidirectional motion the RA as seen in Fig. 2.10. Gravity compensation can also be used as shown in Fig. 2.11 to alleviate the force relationship [4] by orienting the motion path of the RA against gravity, the RA can be suspended and moved vertically and released with the use of gravitational forces. In [61] a novel gravity compensated 2-DOF hybrid RA is demonstrated with an actuation range of ± 0.7 mm and is shown to allow for energy efficient gravity compensation through experimentation. It was shown that for a 500 g payload the amount of current required to support it was reduced from 1.58 A to 10 mA, which is a reduction in power consumption by a factor of 25,000.

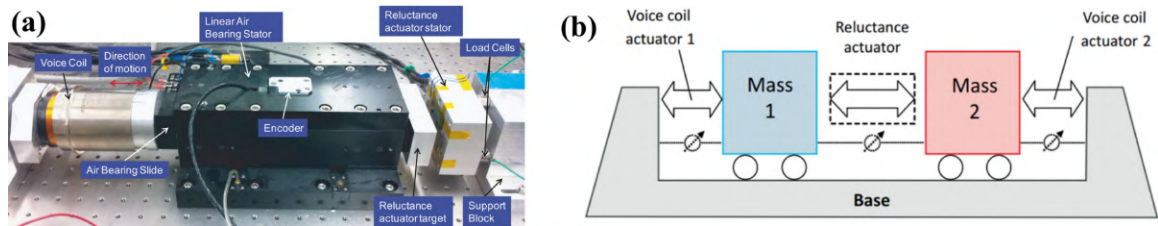


Figure 2.10: RA setup with connected voice coil actuators to provide relative motion between mover and stator cores as shown in (a) [2, 33], and (b) [7, 23–25].

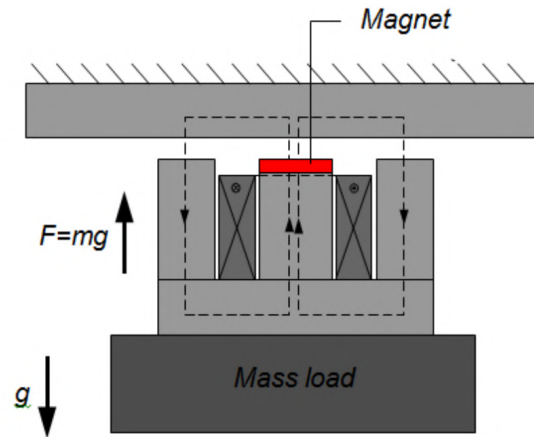


Figure 2.11: Gravity compensated RA [4].

2.2.7 Core & Mover Material

The material used for the RA is important as some ferromagnetic materials provide higher saturation limits of the flux density which allow for higher forces to be realized. The main parameters for material selection are saturation flux density, B_s , coercivity (resistance to magnetization changes or how wide the hysteresis loop is [62]) H_c , permeability μ , and electrical conductivity σ [2]. Permeability is the ratio between the flux density, B , and the magnetic field strength H and can be calculated through a material's BH curve as the permeability changes depending on the flux density [62]. Since the magnetic potential drop in the core and mover is smaller with a larger permeability, the RA will function more effectively. Coercivity and saturation flux density are often trade-offs since a material with a higher saturation flux density will often also have a higher coercivity, resulting in a wider hysteresis loop making the system behave more nonlinearly (hysteresis errors) [2]. Table 2.1 shows a comparison between some of the key parameters of various core and mover materials. The cobalt-iron (CoFe) alloys are recommended since they can provide the highest saturation flux density and therefore the highest realized force density (force-to-mass ratio) than

other alternatives due to the higher saturation flux density.

Table 2.1: Comparison of coercivity, H_c , and saturation flux density, B_s , for various materials [2].

Material	Coercivity H_c (A/m)	Saturation Flux Density B_s (T)
50% Ni-50% Fe	9.6	1.6
49% Ni-49% Fe	4.0	1.5
49% Co-49% Fe	14.4	2.3
3% Si-97% Fe	31.8	2.0
Nanocrystalline	0.6	1.2

2.2.8 Thermal Management

Electromagnetic actuators will dissipate heat mostly through the coil windings as the electrical resistance to the current produces heat [7]. This can be a problem if actuators require long operating times since they will heat up the conductive metal components of the actuator over time. You can cool the actuator through water cooling [7] or through cryogenic coolers [13]. The RA is actually more efficient in power dissipation than the Lorentz actuator for forces higher than 30 N (at a air gap ≤ 1.5 mm [7]. Therefore the RA requires less cooling than the Lorentz actuator for high force applications allowing more compact actuation systems that do not require large cooling systems. The power dissipation for the Lorentz actuator, P_L , and the RA, P_R is shown in the following equations:

$$P_L = \frac{16\rho\rho_L}{\mu_0^2 H_c^2 \pi} \times \frac{F^2}{m}, \quad P_R = \frac{64\rho\rho_R}{\mu_0 \pi} g^2 \times \frac{F}{m} \quad (2.1)$$

Where ρ_L and ρ_R are the average mass density of the Lorentz and RA respectively. ρ is the specific resistance of the conductive material of the coil. F and m are the output force and actuator mass respectively. H_c is the coercive field strength of the

Lorentz actuator. g is the air gap of the RA and μ_0 is the permeability of free space. These equations show that the RA is more efficient (low heat dissipation) for short-stroke applications where the g term. It was shown that if $g = 1.5$ mm the RA outperforms the Lorentz when $F \geq 30$ N but if the g is increased to $g = 3$ mm for example, the force required to perform more efficiently is when $F \geq 120$ N [7].

2.3 Available Dynamic Models of RA

The dynamic model for the RA is derived mainly from two basic principles which are *Ampere's circuital law*, and *Maxwell's stress tensor* [7]. *Ampere's circuital law* through one path of the C-Core RA yields:

$$Ni = \oint H \, dl = 2H_g g + H_c l_m \quad (2.2)$$

Where N is the number of coil turns, i is the electrical current, ϕ is the magnetic flux, l_m is the mean path length of the magnetic circuit, H_c is the average magnetic field intensity through the core, and H_g is the average magnetic field intensity through the air gap length g . The H_c and H_g are dependent on μ_r , the relative magnetic permeability of the core material, and the magnetic permeability of free space $\mu_0 = 4 \times 10^{-7}$. Equations 2.3 and 2.4 relate μ_r and μ_0 to B_c , the average magnetic field density through the core and B_g , the average magnetic field intensity through the gap in terms of H_c and H_g .

$$B_c = \mu_0 \mu_r H_c \quad (2.3)$$

$$B_g = \mu_0 H_g \quad (2.4)$$

RAs are used in high precision motion system with a small air gap; therefore, fringing is neglected [7]. For this standard derivation, eddy currents are neglected, as well as

the hysteresis effects because steady state DC current is applied. The area of the cross section in the air gap and the core can be considered equal. Therefore, through the relationship between flux and cross-sectional area in Eqn. 2.5, the magnetic field density is uniform throughout the magnetic circuit, and B_c and B_g can be considered as B , where A is the RA tooth cross-sectional area.

$$B = \frac{\phi}{A} = B_c = B_g = \frac{\mu_0 N i}{\frac{l_m}{\mu_r} + 2g} \quad (2.5)$$

Next, taking into consideration *Maxwell's stress tensor* through the air gap, With the assumption from Eq. 2.5 that the flux density in the air gap of the RA is homogeneous yields:

$$F = \frac{1}{2\mu_0} \oint B^2 dA = \frac{B^2 A}{2\mu_0} = \frac{\mu_0 N^2 i^2 A}{2\left(\frac{l_m}{\mu_r} + 2g\right)^2} \quad (2.6)$$

With F being the force output from one RA tooth (C-Core's total force would be double from having two teeth for example). Most papers choose to assume $\frac{l_m}{\mu_r} \lll g$ [2, 7] which simplifies Eq. 2.6 to:

$$F = \frac{\mu_0 N^2 i^2 A}{8g^2} \quad (2.7)$$

There are other methods to derive the final force equations for the RA that will lead to the same result. Some of these methods include using Faraday's law of induction and co-energy principles, and reluctance principles from a magnetic equivalent circuit (MEC) concept. Next, the mechanical dynamics can be defined based off Newton's second law [63]:

$$F_e(g) + F_f(g, v) + F_{mag}(g, \phi) = ma \quad (2.8)$$

Where m is the mover's mass, a is the mover's acceleration F_e , F_f , F_{mag} are the elastic, friction and magnetic forces that affect the mover respectively. Other research has included many nonlinearities into the dynamic model of the RA.

The main variables used in modeling of an RA is the air gap displacement and the electrical current since these are important for the control of the RA. Parameters can also be changed and optimized in the design such as the geometry, the number of coil turns, and the material type used. This is shown in Fig. 2.12 for a C-Core and E-Core setup.

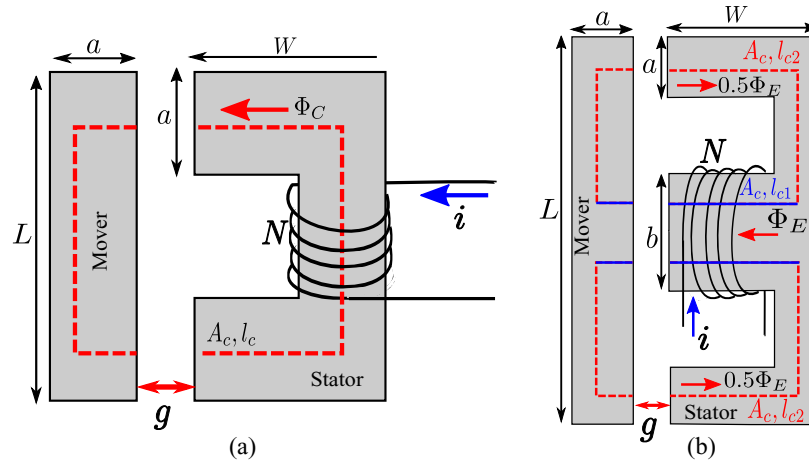


Figure 2.12: Variables such as the electrical current, i , and the air gap displacement, g , are used in the modeling of the actuator along with geometric parameters such as the length, L , width, w , and thickness, a , of the stator and mover elements, along with the number of coil turns, N , as shown for a C-Core (a) and an E-Core (b) RA setup.

2.3.1 Flux Fringing & Eddy Current Considerations

Flux field lines can bend around the air gap depending on the air gap displacement creating the fringing flux effect which is a function of gap dimension, shape of pole faces, and the shape, size, and location of the winding [1]. An example of how gap

length changing the fringing lines is shown in Fig. 2.13. Flux fringing will reduce the total reluctance of the magnetic path and can be calculated as a flux fringing factor on each gap, \mathcal{F} , [1] or by updating the effective area, A_{gi} , based on \mathcal{F} [63]:

$$A_{gi} = A_{g0i} \cdot \mathcal{F} = A_{g0i} \left(1 + \frac{l_{gi}}{\sqrt{A_{g0i}}} \ln \left(\frac{2l_w}{l_{gi}} \right) \right), \quad (2.9)$$

where A_{g0i} is the initial area, l_w is the coil winding length or the tooth width from the stator, and l_{gi} is the air gap displacement for the i^{th} air gap [63].

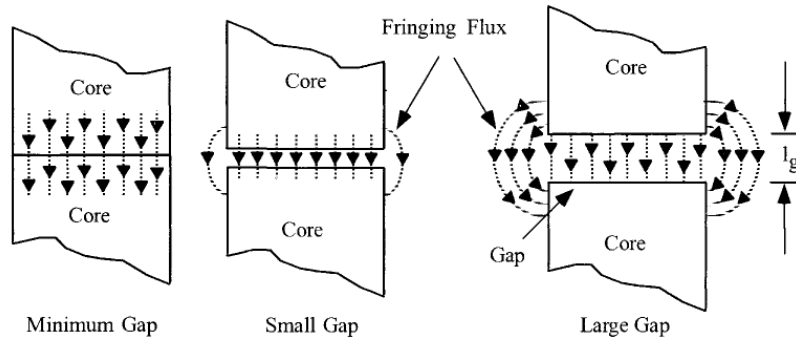


Figure 2.13: Flux fringing at various gap lengths [1].

Taking into account the flux fringing effect, allows for a better representation of the true nature of the RA, especially at larger air gaps. Flux fringing effects were modelled and were shown to match relatively well with experimental data in [63].

When changing flux lines pass through the ferromagnetic core they can induce small electrical currents, called eddy currents [1]. These eddy currents will generate a counteracting magnetic flux depending on core geometry which can degrade the RA performance [1, 2]. Eddy currents can generate in lamination layers and can be reduced through an insulated coating applied to the surface of the lamination as shown in Fig. 2.14 [1].

Since eddy currents are proportional to the rate of change in magnetic flux, $\dot{\phi}$, and

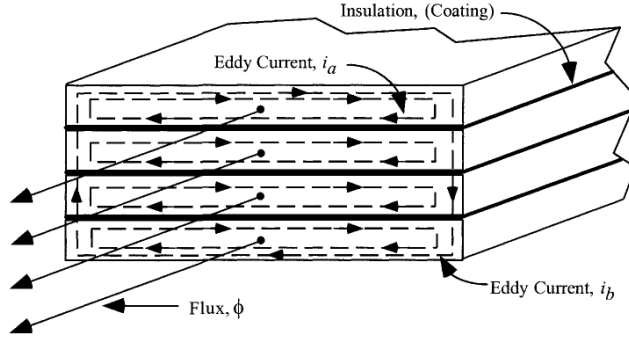


Figure 2.14: Eddy current generation in lamination layers [1].

with the assumption the magnetic flux is uniform within the cross-section, the eddy current, $i_{eddy} = -k_e \dot{\phi}$, where k_e is a constant [48,63] that is governed by the geometry and electrical conductivity of the iron core. One way to reduce eddy current losses is with the using specialized metals for the stator and mover components. In [51–53] laminated electrical steel sheets of EN10025-S235JR are used for this purpose.

2.3.2 Design Considerations

The RA is a nonlinear system in nature and therefore it is beneficial to try and make it more ‘linear’ to allow for easier control and estimation. Some ways to push towards this linearity is with the use of current-biasing, flux-biasing (with permanent magnet or magnetic coil), and operating point optimizations [2].

The linearity of the RA can be improved through the use of current-biased linearization [2]. The method works by having a two stator (dual core setup) that are placed on each side of the mover as shown in Fig. 2.15 [2].

I_1 and I_2 are the excitation currents in the first and second stators respectively, and g_1 and g_2 are the associated air gaps [2]. The actuation force on the mover can be found to be:

$$F = \frac{C}{g_0^2} I_0 \tilde{I}, \quad (2.10)$$

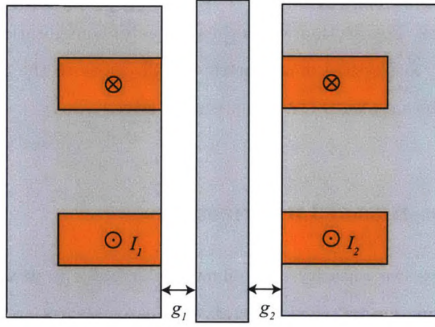


Figure 2.15: A current-biased E-Core RA through a dual core setup [2].

where C is a constant based on the number of turns and geometry, $I_0 = (I_1 + I_2)/2$ is the bias current, and $\tilde{I} = (I_1 - I_2)/2$ is the current difference [2]. A detailed analysis is found in Section 2.2 of [64]. The current-biased RA setup has some flaws however, such as requiring a high bias current which will result in high power dissipation when generating zero net force or at rest [2]. Another linearization technique is the use of a permanent magnet to bias the magnetic flux [2]. An example can be seen in Fig. 2.16. The force derived in [64] is:

$$F = \frac{A}{\mu_0} B_0 \left(\frac{\mu_0 N I}{g_0} + \frac{2g}{g_0} B_0 \right) \quad (2.11)$$

Where A is the area of the mover normal to the direction of motion, B_0 is the DC bias flux produced from the permanent magnet, NI is the total number of coil turns, g_0 is the air gap when mover is centered, and g is the air gap deviation from the center position [2]. This setup allows the output force to be both linear in the current and the air gap. This is also more efficient than the current-biased linearization model since the bias flux is generated by a permanent magnet, not an external current [2].

The disadvantage is there is a negative stiffness in the direction of the permanent magnet's magnetization (orthogonal to the motion direction [2]). This could cause potential problems from the negative stiffness in the non-scanning axis of the RA.

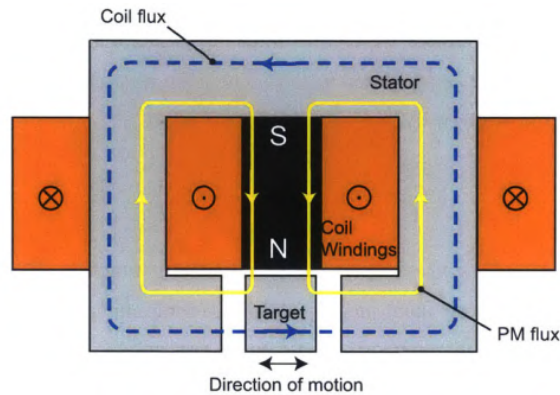


Figure 2.16: A flux-biased hybrid RA with the addition of a permanent magnet to bias the magnetic flux in the Maxwell configuration [2]. Presented by Lu [64].

Instead of having a permanent magnet, an electromagnet or magnetic coil can provide the bias flux [2]. This setup can be seen in Fig. 2.17. The advantage here is the negative stiffness pushing against the motion axis could be eliminated at selected times since the bias flux can be essentially ‘switched off’ [2].

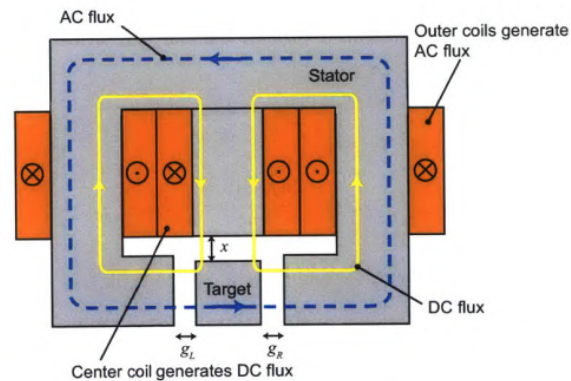


Figure 2.17: A flux-biased hybrid RA with the addition of a magnetic coil to bias the magnetic flux [2].

The disadvantages are that the RA would be less efficient since now you have external current that is required to generate the DC flux and there is an added complexity in having to manage the ‘switching off’ of the magnetic DC coil which

does not ‘switch off’ instantaneously due to the coil inductance and the slew rate [2]. Also, the RA geometry would have to be designed in a way so the magnetic coil DC flux does not couple with the AC flux. This would require a larger gap x between the magnetic DC coil and the mover, leading to even larger power losses to drive the magnetic DC coil.

Lastly, another way to help push the linearization is through the operating point selection. One example would be to operate away from the saturation region so the RA would have the same permeability throughout the operating regime with the hysteresis also being reduced and $F \propto I^2$ will remain approximately accurate [2]. The disadvantage, however, is the RA would not reach it’s full force potential since the mover mass will need to be made larger to generate the required force and especially in high-acceleration applications where low moving mass is critical [2].

Another method is to increase the nominal operating air gap. This essentially ‘shears’ the original hysteresis loop by the amount nB/μ_0 where $n = 2g/l_m$, thereby making the $B - H$ relationship more linear [2]. The linearization occurs due to the linear air gap reluctance being much larger than the nonlinear ferromagnetic material reluctance, leading the magnetic field strength of the gap H_g dominating over the ferromagnetic material magnetic field strength H_{Fe} [2]. Another advantage is that gap disturbances would have a lower effect on the force output since the stiffness is essentially reduced [2]. The disadvantage is that more current would be required to generate a force, leading to higher power dissipation [2]. Also, the larger air gap would lead to more flux fringing, and the mover would need to be enlarged, leading to lower force potential [2].

2.3.3 Finite Element Modeling Methods

Finite element analysis (FEA) or finite element method (FEM) can be used to model physical systems with high accuracy. The disadvantage however is the processing time to simulate the underlying physics. Programs such as COMSOL, ANSYS, and Abaqus can be used to simulate the magnetic fields involved in the RA. COMSOL is the most used FEA program for RA modeling and is featured in [5, 6, 15, 47, 48, 65] and is shown to be highly accurate at replicating real-life electromagnetic physics. In [47] the results from the FEM are used in conjunction with experiment findings to characterize the RA better by using system identification techniques to determine the unknown parameters between the ideal FEM scenario and the real-life experimental RA setup. In [5] a combination of FEA is used with analytical equations to formulate a more accurate mathematical model of the RA for cases when there are asymmetries in the air gap between the mover and stator. In [9] a FEM through ANSYS is presented to simulate the dynamics of a 2-DOF hybrid RA which accurately predicted the experimental results which was validated through comparing the measured frequency. It was also shown that the triangular mesh requires the maximum height of each triangular element to be smaller than the skin depth, $\delta = 1/\sqrt{\pi f \mu \sigma}$ (σ is the electrical conductivity, μ is the relative permeability) at the excitation frequency, f , in order to have more precise computation of the eddy currents in the model. Using FEA allows for flux fringing, eddy currents, and hysteresis behaviours to be modelled effectively by democratizing the system into smaller connected elements. This allows the user to also see a visual representation of the magnetic flux lines as well as the color-coded flux density which can be beneficial to system optimization as can be seen in Fig. 2.18. The main disadvantage to using FEM is the processing time it takes to obtain accurate simulations.

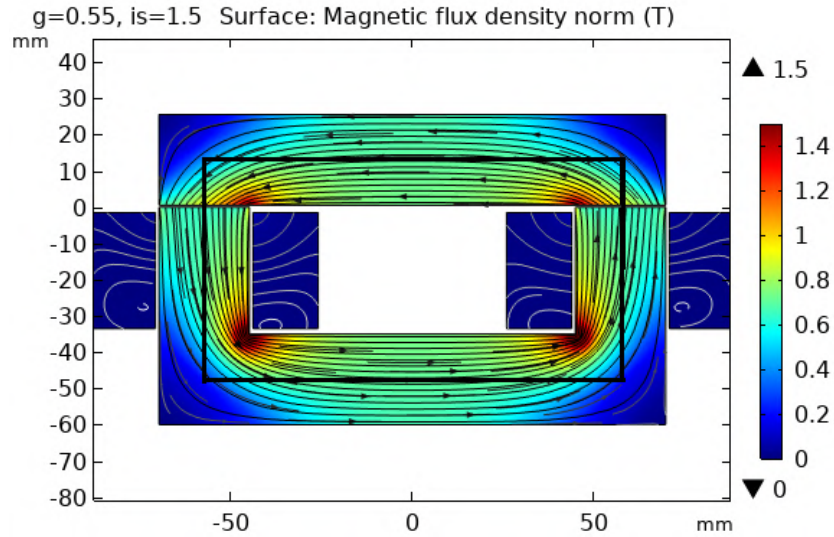


Figure 2.18: The magnetic flux representation of a C-Core RA which shows the direction, as well as the concentration of the flux in a cross-section view of the RA. COMSOL was used to generate the figure [6].

2.4 Available Measurement Systems

In order to control the RA, a reference needs to be measured. The types of measurement devices include: flux sensors, force sensors, acceleration sensors, gap sensors, and a multi-sensor setup [2]. Observers can also be used to limit the required measurement systems such as force and air gap sensors.

2.4.1 Flux Sensing

The magnetic flux density in the RA can be measured through a Hall-effect sensor or a sense coil and used to estimate the current actuator state. The advantages of flux sensing is the signal is bipolar meaning a negative actuator flux results in a negative sensor reading [2]. This allows the RA controller to smoothly operate through the zero-flux point without switching problems arising [2]. Another benefit is mover acceleration will not affect the sensor reading and the sensor attachment and

location should not have a drastic effect on the system dynamics like added stiffness or mass [2]. The disadvantage being that the flux-force relationship must be modeled accurately to achieve accurate force control [2].

There are two types of flux sensors, DC or AC. DC flux sensors include Hall-effect, magnetoresistive (MR), and giant magnetoresistive (GMR) sensors [2]. The downside to the Hall-effect sensor is it is an active sensor meaning it requires a constant current or voltage source and they usually have higher temperature sensitivity and noise characteristics when compared to a sense coil. MR and GMR sensors work on the magnetoresistance phenomenon where a material's electrical resistance changes in response to an applied magnetic field [2]. The difference between MR and GMR is that the percent change in resistance for the same magnetic field is much greater in GMR sensors [2]. The main disadvantage is that they are also active sensors like the Hall-effect sensor. They also usually have a low linear range, exhibit hysteresis, and are mostly unipolar (cannot distinguish between positive and negative magnetic fields) [2]. The advantage of the DC flux sensor is that the flux density can be directly measured at DC. The disadvantages being that the measurement is localized and does not capture the average flux density over the entire cross-sectional area, it only encompasses a small fraction of the area. In [24] shows that an air gap observer can be used to offer force control based off hall probe feedback without the need for force or position measurements. The flux density distribution is not uniform and can give inaccurate measurements for the true average flux density [2]. Multiple sensors can be used and averaged to reduce this disadvantage, however, this leads to additional computation and more A/D channels required leading to a higher reliability risk [2]. This sensor also requires the flux to pass through it, meaning it has to be positioned at the air gap interface, limiting the minimum air gap achievable since the sensor occupies some of the space. A solution is to embed the sensor into the pole face, but

this also would reduce the measured flux [2].

An AC flux sensor uses a sense coil by taking advantage of Faraday's Law [2]:

$$\oint_C E dl = -\frac{d}{dt} \iint_S B dS = -\frac{d\bar{B}}{dt} A \quad (2.12)$$

Meaning the line integral of the electric field, E , around a closed contour is equal to the negative rate of change of the mean magnetic flux density normal to the contour's surface, \bar{B} , times the surface area A [2]. The equation can be simplified further and the mean magnetic flux density, \bar{B} can be isolated as [2]:

$$\bar{B} = \frac{1}{NA} \int v_s dt, \quad (2.13)$$

The flux passes through the sense coil as shown in Fig. 2.19 [2]. The mean flux density is proportional to the integral of the voltage measured from the sense coil. This offers many advantages such as being able to capture a bigger area (since it measures the mean magnetic flux through the complete area) than the more localized DC sensors. Resulting in lower sensitivity of the force-flux relationship to gap disturbances and off-axis motion, and to local variations in saturation [2]. Also, the sensor is less noisy than a hall-effect sensor. Another advantage is it is a passive sensor meaning it does not require any current or voltage source to operate since it naturally produces its output. Other equipment would be required however to perform the integration, but the sense coil does not take up much space and does not interfere with the air gap, allowing a more efficient RA [2]. In [32] a sense coil is used as a flux sensor to measure the flux density and directed through a linear power amplifier (25A/100VDC) and transferred to dSPACE (CP1103) after a low-pass filter and acquired at a sampling frequency of 10 kHz for data acquisition of an E-Core RA.

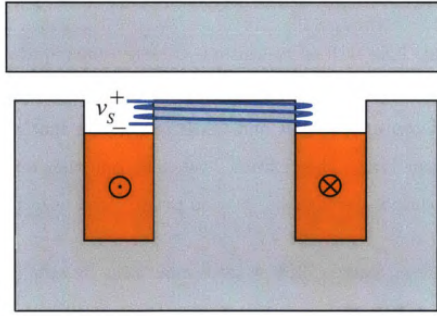


Figure 2.19: An E-Core RA with an AC flux sense coil measuring the mean flux density in the center tooth [2].

The main disadvantage to a sense coil is it does not provide a direct measurement and due to integration, it may be difficult to get an accurate DC flux estimate [2]. A hybrid configuration with sensor fusion could help these issues.

A hybrid setup includes both a DC sensor and a sense coil. This will allow the user to take advantage of both sensor readings, for example, using the DC sensor for low frequency and the sense coil for high frequency measurements [2]. In [7] an example of a hybrid setup is showcased and how it can be used along with a controller to operate a RA successfully.

The disadvantage to a hybrid sensor setup is that the extra sensors and wiring creates added complexity and extra reliability concerns [2]. Fusing the sensor outputs together may seem problematic since they will have different calibrations that would need to be verified. Also, since a DC sensor is used, the air gap range would be limited and therefore reduce the maximum force density capability of the RA [2].

2.4.2 Force Sensing

Measuring the force can also be done with the use of load cells or strain gauges a force can be measured proportional to their displacement. Some advantages include the force is able to be measured directly without the need of any intermediate variables

such as flux [2]. Another advantage is that the total force can be measured with just one sensor and the load cell will not be located in the air gap, so it will not limit the air gap range [2].

A main disadvantage, however, is the sensor cannot distinguish the direction of flux flow due to the $F \propto B^2$ relationship [2]. This can cause issues with the controller when having to operate about the zero-flux point. Another disadvantage is the sensor would add an extra stiffness element which can affect system dynamics and the inertial force from the mover introduces an error into the sensor reading [2]. Like flux sensors, force sensors also have DC or AC versions.

An example of a DC force sensor is a strain gauge. Strain gauges provide a direct DC measurement and have a lower stiffness when compared to AC-coupled piezo-based load cells. Strain gauges work by measuring the change in electrical resistance when undergoing mechanical strain [2]. The strain gauge deforms linearly with the load and the force can then be computed with Hooke's Law. A disadvantage is that strain gauges are sensitive to temperature and temperature compensation systems would dissipate additional power.

An example of an AC force sensor is a piezoelectric load cell. Piezoelectric material emits an electrical charge when stress is applied and a voltage reading can be measured and converted into an associated load [2]. Therefore, piezoelectric force sensors cannot measure static loads since the charge produced will gradually dissipate [2]. Multiple piezoelectric load cells can be used to measure the force and moments as shown in Fig. 2.20 [2].

In [31] force measurements are measured using a piezoelectric load cell (Kristler type 9272) which was utilized to measure the RA force values since it has a high rigidity and therefore, a high natural frequency. In [50] a MZLG force sensor from JinNuo Inc. is used which has a measurement range of ± 50 kg associated with a

-10 → +10 V analog transmitter output.

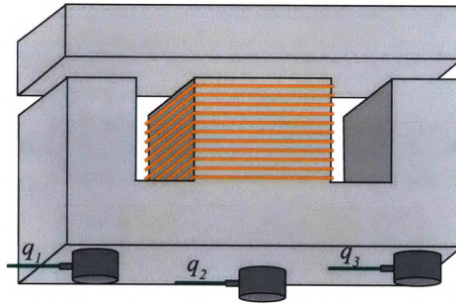


Figure 2.20: An E-Core RA with three piezoelectric load cells connected to the stator which will allow measurements of the force and two moments [2].

2.4.3 Acceleration Sensing

The force can be estimated with the use of acceleration sensors connected to the mover. Accelerometers allow for the acceleration to be measured and the force estimated since the force would be proportional to the acceleration. The accelerometer can be easily attached with to the mover with small additional mass [2]. A benefit to this sensor is it does not interfere with the air gap range since it can be mounted anywhere on the mover. An example is shown in Fig. 2.21 [2].

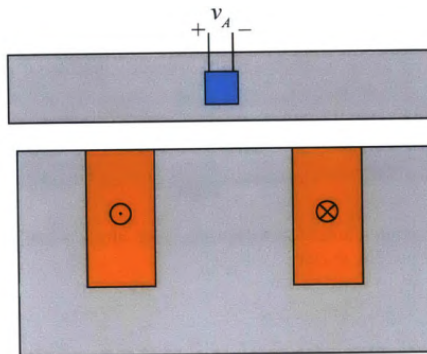


Figure 2.21: An E-Core RA with an accelerometer mounted to the mover which will allow measurements of the acceleration [2].

2.4.4 Position Sensing

The position of the RA is an important variable to also measure. Knowing the position or the air gap displacement can be useful in order to provide proper feedback to the controller being used. Also position measurements can be used to estimate other specific parameters of the dynamical model or assess positioning algorithms. It is important to have an accurate measurement of the true position of the actuator for proper control. The air gap displacement can be measured with the use of inductive sensors, optical sensors, and ultrasonic sensors. An inductive sensor or sometimes called an eddy current type displacement sensor [37] provides a non-contact displacement measurement which is based on the eddy current principle. In [9], two eddyNCDT DT3702-U1-A-C3 eddy current sensors from Micro-Epsilon GmbH with a bandwidth of 10 are used to measure the rotational position of the tip-tilt RA mover and system dynamics are identified through a 3652A system analyser from Hewlett-Packard. Optical sensors such as laser interferometers or laser displacement sensors can also provide accurate position measurements of the RA [38]. These work by reflecting lasers off the object to be measured and comparing the interference pattern between the reflected light to determine the displacement. They are used in a variety of industrial applications, including as dimensional measurements, precise object placement, irregularity detection, and vibration characterization [66]. These sensors have a precision of less than $0.1\mu\text{m}$ and sampling rates of hundreds of kilohertz, which meet the measurement demands of the RA. The disadvantage to the laser displacement sensor is it can only measure objects that are directly in-line with the laser [66]. In [50] a HL-G103-S-J laser displacement sensor from Panasonic is used to measure the displacement of the RA micro/nanopositioning stage which was able to measure ± 4 mm which was associated with an analog voltage output between

0 – 10 V. The linearity and sampling rate of this sensor was $\pm 0.1\%$ in full scale, and 200 μs respectively [50]. To read the sensor displacement and output control voltage a PCI-6221 data acquisition card from NI was used with 16-bit A/D and D/A converters. In [51–53] the RA mover carries a 43-305 retroreflector from Edmund optics for measuring position data with a 1.25 nm/bit 10899A laser interferometer from Agilent Technologies and connected via a FPGA DS5203 to a DS1005 rapid prototyping system from dSPACE for data acquisition. Another type of optical sensor is a digital camera which can record and measure pixel displacement of an object which can translate into the actual displacement. The two main types of cameras that are used as optical sensors are the line-scan camera and the high-speed camera. Line-scan cameras are essentially high-speed cameras that record just a single line of pixels which are used mainly in industrial applications to record objects that move only in one direction [66]. The advantage of the line-scan camera is the affordability compared to other solutions and their ability to record in real-time. The disadvantage however is the results rely heavily on the geometry of the moving object and lighting conditions [66]. High-speed cameras on the other hand allow for the recording of two-dimensional (2D) images at frame rates greater than 1000 frames per second (fps) with some being able to film up to a million fps [66]. There is usually a trade off between fps and resolution however, where using a higher fps setting means a lower maximum resolution that can be recorded. Higher fps allows for higher sampling rates while a higher resolution allows for better precision since there are more pixels to measure in the image. The main disadvantage of a high-speed camera is the results are not obtained in real-time since the videos take longer to process meaning it cannot be used for controller feedback [66]. The high-speed camera is also generally more expensive than the other optical sensors given. Also the high-speed camera, like the line-scan camera, requires good lighting conditions for better accuracy. In [66] it

is shown that a high-speed camera that is more expensive than a laser displacement sensor provides less accurate measurements due to the resolution constraints. Ultrasonic sensors are also a potential option that could be used. Ultrasonic sensors use sound waves to bounce off objects to infer their position through triangulation similar to that of laser displacement sensors, however, there has not been a published article yet on their use to measure RA. One use of sound as a measurement is for impact intensity detection as shown in [67] where it is shown how an electret microphone can be used to minimize impact velocities in short-stroke actuators through probability-based optimal control. In [18] where the cost of impact is found through the voltage signal of an electret microphone and used for soft landing of a RA through run-to-run control. With the knowledge of the position and current of the RA, force equations can be solved to know the effective force of the RA. Also with this knowledge other quantities can be derived such as flux, acceleration, and the magnetic field strength from known derived equations. If a position sensor is too costly, then a position estimator can be used. In [68] a position estimator for soft-landing control is built using a Rauch-Tung-Striebel fixed-interval smoother which takes the electrical signals and contact information as observable variables to estimate the position and velocity of the RA.

To control the RA system for precise motion proper measurement devices are required. There are many types of sensors that can be used and each have their pros and cons as stated previously. A summary table highlighting the pros and cons of flux, force, acceleration, and position sensing is outlined in Table 2.2.

Table 2.2: Highlighting the pros and cons of measurement sensing systems for flux, force, acceleration, and position sensing methods.

Method	Pros	Cons
Flux (AC & DC)	<ul style="list-style-type: none"> • Can offer a bipolar output signal • Not affected by system dynamics • All flux area captured (AC) • Passive sensor (AC) • No air gap interference (AC) • Flux measured directly (DC) 	<ul style="list-style-type: none"> • Needs flux-force model for control • Not affected by system dynamics • Localized measurements (DC) • Active sensor (DC) • High temperature sensitivity (DC) • No direct measurement (AC)
Force (AC & DC)	<ul style="list-style-type: none"> • Direct force measurement • Only one sensor req. • No air gap interference • Passive sensor 	<ul style="list-style-type: none"> • Cannot distinguish flux flow direction • Added stiffness to the system • High temperature sensitivity (DC) • Cannot measure static force (AC)
Acceleration	<ul style="list-style-type: none"> • No air gap interference • Output \propto dynamic force • Low mass 	<ul style="list-style-type: none"> • Cannot measure static force • Cannot distinguish flux direction
Position	<ul style="list-style-type: none"> • No air gap interference • No added dynamics • Affordable (line-scan camera) • High fps (high-speed camera) 	<ul style="list-style-type: none"> • Cannot distinguish flux direction • In-line measurements required (laser) • Good lightning required (cameras) • Results not in real-time (high-speed) • Expensive (high-speed)

2.5 Available Control Systems

In order to properly operate the RA a control system needs to be in place to allow for precise positioning. There have been many control systems proposed in the literature that are usually based off a feedforward and feedback model.

2.5.1 Feedforward and Feedback

Combining local sensor-based feedback control and model-based feedforward control can be used to linearize the RA [2]. In order to excite the RA magnetic coils a linear current amplifier is often used to amplify the output from the controller to the correct current value. In [50] a CH808 linear amplifier from HIT-UOI is used to convert the output voltage of the data acquisition card to the excitation current of $-8 \rightarrow +8$ A to operate a Maxwell RA. There are many setups for the controller and what the measurement device utilized is such as current sensing, gap sensing, flux sensing, force sensing, or a combination.

2.5.1.1 Current Sensing

Current through the coils can be measured and sent through a feedback loop to determine the error and controlled through a current controller C_I . A feedforward path FF_I can also be used by using past experiment data or analytical equations as seen in Fig. 2.22 [2].

The main disadvantage with this controller setup is that since the flux density $B(I, g)$ and the $F(B, g)$ rely on the air gap, the controller will not be accurate if the changing air gap is not taken in consideration [2]. Another disadvantage is the complexity to accurately model the current relationship, especially with hysteresis.

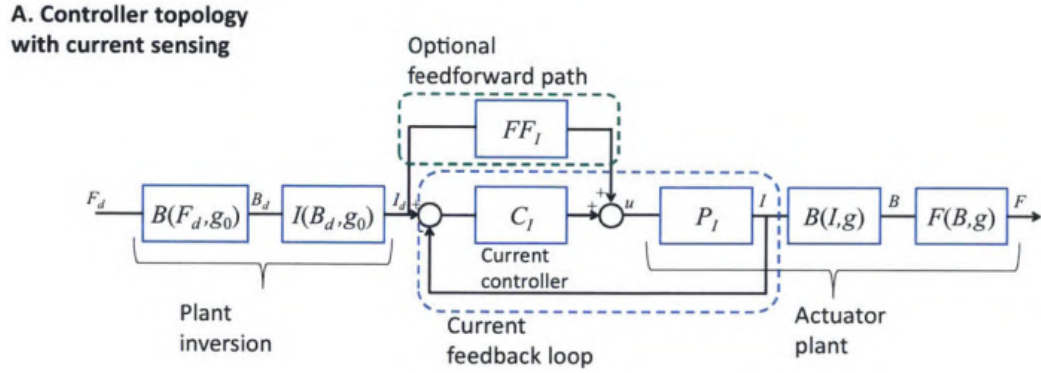


Figure 2.22: A block diagram for RA controller with current sensing feedback and feedforward loop [2].

Additionally, eddy currents can induce a phase lag between current and flux, increasing the complexity [2].

2.5.1.2 Gap Sensing

A way to alleviate the disadvantage of just current sensing control is to add a gap sensor. The signal of the air gap displacement can then be fed into the FF_I to allow for advanced 2-D lookup tables to process the information and an inverse hysteresis model can also be implemented to improve accuracy [2]. A block diagram example is shown in Fig. 2.23.

The disadvantages for adding a gap sensor is that the added complexity of the feedforward model along with the issue that inaccuracies in the gap measurement could produce errors in the feedforward from measurement delay, imperfect coordinate transformation, sensor non-linearity, sensor noise, and the effect of flexible-body dynamics between the sensor location and the air gap [2].

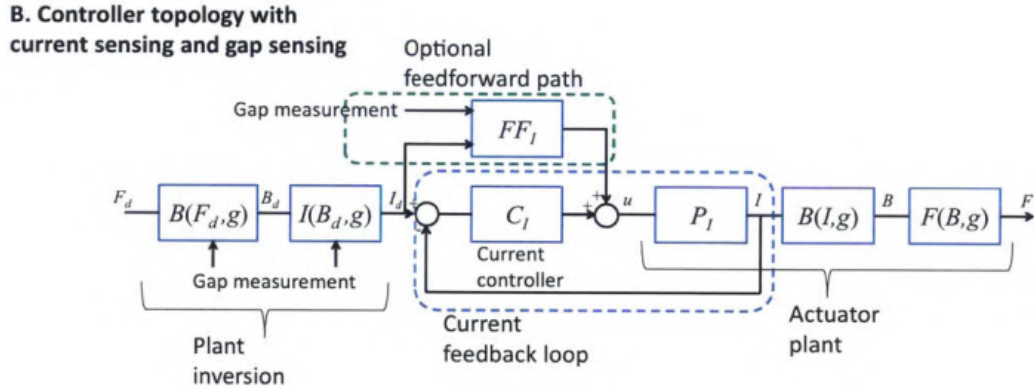


Figure 2.23: A block diagram for RA controller with a current sensing feedback and feedforward loop with a gap sensing feedforward path [2].

2.5.1.3 Flux Sensing

Another way is to use flux instead of current in the feedback and feedforward loop as seen in Fig. 2.24 [2]. In [32] a feedforward compensator using an inverse hysteresis model is used based off flux density measurements from a sense coil.

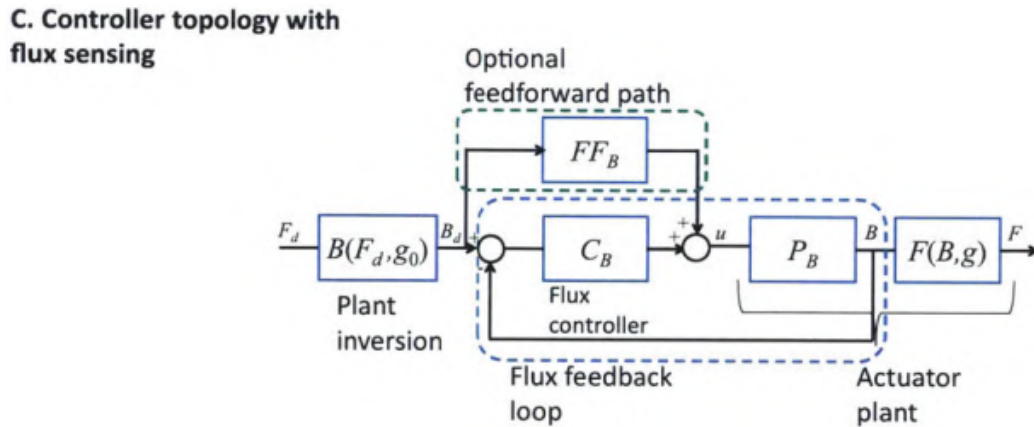


Figure 2.24: A block diagram for RA controller with a flux feedback and feedforward loop [2].

The advantage to having a flux-based controller is it will automatically correct for any flux reduction caused by eddy currents [2]. However, a gap measurement is also recommended as shown in Fig. 2.25 since fringing field can affect the force [2].

D. Controller topology with flux sensing and gap sensing

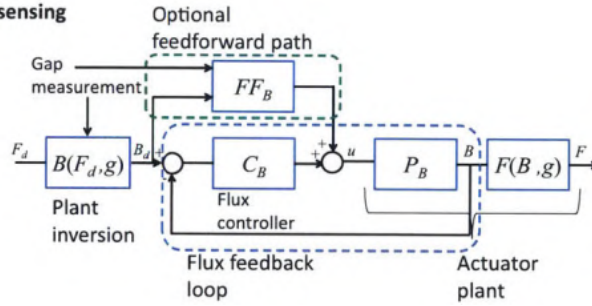


Figure 2.25: A block diagram for RA controller with a flux feedback and feedforward loop with gap sensing [2].

Another configuration is to have both current and flux sensing controllers, as seen in Fig. 2.26, which will increase the controller bandwidth [2].

E. Controller topology with flux sensing and current sensing

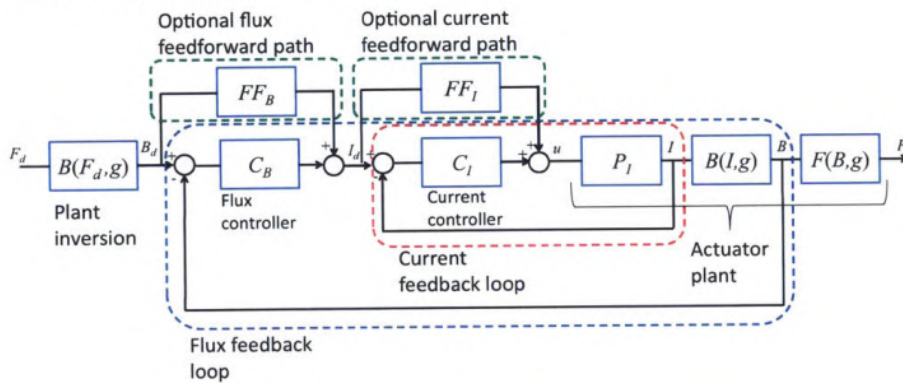


Figure 2.26: A block diagram for a RA controller with a flux feedback and feedforward loop, and a current feedback and feedforward loop [2].

This controller benefits by having additional phase from the current side that compensates for the RA inductance. A gap measurement could also be injected into the feedforward of the controllers to improve controller performance [2].

2.5.1.4 Force Sensing

A force sensor can be used for feedback and feedforward control as shown in Fig. 2.27, however, force sensors face challenges when there is acceleration since it can introduce errors due to the inertial effects [2]. The force sensor also adds additional stiffness to the RA that needs to be factored in and it can compromise the bandwidth and increase gap disturbances [2].

F. Controller topology with force sensing

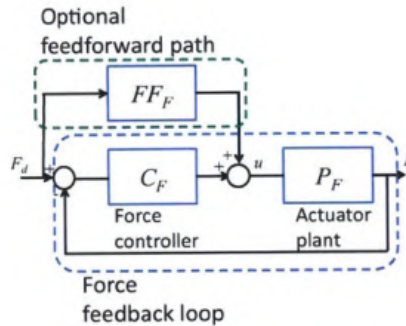


Figure 2.27: A block diagram for a RA controller with a force feedback and feedforward loop [2].

Also the force can only be operated in one direction with this setup. Additional configurations are also possible such as the addition of a current sensing controller helping to allow for higher bandwidth as seen in Fig. 2.28 [2]. A flux sensing controller could also be added for another possible configuration.

There can also be a phase delay between the force measurements and the current due to magnetic hysteresis and eddy currents as shown in [31]. For a 320Hz excitation current the phase delay induced error was reduced by a factor of 2.5 and 5 for a non-hybrid and a hybrid RA respectively with the use of a phase delay model which takes into account the magnetic hysteresis to compensate the force measurement [31].

G. Controller topology with force sensing and current sensing

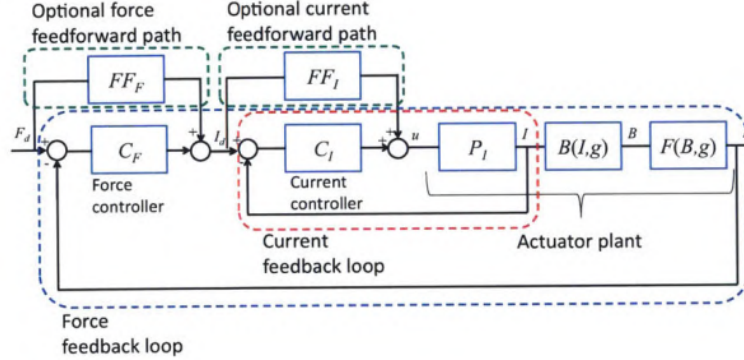


Figure 2.28: A block diagram for a RA controller with a force feedback and feedforward loop and a current feedback and feedforward loop [2].

2.5.2 Controller Algorithm & Identification

In order to control the RA properly, a controller type such as PI, PD, and Shaped-Model Reference (SMR) needs to be chosen along with the identification of the controller parameters through calibration and testing of input signals such as trapezoidal, sinusoidal, triangular which can also help with determining the stability. Another consideration is if a hysteresis model is used and if it is an inverse model and if an observer is used or any robust control considerations.

The usage of a sensing coil voltage control circuitry (SCVCC) with active primary circuit resistance compensation, feedforward voltage injection and a proportional-integral (PI) controller is explored in [25]. A diagram of the SCVCC controller setup is seen in Fig. 2.29.

Next, an inverse feedforward and a feedback control based on the Hall effect sensor is combined with the SCVCC circuit as seen in Fig. 2.30. The measured sensing coil voltage to force output equation is inverted and discretized using backward-euler differentiation to get equation (11) in Fig. 2.30.

The controller is then tuned to eliminate as much root-mean-squared (RMS) flux

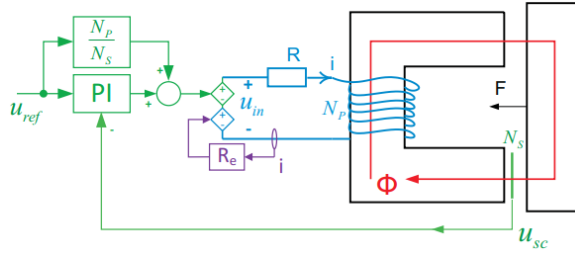


Figure 2.29: SVCC controller schematic from [25].

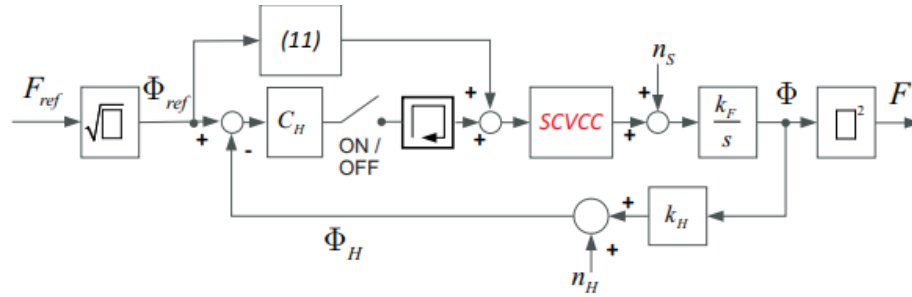


Figure 2.30: Cascaded flux based RA linearization schematic from [25].

noise.

In [25] the force profiles tested all follow a trapezoidal path as seen in Fig. 2.31. It was shown that the Hall feedback helps reduce drift errors, cutting overall error in approximately half. The spikes in error are due to the limited bandwidth of the SCVCC. The paper focuses on the voltage-based linearization which offers low stiffness and high predictability control schemes whereas current-based linearization techniques yield approximately two orders of magnitude larger stiffness for the same actuator [25].

In [17] a parametric hysteresis inverse model is shown to increase the overall accuracy of the feedforward control. It was again shown that the voltage-based control was able to naturally dampen the unknown high frequency air gap and hysteresis disturbances due to the generated back EMF (the smaller the total resistance, the more damping), whereas a current-based source would counteract this damping. The

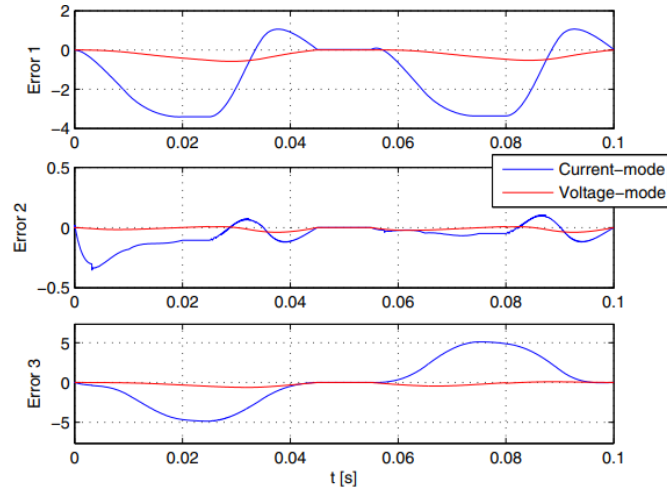


Figure 2.31: The injected trapezoidal force profiles with the SCVCC feedforward controller and Hall feedback, and the corresponding error after several iterations at a fixed air gap of 0.7 mm [25].

errors are highlighted in Fig. 2.32.

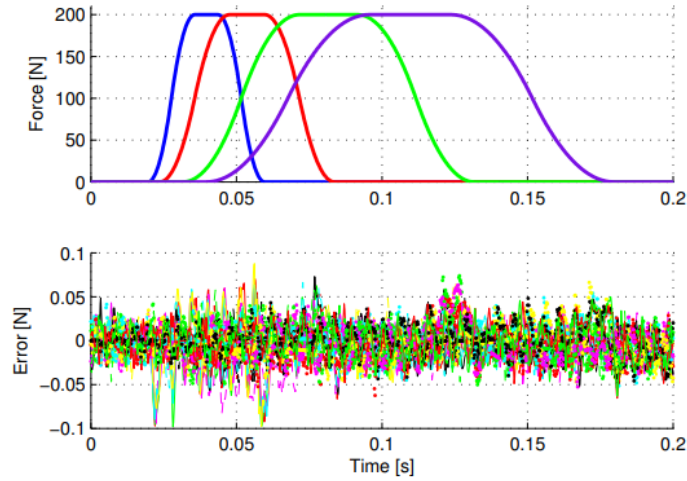


Figure 2.32: Comparison of RA force errors in current and voltage based feedforward control. Error 1 shows no hysteresis compensation, Error 2 shows with hysteresis compensation based on the parametric hysteresis inverse, and Error 3 shows with hysteresis compensation and additional air gap disturbance $\Delta g = 1 \times 10^{-5} \sin(40\pi \times t)$ [17].

In [55] a combination of PI (proportional-integral) and inverse Duhem hysteresis

feedforward controllers are designed to improve system stability and eliminate nonlinearities in a hybrid RA. The feedforward inverse hysteresis model compensation comprises of a lookup table operation as depicted in Fig. 2.33.

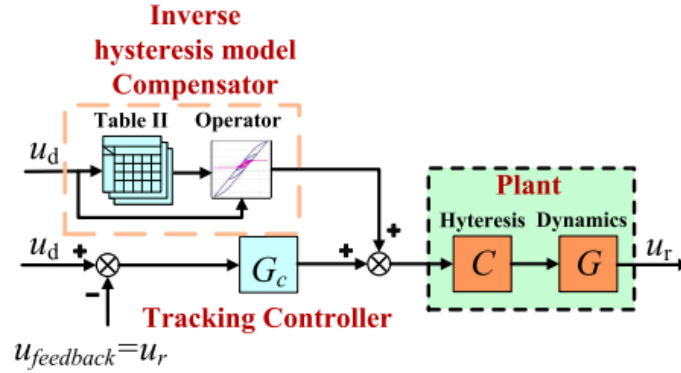


Figure 2.33: Schematic of the PI plus inverse Duhem hysteresis feedforward controller used in [55].

This paper used a triangular wave signal to determine the controller parameters. Triangular waves are similar to trapezoidal waves, however, there is no rest at the crest of the wave and the wave is a series of triangles. The advantage of this is it allows for testing of abrupt changes in the tracking signal's slope. The triangular tracking is shown in Fig. 2.34, it is shown that the optimized hysteresis compensation model reduced tracking errors by 5.33 times when compared to the feedback model alone [55].

In [56, 57] a fractional order proportional-integral (FOPI) is designed and tuned based off an iterative feedback tuning (IFT) algorithm to eliminate tracking error and improve robustness of a Maxwell RA operated XY positioning stage. The error is also further eliminated with the use of a model-free finite impulse response (FIR) filter that is based on non-paramateric frequency domain system identification. Followed by a model-free inversion-based iterative feedforward control (MIIFC) to iterate over

all operational frequencies in the tracking signal which eliminates periodic errors further. This paper also used triangular wave signals for reference trajectories and also tested circular curve outputs of various diameters since it is an XY stage and was able to operate in both x and y and was shown to have excellent tracking with error converging to ± 0.01 mm. In [57] complex curve tracking is implemented with this XY FOPI RA stage on a 2 mm five pointed star and an Archimedes spiral trajectory with a speed of 12.8 and 12.732 mm/s respectively.

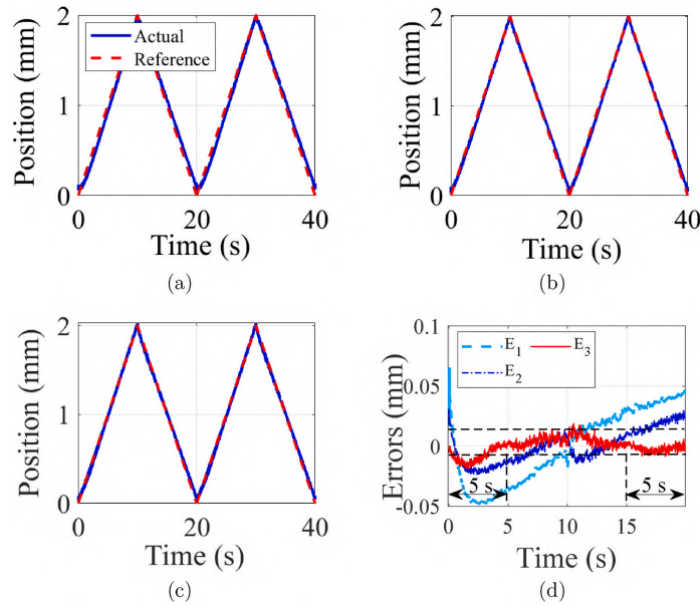


Figure 2.34: Experimental results with a 0.05 Hz triangular wave tracking of a RA with (a) feedback control alone, (b) using unoptimized feedforward control, (c) using the optimized feedforward control. The tracking errors (d) show E1 which represents no hysteresis compensation, E2 represents the unoptimized hysteresis compensation, and E3 is the optimized hysteresis model which has less error than the other models by a magnitude of 5.33 and 1.62 respectively [55].

In [59] an input shaped-model reference control (IS-MRC) is used with a PD and a Lyapunov controller setup as shown in Fig. 2.35 is used to control a flexure-based RA system.

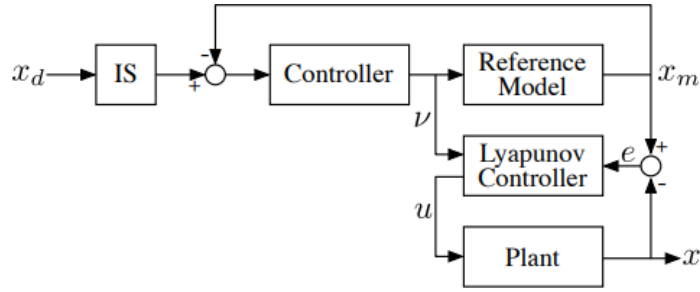


Figure 2.35: IS-MRC control schematic used in [59].

The input shaper (IS) is designed around the natural frequency and damping ratio to generate impulses to counteract residual vibrations [59]. The limitations of using an IS is the delay in the command depending on the duration of the IS. One example of an IS is the Zero Vibration (ZV) shaper, this can be used to eliminate residual vibrations as depicted in Fig. 2.36.

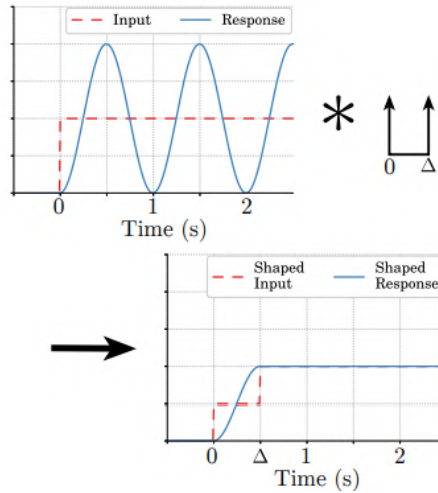


Figure 2.36: Using a ZV shaper eliminates residual vibrations by shaping the input as shown in the step response [59].

This paper [59] proposes an adaptive IS (AIS) that can account for saturation by modifying the input shaper after saturation has occurred. A Lyapunov controller is used to ensure asymptotic stability about $e = 0$ while a proportional-derivative

(PD) controller is used to dampen unwanted system oscillations. A combination of PI feedback control and iterative learning control is used in [53]. PI control eliminates steady-state error through the integration of error over time.

A run-to-run controller with bayesian optimization (R2R-BO) is used in [18] which provides a robust controller with the help of Gaussian process regressors which can converge rapidly to an optimal solution based on past data. The controller also does not require position sensors and is shown to control the RA based off coil current which makes the position dynamics independent on the coil resistance, making it more robust to temperature changes and works better than voltage-based control.

In [39] a dual-stage E-core RA an integral sliding mode control (ISMC) algorithm is derived for flux control along with a heuristic optimization-based Bouc-Wen model to capture the hysteresis in the RA which was treated as a nonlinear internal disturbance to the system. It was shown through simulation results that the model can overcome hysteresis without accurate known parameters. When compared to a standard PI controller, a combination of PI and hysteresis combination, the ISMC showed impressive mean error reduction in the control performance as shown in Table 2.3.

Table 2.3: Comparison of control performance (mean error, maximum error, and standard deviation) of various flux controllers of a RA system as shown in [39].

Controller	Mean Error (T)	Max Error (T)	Standard Dev. (T)
Pure PI Control	5.0823e-4	0.0056	0.0028
PI + Hysteresis	1.1222e-5	0.0029	1.1381e-4
ISMC	7.8513e-8	0.0027	4.1896e-5

2.5.3 Feedback Linearization

A nonlinear system can be transformed to a linear system with feedback linearization by feeding back a measured signal as an input to the transformation. This allows standard linear feedback control techniques to be used [2]. By having the inverse of the nonlinear plant's transfer function, $P(v, x)$, before the plant, the system output would be effectively 1 since $P^{-1}P = 1$ as seen in the block diagram in Fig. 2.37 [2].

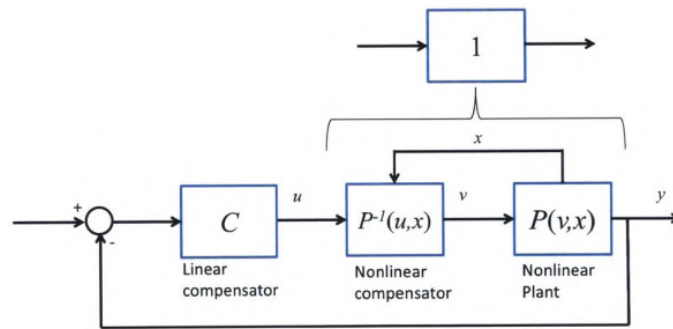


Figure 2.37: A block diagram of a controller with feedback linearization [2].

For the RA, an example would be the controlling the flux density via feedback linearization as shown in Fig. 2.38 [2]. The disadvantage to feedback linearization is it requires an accurate plant model and is sensitive to plant disturbances [2]. Examples are showcased in [30, 64, 69]

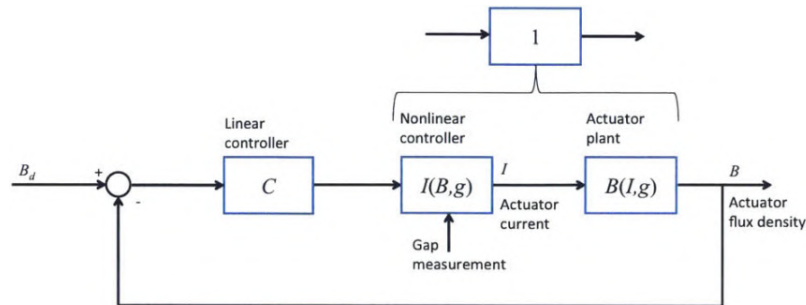


Figure 2.38: RA flux density controller with feedback linearization [2].

The main advantage is being able to now use a linear controller such as a PID to control the now linearized plant/actuator. In [70], feedback linearization is used on a dual-stage hybrid style RA to allow the RA to be controlled via PID. A feedforward controller was also included along with a notch filter to suppress bandwidth limiting resonance. This setup was able to accomplish a closed loop bandwidth of 335Hz with 2nm positioning resolution for a $60\mu\text{m}$ range using a capacitive displacement sensor (which has a nominal resolution and linearity of 1 nm and 0.25%, respectively) [70]. A challenge found was with slower scanning, a jumping motion occurred due to the coil switching between actuators. A block diagram of the control strategy used is seen in Fig. 2.39.

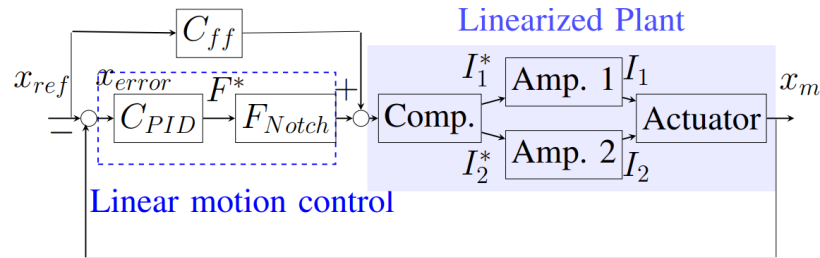


Figure 2.39: Block diagram for a feedback linearization controller on a dual-stage hybrid RA. [70]

2.5.4 Iterative Learning Control

Iterative learning control (ILC) is a method where trajectory data is stored and through the memory of past trials the ILC method aims to improve tracking performance for the next trial [2]. It learns what input is required to reduce the tracking error towards zero. Feedback from each trial is used to update future feedforward signals. The error is passed through a learning controller, L , and added to the k^{th} iteration of the feedforward input, u_k . This is then processed through a ‘robust-

ness' low-pass filter, Q , and added to memory for the feedforward input to the $k + 1$ iteration, u_{k+1} [2]. This can be seen in Fig. 2.40 [71].

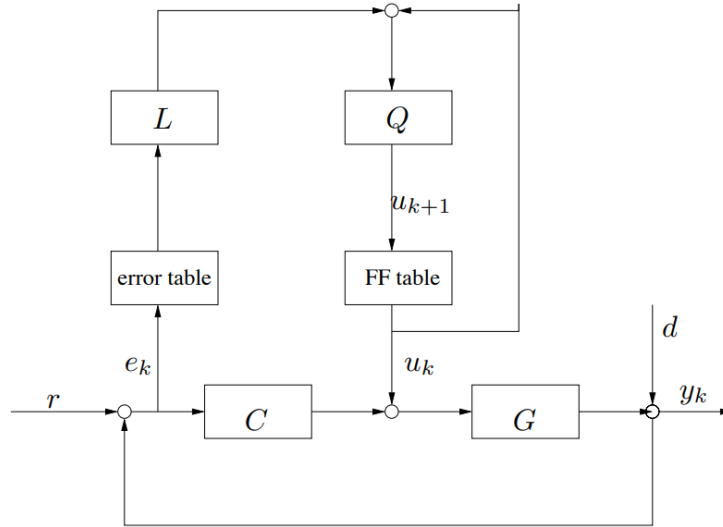


Figure 2.40: A closed-loop ILC block diagram [71].

Modeling-free inversion-based iterative control (IIC) is used in [53] to decrease tracking error in a hybrid RA and after the 15th learning iteration, the error was reduced by a factor 396 at most. The system was able to achieve an error of 10 nm (RMS) for a 1 Hz triangular motion of 1.6 mm range and a 100 Hz triangular motion of 10 μm .

2.5.5 Hysteresis Considerations

Since the RA relies on the magnetization of ferromagnetic materials, a phenomenon known as *hysteresis* occurs [7]. When a magnetic field flows through ferromagnetic material, the atomic dipoles align themselves with the flux flow and even when the field is removed, part of the alignment will remain, leaving the material magnetized. This will affect the B-H curve depending on magnetizing and demagnetizing condi-

tions. This can be shown in Fig. 2.41, where the magnetic field strength H and the flux density B correlate with one another with a hysteresis loop consideration. A hysteresis model can be proposed to model the system better and reduce potential errors in trajectory tracking.

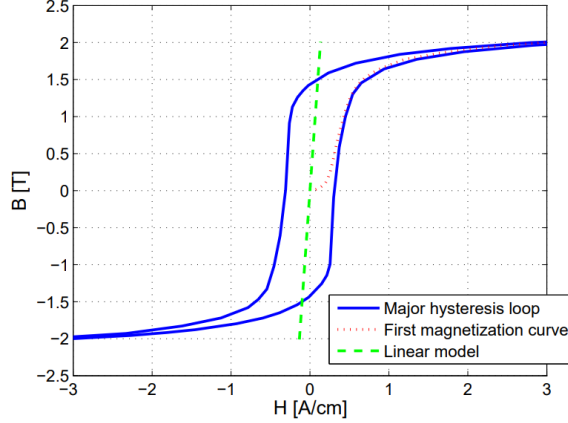


Figure 2.41: Hysteresis loop model of cobalt-iron magnetic flux density B vs. magnetic field strength H from [7].

To represent the hysteresis influence analytically, a hysteretic component, H_{hyst} , can be added to the magnetic core field strength, H_c [7]:

$$H_c = \frac{B}{\mu_0 \mu_r} + H_{hyst} \quad (2.14)$$

Which leads to the magnetic flux density, B :

$$B = \mu_0 \frac{Ni - H_{hyst} l_m}{\frac{l_m}{\mu_r} + 2g} \quad (2.15)$$

This shows the amount of error in the force will vary with air gap size g , actuator size l_m , and total force F [7].

There are models that can be used to represent hysteresis. These include the Duhem model [50], Preisach model, Prandtl-Ishlinskii model, Chua model [72], Jiles-

Atherton model [73], Dahl model [74], Bouc-Wen [75], and the Krasnosel'skii-Pokrovskii model [76].

The Duhem model requires experimental data to be interpolated and processed and mapped on to hysteretic parameters [77]. An example of a successful Duhem model identification that was able to reduce the tracking error of a hybrid RA setup by 5.33 and 1.62 times smaller than that of regular feedback control and unoptimized hysteresis model feed-forward control respectively [50].

The Preisach model is formulated through a set of infinite hysteresis operators $\hat{\gamma}_{\alpha\beta}$ each representing a rectangular loop which switches between one and zero based on the α and β inputs and the Preisach function $\mu(\alpha, \beta)$ [78, 79]. The Preisach model requires experimental identification through extrema points to map and determine the hysteretic system parameters as done in [78] for an E-Core RA. The accuracy of the Preisach model deteriorates as the input frequency and pre-loading forces of the actuator are increased [80]. A hybrid dynamical model for RA was developed using a derived inverted Preisach model in [48].

The Prandtl-Ishlinskii (PI) hysteresis model is based on the superposition of play or stop operators through a threshold variable [80–82]. This model cannot express asymmetric hysteresis loops or saturated outputs. The main benefit of the PI model over the Preisach model is that the inverse can be attained analytically whereas the Preisach requires experimental data [81]. This allows the PI model to be used in a feedforward controller.

The PI model was used along with the Chua model in [32] to create a hybrid two-stage model for rate-dependent inverse hysteresis in a RA. The paper shows that the two-stage model can alleviate the rate-dependent hysteretic non-linearities effectively and more accurately than just the Chua model and direct inverse model (DIM) at higher frequencies.

The Chua model estimates dynamic hysteresis loops in systems with the use of a potential energy restoring function and taking into account the dissipation energy of the loop [72, 83]. The Chua model is used successfully in [32] with a combination of the PI model.

The Jiles-Atherton (JA) ferromagnetic hysteresis model is an equation that describes theoretically the initial magnetisation curve and hysteresis loop parameters [73]. This model uses a combination of irreversible and reversible magnetization parts that is based off the idea of domain wall motion

A variation of the JA hysteresis model was used successfully to model RA dynamics in [63] and was shown that the simulated results match well with the experimental findings. The JA model was also compared here to the generalized Preisach model and after 1000 repetitions, the mean computation time was approximately ten times faster [63].

2.6 Discussion

Overall, the RA provides many benefits including: a higher force density, lower heat dissipation, and lower mass than traditional electromagnetic actuators. The main challenge is in the control of the RA and the hysteresis of the system. It is recommended that RA be used in millimeter ranged applications that require high acceleration since lower air gaps offer higher force efficiencies. Going beyond the millimeter range increases flux fringing, which can lead to an unstable system if not taken into account. The configuration is also important and depends on the overall application. Using a cobalt-iron (Co-Fe) for the RA material also provides the best force density output due to higher saturation flux densities that can be realized. It is shown to be beneficial to use the tape-wound cut core as shown in Fig. 2.4 to help the grain

orientations align with the magnetic flux path to increase the core permeability which would increase the RA efficiency [2]. Also, since most applications will require bidirectional motion, it is recommended that a dual core approach is used or a spring or flexure utilized to allow for forces in the opposing direction. As for the measurement device it is recommended to use a non-invasive (not interfere with the air gap) and passive sensing element (no extra power required to power the sensor). Having two sensors is also beneficial and can help with the feedforward controller that should be implemented. The sense coil, as described in Section 2.4.1, allows the controller to smoothly operate about the zero-flux point, mover acceleration will not affect readings, no extra stiffness or mass, passive sensor, less noise, will not affect air gap range, and have the ability to correct for any flux reduction caused by eddy currents if used in the controller. If a position sensor or observer is not feasible then it is possible to just use current as shown in [18] to control the RA effectively. Section 2.5.1.3, goes over how flux sensing can be used in the control. It is recommended to also use the current in the controller since it is easy to get the current readings and a flux current controller can be implemented as shown in Fig. 2.26. It would also be beneficial to use feedback linearization as described in Section 2.5.3. If the application is repetitive in the working trajectory, then it is recommended to also include ILC as described in Section 2.5.4. This can help the feedforward controller section of the controller by learning from past trajectory paths.

2.7 Conclusions of the Chapter

The RA works by exploiting the reluctance force property in air gaps between stator core and mover elements. The stator creates the magnetic flux which generates an attractive magnetic force between the stator and mover, causing the mover to acceler-

ate. The force has a nonlinear gap dependency and is affected by hysteresis and other non-linearities in the magnetic flux. The RA is shown to be able to generate an efficient force that can be used in high-acceleration applications with millimeter ranges. This is ideal for the short-stroke stage in photolithography machines for example.

The RA has many configurations which include C-Core, E-Core, Hybrid, and Plunger type designs. Each design has its merits as shown in Section 2.2. The main issue with the RA is the complex non-linear nature and the requirement of accurate models and controllers to help linearize the RA system. Many researchers have made great progress in the advancement of the RA and ways to counteract this nonlinear behaviour with the use of hybrid dynamical models to accurately model the hysteresis, flux fringing, and eddy current effects. The main proposed application is for use in photolithography machines where high acceleration and precision is vital for the short-stroke stage.

Chapter 3

Investigating the effect of the Mean Path Length on RA Output Force Characterization

This chapter¹ investigates the effect of the flux's mean path length (MPL) on the RA's analytical model. It determines the circumstances where the model neglecting the MPL is valid. The analysis is carried out for both C-Core and E-Core RAs; the analytical results are calculated using MATLAB, then validated against a finite element model simulation using COMSOL Multiphysics. Additionally, the experimental results of the magnetic force of C-Core and E-Core RAs are presented and compared with the analytical model. The comparison is obtained under different input currents and air gaps for two different ferromagnetic materials. It can be concluded that the analytical model is valid only for air gaps with a relatively high air gap displacement and for small air gaps, considering the MPL is necessary for accurate results. This means that whenever the RA is proposed for high-precision motion system applications, it is essential that the analysis takes into account the effect of the MPL.

¹A version of this chapter was published in The Review of Scientific Instruments (AIP) [6].

3.1 Introduction

High precision motion systems are essential in various devices such as atomic force microscopes [84, 85] and lithography machines for the semiconductor industry [86]. In lithography machines, the precision motion system of the wafer scanner is driven by six Lorentz actuators to obtain a multi-degree range of motion [87]. The main advantages of the Lorentz actuators are a linear force-current relation and zero-stiffness since the force is not position dependent [88, 89]. The new desired requirements of lithography machines are improved accuracy, efficiency, and faster production of integrated circuits to meet the rapidly increased demands of the micro/nano technologies [90]. To improve Lorentz actuators under the new requirements of the next generation of lithography machines requires an increased actuator size which increases heat dissipation [91]; also, the Lorentz actuators reach their physical limits to generate a higher force density [92]. RAs are being designed and proposed for use in the next generation of lithography machines [86, 93–95]. RAs induce a magnetic field from a current and produce higher forces with a smaller actuator size. However, the RA has a nonlinear force as a function of the input current and the air gap, negative stiffness, and nonlinearities such as hysteresis, fringing, and eddy currents [5, 96]. Various methods exist to mitigate the nonlinear effects of RAs, through PID control [97], observer design [98], complex hysteresis modelling [99], and optimal design parameters selection [94, 95].

While precise finite element analysis (FEA) modelling is used extensively in computing the dynamics of RAs [100], as well as hybrid RAs [101], in contrast, an equivalent magnetic circuit (EMC) based model is favoured over the more accurate FEA due to lower computational requirements [102] and applicability in real-time measurements such as in [103]. The mean path length (MPL) is introduced when considering

the flux through the core in a EMC analytical model. This term is present in the denominator of the force equation and consists of the MPL being divided by the relative magnetic permeability of the core, which has a nonlinear magnitude on the order of thousands. Under certain conditions, this term is neglected due to its smaller magnitude and the benefit of neglecting the nonlinear magnetic permeability. Researchers have not reached a consensus regarding the inclusion of the MPL term in high-precision motion systems. In some cases, the term containing the MPL is assumed to approach zero as it is divided by the higher magnitude relative magnetic permeability; for example, [103–105]. In [102], the reluctance of the core is stated to be linear, which neglects the nonlinear effects of saturation arising from the core material. Other works include the MPL in their analysis. In [103], a RA is modelled using a hybrid lumped-parameter state-space model accounting for the nonlinearities that exist in the core, including eddy currents, flux fringing, magnetic hysteresis, and saturation, where analysis includes the MPL term. A real-time model for hysteresis in [106] considers the MPL while using the average values for magnetic field density through the core, which results in accurately modelling the behaviour of the actuator below saturation.

The validity and effects of neglecting or including the MPL term have not been thoroughly analyzed, particularly concerning high-precision motion systems and motion scanning applications. An analysis of the MPL’s effects on the analytical modelling of a RA is presented in this chapter to determine under what conditions it should be incorporated. A range of parameters will be tested to determine the effect of the value of these parameters on the necessity of the MPL. Two standard geometries, C-Cores and E-Cores, will be considered to ensure the results are useful across varying geometries as in [107]. In [108], an open-loop steady-state model that can estimate the hysteresis effects of an E-core actuator based on the phase delay of flux

variations is found.

This chapter discusses the overall methodology, including the mathematical modelling of two standard geometries, C-Core and E-Core RA in Section 3.2, the comparison between the FEA, the analytical model, and the experimental study is presented in Section 3.3. Lastly, Section 3.4 concludes this chapter's results.

3.2 Modeling of RA

A RA is a type of electromagnetic actuator that consists of two parts: a fixed part called a stator, and a moving part called a mover. The RA has three main configurations: C-core, E-core, and plunger-type. This study investigates the impact of considering the MPL and neglecting the MPL in the analytical model of the C-core and E-core RAs. The magnetic force in the air gap between the stator and the mover is formulated based on the equivalent magnetic circuit (EMC) concept. The comparisons are carried out between the analytical models using MATrix LABoratory (MATLAB) and the finite element analysis (FEA) using COMputer SOLution (COMSOL) Multiphysics.

3.2.1 C-Core RA

The C-Core has been studied in papers such as in [2, 3, 7, 15, 17–25]. The schematics diagram of the C-core RA and the equivalent magnetic circuit are shown in [Figure 3.1](#). The magnetic flux Φ_C and the magnetic force F_C can be formulated based on the analysis of the EMC. Consider the Magnetomotive Force (MMF) Ni is the source of the EMC, the loop of EMC is expressed as

$$Ni = (\mathcal{R}_c + 2\mathcal{R}_g) \Phi_C \quad (3.1)$$

where N is the coil number of turns, and i is the coil current. The reluctance of the magnetic core \mathcal{R}_c and of the air gap \mathcal{R}_g are expressed by

$$\mathcal{R}_c = \frac{l_c}{\mu_o \mu_r(B, H) A_c}, \quad \mathcal{R}_g = \frac{g}{\mu_o A_c} \quad (3.2)$$

where A_c is the cross-sectional area of the core, g is the air gap between the stator and the mover, $\mu_o = 4\pi \times 10^{-7}$ is the permeability of free space, $\mu_r(B, H)$ is the relative permeability based on the BH-curve of the ferromagnetic material, and l_c represents the MPL of the magnetic flux which is calculated by $l_c = 2L + 2W - 2a$. Thus, the magnetic flux Φ_C and the magnetic flux density B_C can be expressed as

$$\Phi_C = \frac{\mu_o A_c N i}{\frac{l_c}{\mu_r(B, H)} + 2g}, \quad \text{and} \quad B_C = \frac{\Phi_C}{A_c} = \frac{\mu_o N i}{\frac{l_c}{\mu_r(B, H)} + 2g} \quad (3.3)$$

The stored energy in the field is presented in terms of the magnetic flux Φ_C and the input current i as

$$W_C(\Phi_C, i) = \frac{1}{2} N \Phi_C i = \frac{1}{2} \frac{\mu_o A_c N^2 i^2}{\frac{l_c}{\mu_r(B, H)} + 2g} \quad (3.4)$$

then, the magnetic force generated in the air gap can be formulated using the derivative of the stored energy in the field as

$$F_C(i, g) = \frac{\partial W_C}{\partial g} = -\frac{\mu_o A_c N^2 i^2}{\left(\frac{l_c}{\mu_r(B, H)} + 2g\right)^2} \quad (3.5)$$

where the negative sign indicates that the mover will always move toward the stator and the magnetic force decreases with increasing the air gap.

Considering the ferromagnetic material has high relative permeability $\mu_r \gg \mu_o$, the MPL can be neglected where $\frac{l_c}{\mu_r} \approx 0$ and $\mu_r \gg \frac{l_c}{2g}$. Thus, the magnetic flux and

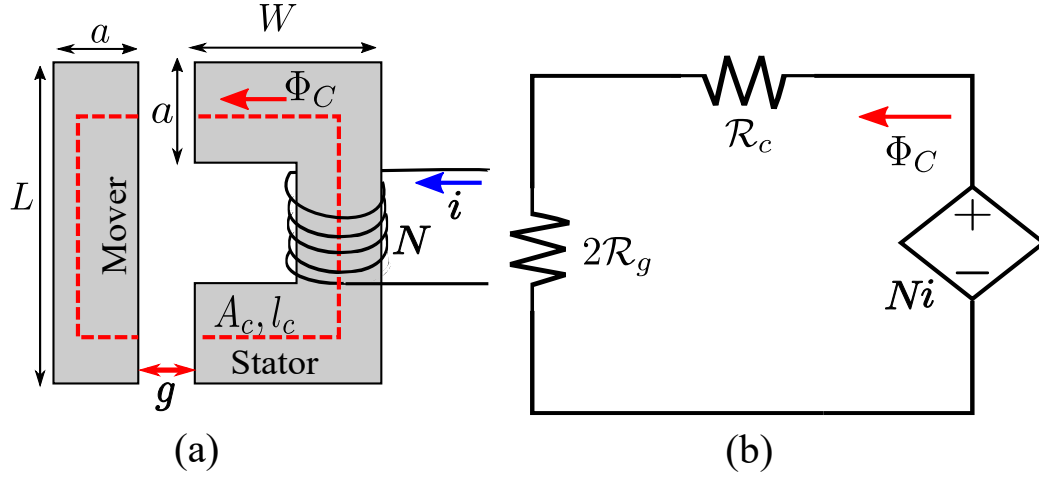


Figure 3.1: (a) Schematic diagram of C-core reluctance with (b) Equivalent magnetic circuit.

the magnetic force can be approximated to

$$B_{C_a} \approx \frac{\mu_o Ni}{2g}, \quad F_{C_a} \approx \frac{\mu_o A_c N^2 i^2}{4g^2}. \quad (3.6)$$

3.2.2 E-Core RA

E-Core setups are covered in the following papers [2, 4, 7, 23, 26–39]. The schematics diagram of the C-core RA and the equivalent magnetic circuit are shown in Figure 3.2. The magnetic flux Φ_E and the magnetic force F_E can be formulated based on the analysis of the EMC. Consider the Magnetomotive Force (MMF) Ni is the source of the EMC, and it can be expressed as

$$Ni = \left[\frac{\mathcal{R}_{ul}\mathcal{R}_{bl}}{\mathcal{R}_{ul} + \mathcal{R}_{bl}} + \mathcal{R}_{cl} \right] \Phi_E \quad (3.7)$$

where \mathcal{R}_{ul} is the equivalent reluctance of the upper lump, \mathcal{R}_{cl} is the equivalent reluctance of the center lump, and \mathcal{R}_{bl} is the equivalent reluctance of the bottom lump.

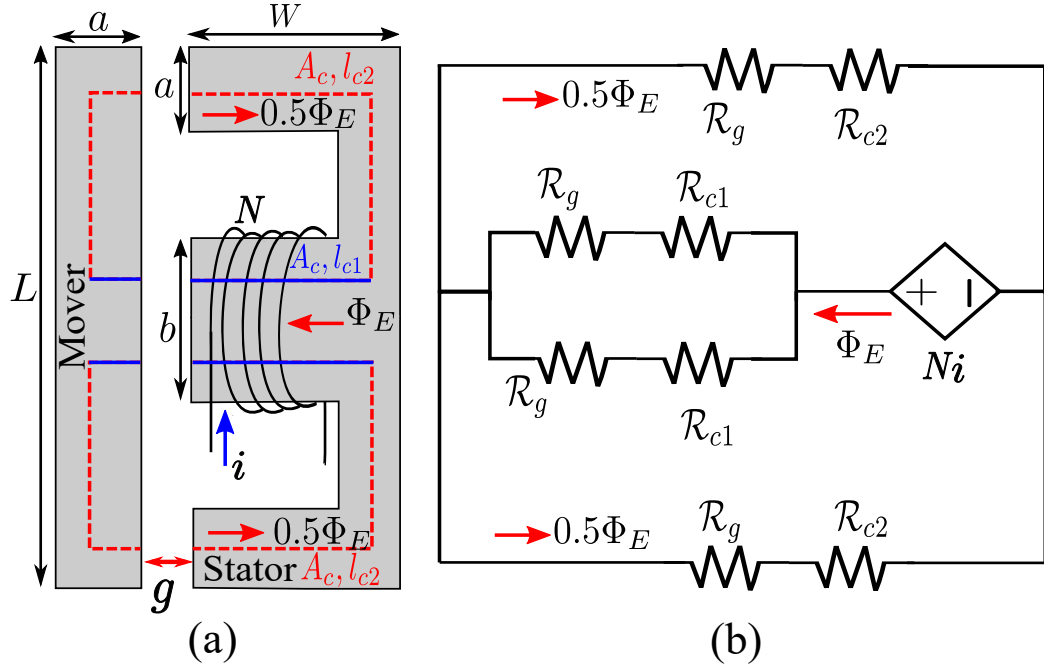


Figure 3.2: (a) Schematic diagram of E-core reluctance with (b) Equivalent magnetic circuit considering two parallel paths.

The equivalent reluctance for each lump is expressed as

$$\mathcal{R}_{ul} = \frac{l_{c2}}{\mu_o \mu_r(B, H) A_c} + \frac{g}{\mu_o A_c}, \quad (3.8)$$

$$\mathcal{R}_{cl} = \frac{1}{2} \left(\frac{l_{c1}}{\mu_o \mu_r(B, H) A_c} + \frac{g}{\mu_o A_c} \right), \quad (3.9)$$

where $l_{c1} = W$ and $l_{c2} = L - 2a + W$. Then, the magnetic flux Φ_E can be calculated as

$$\Phi_E = \left[\frac{1}{2} \mathcal{R}_{ul} + \mathcal{R}_{cl} \right]^{-1} Ni, \quad (3.10)$$

$$\Phi_E = \left[\frac{0.5l_{c1}}{\mu_o \mu_r(B, H) A_c} + \frac{0.5l_{c2}}{\mu_o \mu_r(B, H) A_c} + \frac{g}{\mu_o A_c} \right]^{-1} Ni, \quad (3.11)$$

Thus, the magnetic flux Φ_E and the magnetic flux density B_E can be expressed

as

$$\Phi_E = \frac{\mu_o A_c N i}{\frac{l_{c1}+l_{c2}}{2\mu_r(B,H)} + g}, \quad \text{and} \quad B_E = \frac{\Phi_E}{2A_c} = \frac{1}{2} \left(\frac{\mu_o N i}{\frac{l_{c1}+l_{c2}}{2\mu_r(B,H)} + g} \right) \quad (3.12)$$

The stored energy in the field is presented in terms of the magnetic flux Φ_E and the input current i as,

$$W_E(\Phi_E, i) = \frac{1}{2} N \Phi_E i = \frac{1}{2} \frac{\mu_o A_c N^2 i^2}{\frac{l_{c1}+l_{c2}}{2\mu_r(B,H)} + g} \quad (3.13)$$

then, the magnetic force generated in the air gap can be formulated using the derivative of the energy as

$$F_E(i, g) = \frac{\partial W_E}{\partial g} = - \frac{\mu_o A_c N^2 i^2}{2 \left(\frac{l_{c1}+l_{c2}}{2\mu_r(B,H)} + g \right)^2} \quad (3.14)$$

where the negative sign indicates that the mover will always move toward the stator and the magnetic force decreases with increasing the air gap.

Considering the ferromagnetic material has high relative permeability $\mu_r \gg \mu_o$, the MPL can be neglected where $\frac{l_{c1}+l_{c2}}{2\mu_r} \approx 0$ and $\mu_r \gg \frac{l_{c1}+l_{c2}}{2g}$. Thus, the magnetic flux and the magnetic force can be approximated to

$$B_{E_a} \approx \frac{\mu_o N i}{2g}, \quad F_{E_a} \approx \frac{\mu_o A_c N^2 i^2}{2g^2}. \quad (3.15)$$

3.3 Results and Discussion

This section shows the analysis of the MPL effect on the characterization of the output force of the RA. Different comparisons are conducted between the magnetic force using the FEA and the analytical models using (3.5), (3.6), (3.14), (3.15). The

Table 3.1: The parameters of the C-core and E-core RA.

Parameter	Value	Mean Path Length	Value
N	400	l_c	350 mm
a	25 mm	l_{c1}	60 mm
b	50 mm	l_{c2}	150 mm
L	140 mm		
W	60 mm		
A_c	625 mm ²		

magnetic force is obtained under different input currents i and over a range of air gap g for two different ferromagnetic materials.

The dimensions of the C-core actuator shown in [Figure 3.1](#) and E-core actuator shown in [Figure 3.2](#) are given in [Table 3.1](#). The two ferromagnetic materials are Iron-Cobalt-Vanadium (Hiperco-50) and Electrical Steel(M-19) with magnetic properties and characteristics presented in [Figure 3.3\(a\)](#) and [3.3\(b\)](#), respectively [109]. It is evident from [Figure 3.3](#) that Hiperco-50 and M-19 produce magnetic fluxes of 2.3 T each, and their maximum relative permeabilities are about 7500 and 8000, respectively. The BH-curve is used to calculate the corresponding value of the relative permeability at given magnetic flux B and magnetic field H .

3.3.1 Simulation results

The FEA model of the C-core RA is obtained using COMSOL based on the given dimensions and ferromagnetic materials. The results are obtained for input currents values of $i = \{0.15, 0.25, 0.5, 1, 1.5, 2\}$ A and the air gaps values of $g = \{0.1, 0.2, 0.3, 0.4, 0.55, 0.7, 0.85, 1, 1.2, 1.4, 1.6, 1.8, 2\}$ mm. [Figure 3.4](#) shows the magnetic flux distribution around the MPL for input current of $i = 1.5$ A at air gap $g = 0.55$ mm

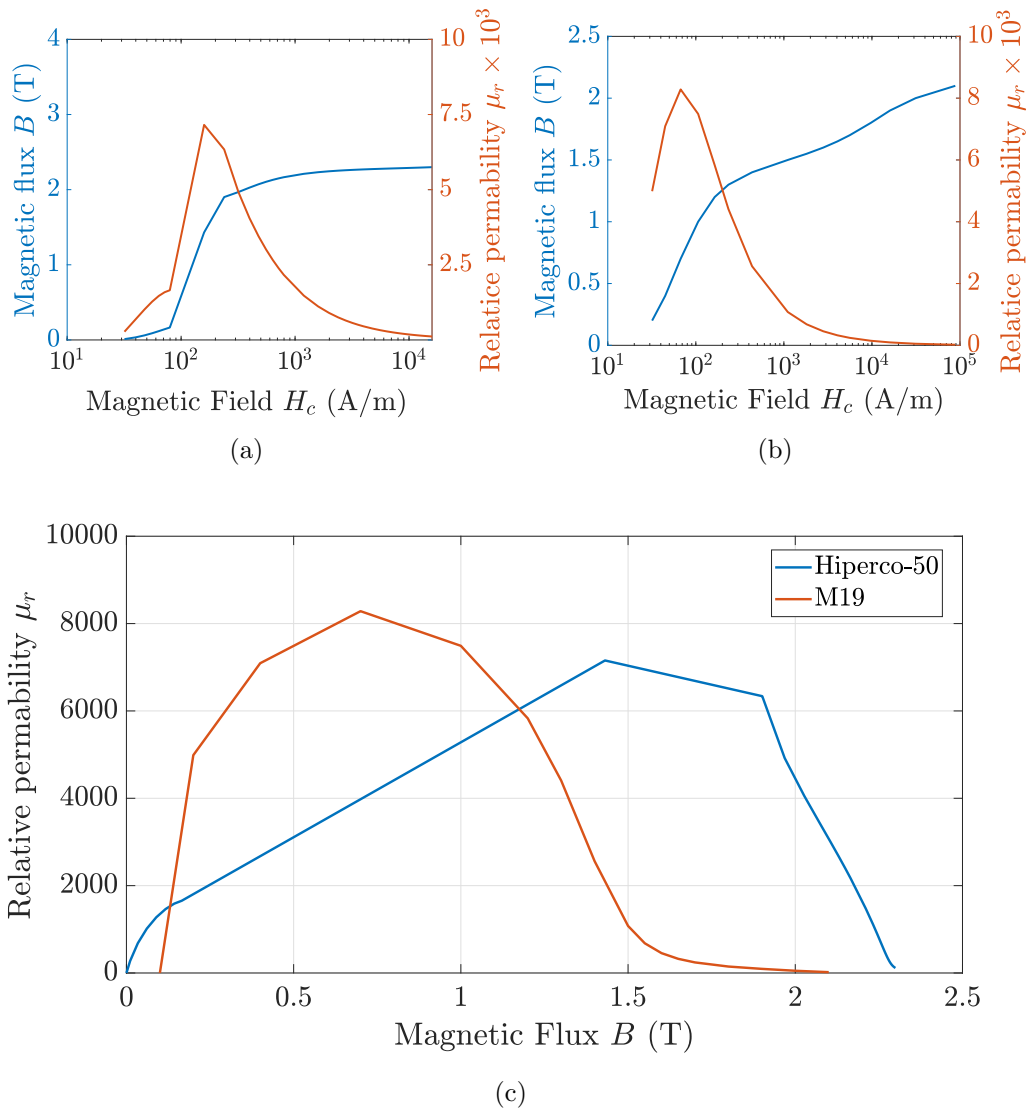


Figure 3.3: The BH-curve with the relative permeability for ferromagnetic materials (a) Iron-Cobalt-Vanadium (Hiperco-50); (b) Electrical Steel (M-19); and (c) the relative permeability as a function of the magnetic flux.

for Hiperco-50 and M-19. The figure illustrates that M-19 has a better magnetic flux distribution around the MPL than Hiperco-50. Also, it can be noticed that Hiperco-50 generates higher magnetic flux, which allows generating higher magnetic force than M-19. The magnetic force using the FEA is compared with the analytical models (3.5) and (3.6) as shown in Figure 3.5.

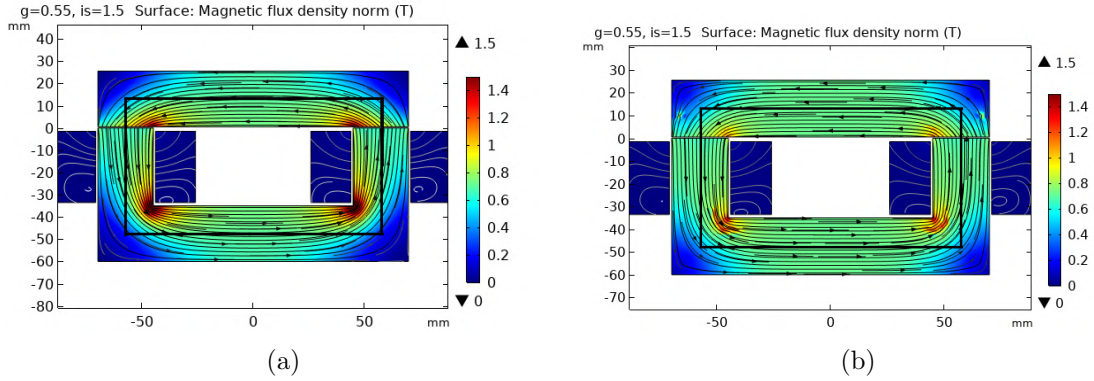


Figure 3.4: The magnetic flux B_C of the C-core RA with input current i of 1.5 A at air gap g of 0.55 mm for ferromagnetic materials (a) Hiperco-50; and (b) M-19.

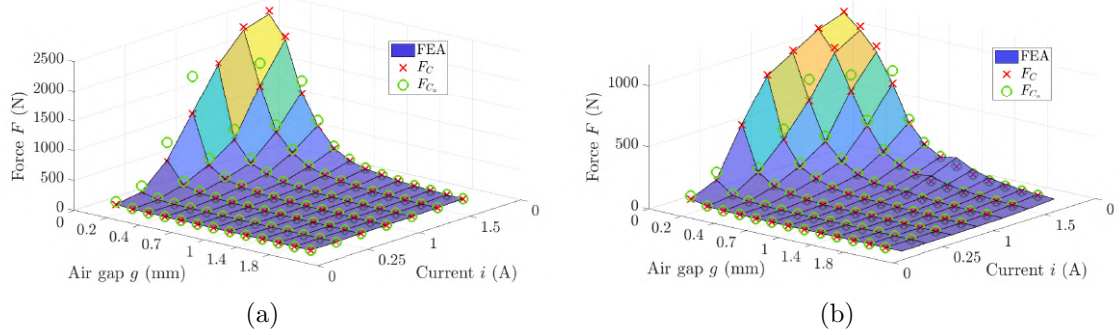


Figure 3.5: The comparison of C-core RA between the magnetic force of FEA, model (3.5), and model (3.6) for (a) Hiperco-50; and (b) M-19.

To compare these results, The percentage errors in the magnetic force are given by

$$\varepsilon_C(\%) = \frac{F_{\text{FEA}} - F_C}{F_{\text{FEA}}} \times 100, \quad (3.16)$$

$$\varepsilon_{C_a}(\%) = \frac{F_{\text{FEA}} - F_{C_a}}{F_{\text{FEA}}} \times 100. \quad (3.17)$$

where F_{FEA} is the generated force of FEA model, F_C is the force of the analytical model (3.5), and F_{C_a} is the force of the approximated analytical model (3.6). [Figure 3.6](#) illustrates the percentage of error as function of the air gap, g .

According to [Figure 3.6](#), it can be observed that Hiperco-50 has a percentage of

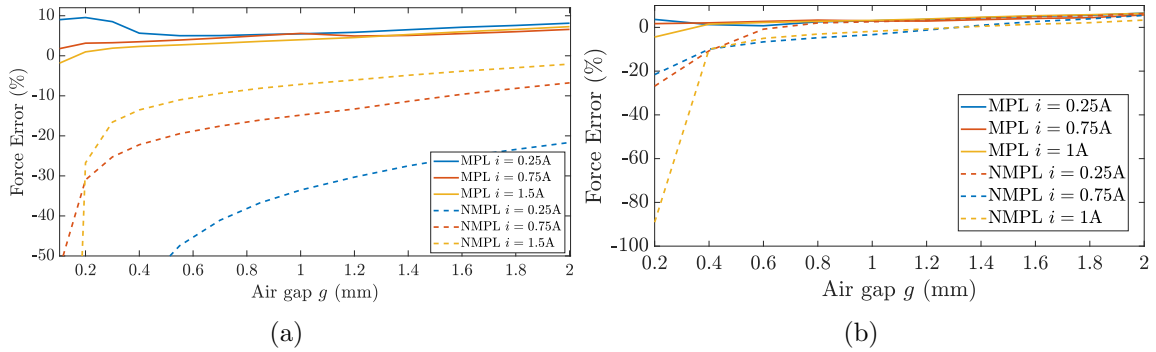


Figure 3.6: The relative force error of C-core RA in (3.16) for (a) Hiperc-50; and (b) M-19.

error less than 10% using the analytical model (3.5), while the M-19 has a percentage of error less than 5%. Also, Figure 3.6 illustrates that the approximated model (3.6) is valid only for M-19 at air gap range of $g > 1$ mm, where the percentage error is less than 15%. While using Hiperc-50, the approximated model shows a higher percentage error larger than 10%, and the results will be inaccurate using the approximation.

As the C-core RA, COMSOL is used to build the FEA model of the E-core RA. The input current and the air gap values are considered as $i = \{0.15, 0.25, 0.5, 1, 1.5, 2\}$ A and $g = \{0.1, 0.2, 0.3, 0.4, 0.55, 0.7, 0.85, 1, 1.2, 1.4, 1.6, 1.8, 2\}$ mm. The distribution of the magnetic flux density is obtained for input current $i = 1.5$ A and air gap $g = 0.55$ mm as shown in Figure 3.7 for Hiperc-50 and M-19. Similar to the C-core, it can be noticed that the Hiperc-50 has a higher magnetic flux than M-19, which allows it to generate higher magnetic force before saturation. Also, M-19 shows better magnetic flux distribution around the MPL. The magnetic forces of the FEA model and the analytical models (3.14), (3.15) are illustrated in Figure 3.8.

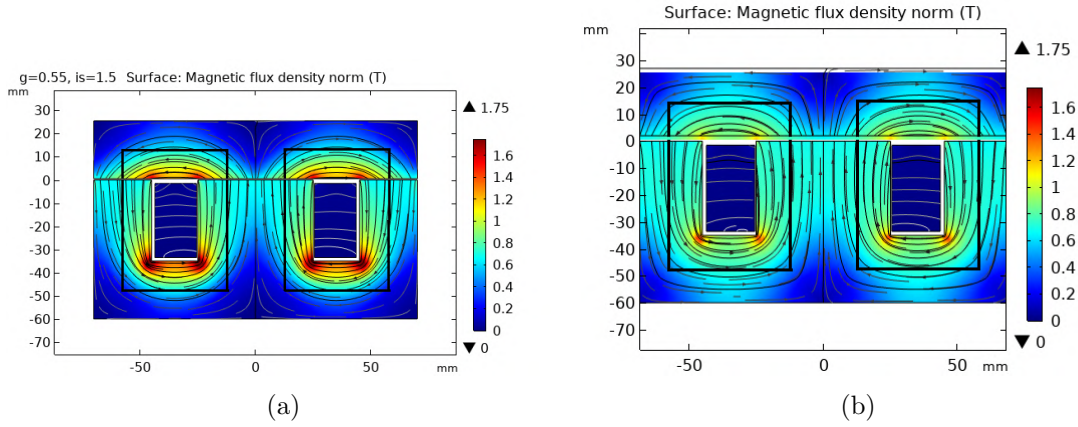


Figure 3.7: The magnetic flux B_E of the E-core RA with input current i of 1.5 A at air gap g of 0.55 mm for ferromagnetic materials (a) Hiperco-50; and (b) M-19.

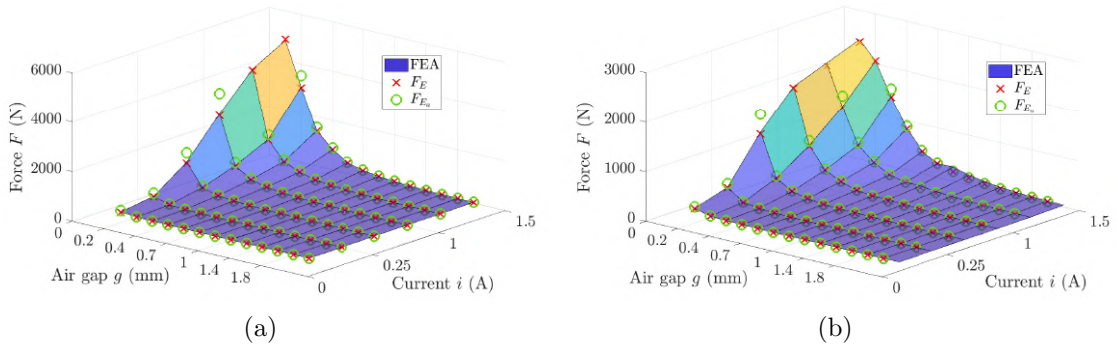


Figure 3.8: The comparison of E-core RA between the magnetic force of FEA, model (3.14), and model (3.15) for (a) Hiperco-50; and (b) M-19.

The percentage errors in the magnetic force are calculated by

$$\varepsilon_E(\%) = \frac{F_{FEA} - F_E}{F_{FEA}} \times 100, \quad (3.18)$$

$$\varepsilon_{E_a}(\%) = \frac{F_{FEA} - F_{E_a}}{F_{FEA}} \times 100. \quad (3.19)$$

where F_{FEA} is the generated force of the FEA model, F_E is the force of the analytical model (3.14), and F_{E_a} is the force of the approximated analytical model (3.15).

Figure 3.9 illustrated the percentage of the errors as function of the air gaps g .

Figure 3.9 shows that the Hiperco-50 ferromagnetic material has a percentage of

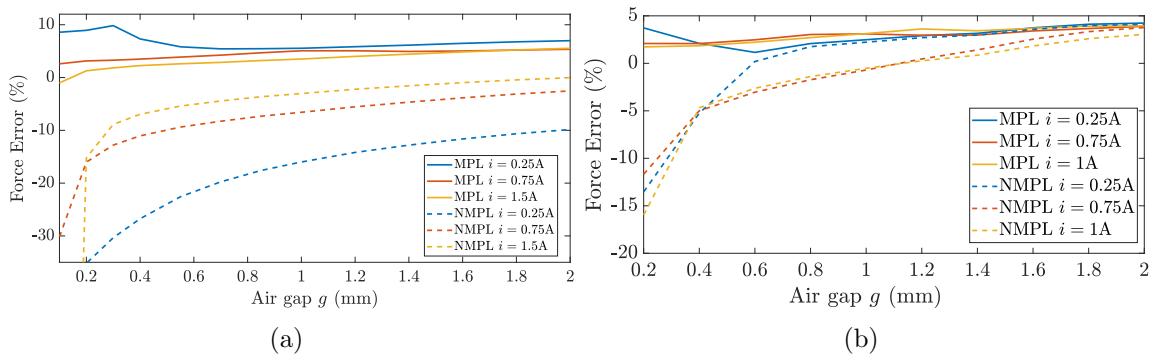


Figure 3.9: The relative force error of E-core RA in (3.18) for (a) Hiperco-50; and (b) M-19.

error of less than 10% when using the analytical model (3.14), whereas M-19 has a percentage of error of less than 5%. Also, it can be noted that the approximated model (3.15) is valid only for M-19 at an air gap range of $g > 1$ mm, where the error is less than 10%. While using Hiperco-50, the approximated model shows a higher percentage of errors.

3.3.2 Simulation Results Discussion

The simulation results show that the analytical models (3.5) and (3.14) can achieve magnetic force similar to the FEA with a percentage of error less than 10% as seen in Fig. 3.6 and 3.9. However, the analytical model requires less computational time to find the solution than the FEA model. The simulation results show that the computation time to find the results with a single input current value and a single value of the air gap is about 0.35 seconds using the analytical model. For the combination of three values of the input current and nine values of the air gaps, the analytical model can achieve all solutions within 5.84 seconds. In contrast, the FEA model requires a computational time of 2 minutes and 43 seconds to obtain all solutions.

For Hiperco-50 ferromagnetic material, using the approximation models (3.6) and (3.15) contributes higher force errors as shown in Figure 3.6 (a) and Figure 3.9 (a).

For M-19 ferromagnetic material, [Figure 3.6 \(b\)](#) and [Figure 3.9 \(b\)](#) shows higher error at relatively low air gaps only. The approximated models depend mainly on the relative permeability corresponding to the calculated magnetic flux. According to [Figure 3.3 \(c\)](#), it can be noted that M-19 has a higher relative permeability as compared to Hiperco-50 for the magnetic flux within the range of $0.125 < B < 1.1875$ (T), thus the M-19 shows less error than using the approximation model. However, materials such as Hiperco-50 is proposed to be used in RA for precision motion systems. This is because it has a higher saturation flux density and less hysteresis. It can be concluded that the approximation models (3.6) and (3.15) can achieve less force error if the input current i at a given air gap g can generate a magnetic flux B with a corresponding relative permeability to satisfy the approximation condition of $\mu_r \gg \frac{l_c}{2g}$ for the C-core RA or $\mu_r \gg \frac{l_{c1}+l_{c2}}{2g}$ for the E-core RA.

3.3.3 Experimental Results

The experimental setup is considered to study the characterization of the RA and verify the simulation results under different input currents and air gaps. The schematic diagram of the used experimental setup is illustrated in [Figure 3.10](#). Two enclosures that house the C-core and E-core are made using a 3D printer. The coils of the two actuators are wounded on the C-core's two lumps and the E-core's center lump using American Wire Gauge (AWG) #22 with a maximum current of 7A. The two RAs are driven using a DC power supply with a maximum volt of 30 V and a maximum current of 5 A. The magnetic force generated in the air gap is measured using four force sensors. The measured signals are collected using a data acquisition card (dSpace-DS1104) and analyzed using MATLAB software.

The magnetic force is obtained for the C-core RA under input currents of $i = \{0.75, 1, 1.25, 1.5, 1.75 \text{ and } 2\}$ A, at air gaps of $g = \{1, 1.35, 1.5, 1.65, \text{ and } 2\}$ mm.

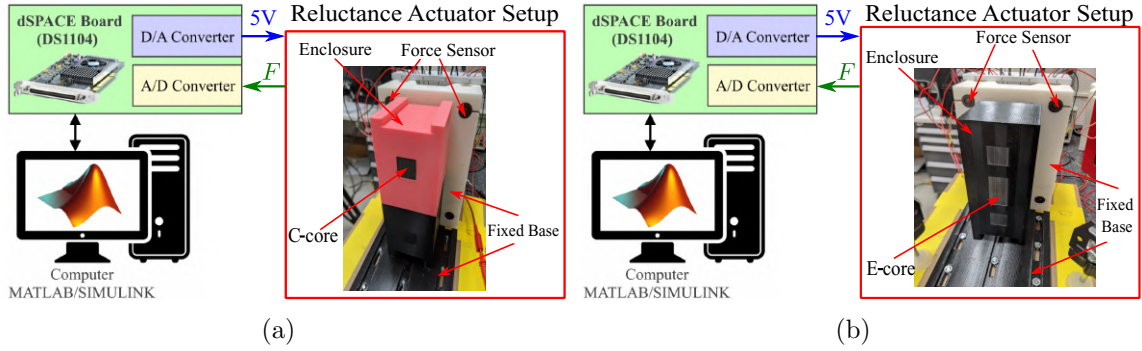


Figure 3.10: Schematic diagram of the experimental setup to measure the magnetic force of the (a) C-core and (b) E-core RA. The measured signals are collected using dSPACE Board DS1104.

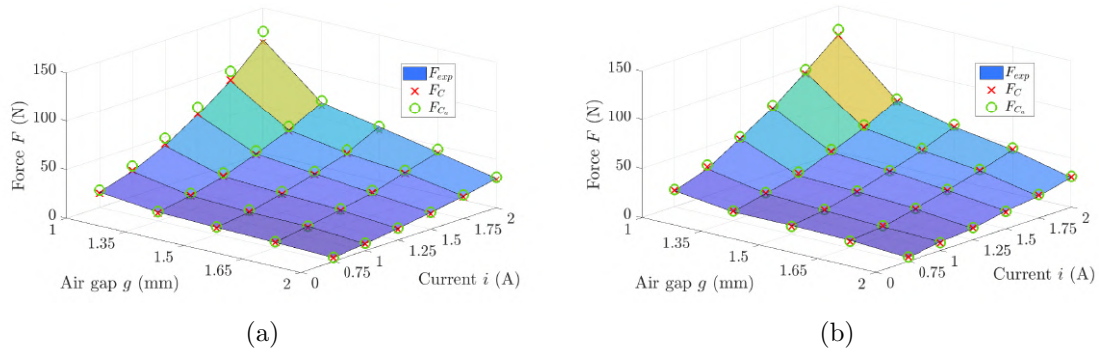


Figure 3.11: The comparison of C-core RA between the experimental measured magnetic force, the magnetic force model (3.5), and model (3.6) for (a) Hiperco-50; and (b) M-19.

Figure 3.11 shows the comparison between the experimental force and the analytical forces using (3.5), and (3.6). Figure 3.12 shows that the relative error between the measured forces and the analytical forces for the Hiperco-50 has higher relative errors over all given air gaps range as compared to M-19. This indicates that the analysis should be conducted using the analytical force (3.14) considering the MPL.

The magnetic force is obtained for the E-core RA under input currents of $i = \{0.75, 1, 1.25, \text{ and } 1.5\}$ A, at air gaps of $g = \{1, 1.35, 1.5, 1.65, \text{ and } 2\}$ mm. Figure 3.13 shows the comparison between the experimental force and the analytical forces using

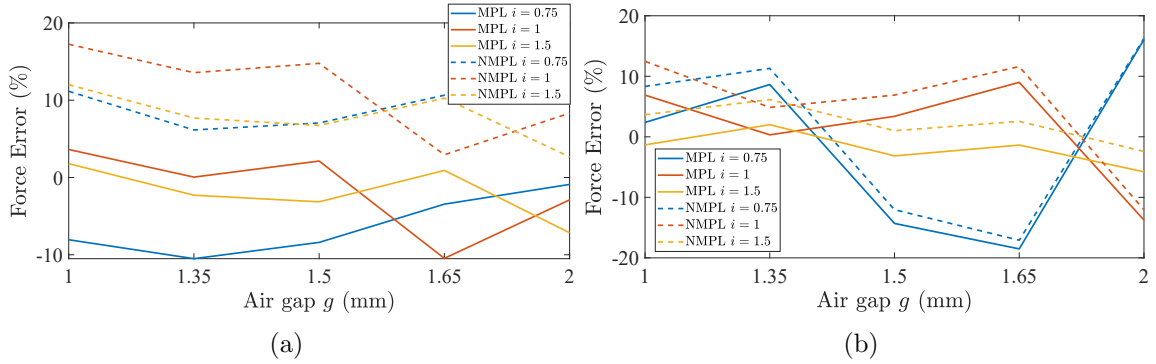


Figure 3.12: The relative force error of C-core RA for (a) Hiperco-50; and (b) M-19.

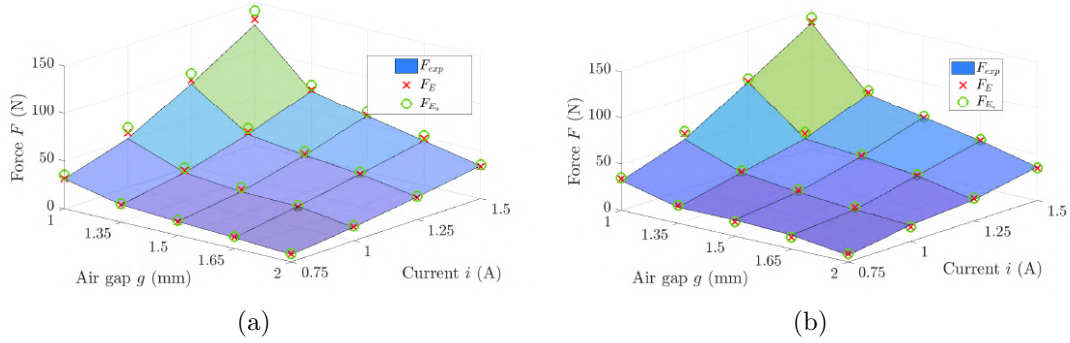


Figure 3.13: The comparison of E-core RA between the experimental measured magnetic force, the magnetic force model (3.5), and model (3.6) for (a) Hiperco-50; and (b) M-19.

(3.14), and (3.15). Similar to the C-core, Hiperco-50 shows higher relative error compared to M-19 as illustrated in Figure 3.14.

The experimental results show the effect of considering the MPL in the analytical formulation of the magnetic force of the RA. Thus, for using the RA for high precision applications where the air gap is less than 2mm, it is necessary to consider the effect of the MPL along with the relative permeability of the ferromagnetic material for more accurate modelling.

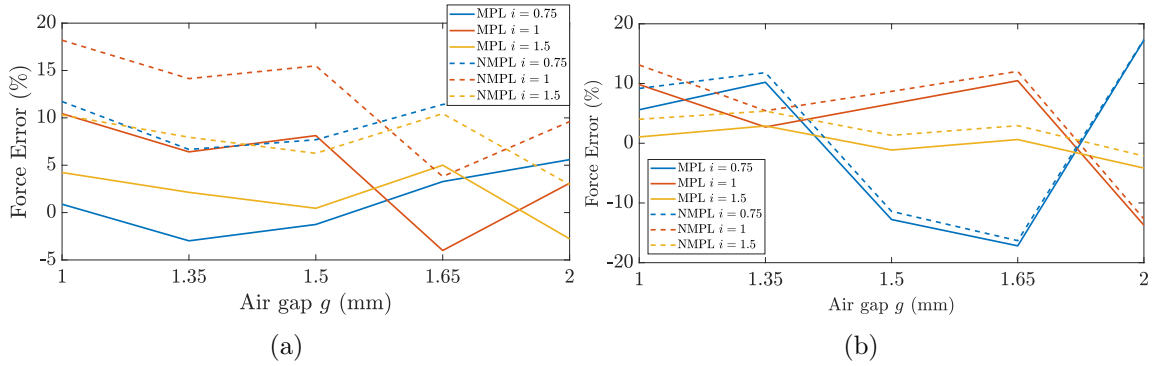


Figure 3.14: The relative force error of E-core RA for (a) Hiperco-50; and (b) M-19.

3.4 Conclusions of the Chapter

This chapter presented the investigation on including and neglecting the mean path length (MPL) of the flux in the analytical modelling of the C-core and E-core RAs. The equivalent magnetic circuit (EMC) is used to formulate the analytical model of the magnetic flux and the magnetic force of a RA; then, the analytical model is approximated by neglecting the effect of the MPL, considering the ferromagnetic material has a large relative permeability.

The analytical and approximated models were compared with the finite element analysis (FEA) model using COMSOL for different air gaps, input currents, and two types of ferromagnetic materials (Hiperco-50 and M-19). The simulation results showed that the error between the magnetic force of FEA model and the approximated model is greater than 15% for small air gaps. However, when the MPL is considered in the analytical model, the error is reduced to less than 5%. Also, it was noticed that the approximated model could be valid for a specific range of air gaps and with higher relative permeability that satisfies the condition of $\mu \gg \frac{l_c}{2g}$ for C-core reluctance and $\mu \gg \frac{l_{c1} + l_{c2}}{2g}$ for E-core RA. Finally, the experimental results were conducted to verify the simulation results. The experimental results showed that the approximated model could be valid for the ferromagnetic material $M - 19$ for air gaps $g > 1$ mm, where the

percentage error is less than 10%. In comparison, the approximated model showed a higher error of more than 10% for the same range of air gaps. The results showed that neglecting the MPL results in a higher relative error in the force, which reduces the system's accuracy. Also, it can be noticed that the relative error in the magnetic force is changed based on the ferromagnetic material selected. Given these results, it is always recommended to include the use of the analytical model that takes into consideration the MPL factor when the range of operation is a few millimetres.

Chapter 4

Modeling and Analysis with Asymmetrical Air Gaps

The following chapter¹ showcases a method for estimating the force of various asymmetrical cases for the C-core RA. To achieve high throughput and efficiency, semiconductor photolithography machines need an actuation system that can meet high acceleration and precision demands on the nanoscale. One available solution is the RA, which provides higher acceleration and force output than the standard, Lorentz actuator. A floating stage with air-bearings is used to eliminate friction in the photolithography process, however, vibration transfer is not entirely eliminated, leading to potential misalignment and asymmetries between the actuator elements. With asymmetrical offsets between mover elements, the output force can be greatly affected. Analytical models are developed and further improved through polynomial curve fitting using precomputed finite element simulation results from Comsol Multiphysics (COMSOL) to achieve more optimal solutions. An experiment verified the results of the force estimation equations, which were within $\sim 11\%$ for different cases

¹A version of this chapter was published in The Review of Scientific Instruments (AIP) [5].

of asymmetric air gaps. This contribution will lead to a design for a control system that will overcome the issue of asymmetries or other altered states.

4.1 Introduction

Photolithography machines are utilized to transfer and encode nanoscale geometric designs into the IC. To reduce vibration transfer, a floating stage with air-bearings is used which eliminates friction [110]. These air-bearings allow the motion platform to hover, allowing no contact and therefore, no friction or wear on nanoscale motions [111]. Vibration transfer is not entirely eliminated, however, since air vortices are generated within the air-bearing, inducing small vibrations into the positioning stage [112], leading to self-excited instabilities that could damage the whole positioning stage [113]. This would lead to overall positioning inaccuracies, reducing the accuracy of the positioning stage [114]. Especially with RAs, the misalignment would impart asymmetries leading to significant differences in force output profiles depending on the asymmetry case. For this reason, it is important to investigate how the force can be estimated for various altered states.

This chapter examines asymmetrical cases of the RA from angular disturbances as outlined in Fig. 4.1. There is an example of Case 1 being examined in [2] with the use of a block diagram for disturbance simulation is briefly outlined. In [115] an experimental testbed is presented which can impart Case 1 disturbances with the use of piezoelectric actuators to test out algorithms for disturbance control. There has not been an in-depth analysis on a RA with disturbance cases in all rotational degrees of freedom as in Fig. 4.1.

This chapter outlines how angular disturbance cases in each degree of freedom of a C-core RA affect the output force. The analytical solutions are further optimized by

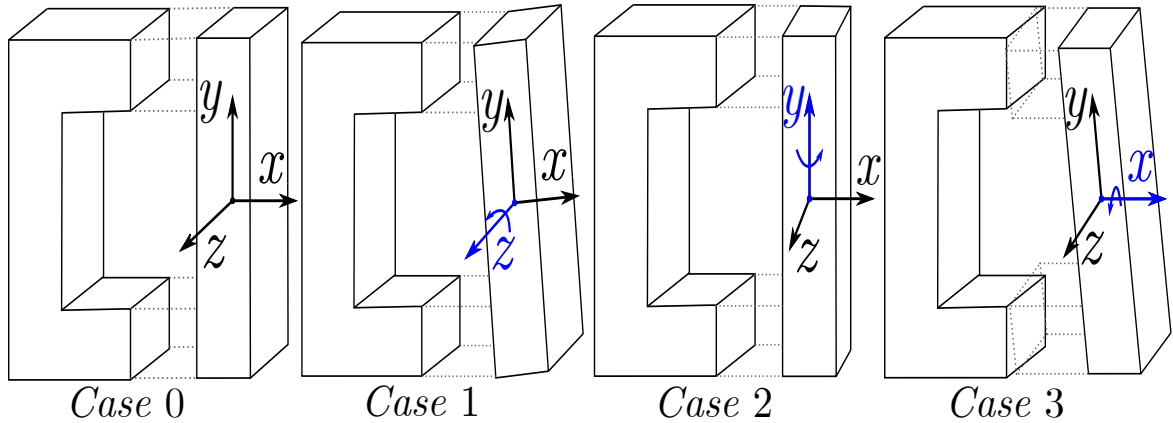


Figure 4.1: Case 0 is the ideal case with symmetrical air gaps. Whereas Case 1, 2, and 3, have angular disturbances in the z , y , and x axis respectively.

comparing them to COMSOL FEA models to generate polynomial correction factors for each case. Also, a filleted C-core is modeled using polynomial correction factors. Each case is compared to experimental findings. The chapter is outlined as follows: an analytical model derivation for each disturbance case is presented in Section 4.2. The COMSOL FEA models are built and compared to the analytical model in Section 4.3 and a polynomial correction function is found. In Section 4.4, the experimental apparatus is outlined, and results are shown along with comparisons to the analytical results with a discussion presented in Section 4.5. Finally, Section 4.6 presents the conclusions of this study and the future work.

4.2 Analytical Model

The ideal symmetrical case is defined as Case 0, whereas Case 1, 2, and 3 have angular disturbances about the z , y , and x axis respectively. There are forces along the I-beam pushing it towards the C-Core element from Fig. 4.2. For Case 1, asymmetries result in different forces in the top and bottom, inducing torque onto the I-beam. There would also be flux fringing and hysteresis effects as shown in [116], but it is

not evaluated in this thesis. The reluctance for a non-parallel gap is found through integration of the gap along the edge. The analytical model provides a rough estimate of what the force will be and will not be accurate in some cases, so FEA modelling is used to further the force estimation through the use of polynomial correction factor functions to match the FEA data found. The variables that will be monitored in the model will be the angular offset, θ , the air gap displacement, a , the electrical input current, i , and the output force, F .

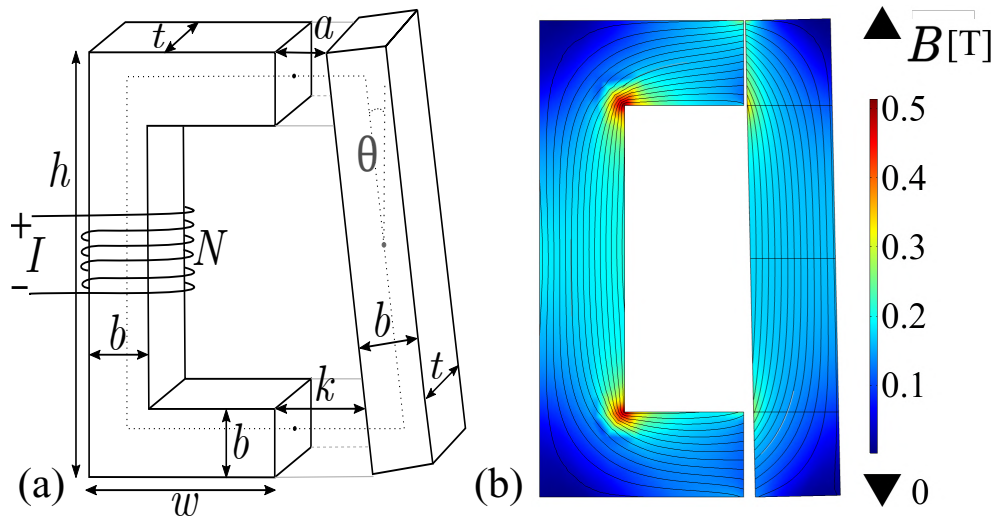


Figure 4.2: Case 1, (a) Schematic representation of the C-Core RA and (b) COMSOL flux density distribution FEA of C-Core.

4.2.1 Case 0 Derivation

This case is for the standard symmetrical air gap scenario and can be found in the literature, see for example [2, 108, 116–121]. However, most of these references do not take into full account the mean path length, l_m , of the magnetic material. With the assumption that no fringing occurs, the flux density, B , can be found along with the mean path length, l_m :

$$l_m = 2(h + w - b), \quad B = \frac{\mu_0 N i}{\frac{l_m}{\mu_r} + 2a}, \quad (4.1)$$

where μ_0 is the permeability of free space, μ_r is the relative permeability of the C-core and I-beam material, N is the number of coil turns, i is the coil current, l_m is the mean path length, and a is the air gap displacement.

Gauss's Law states that the flux entering and leaving a surface is equivalent [122] :

$$B * dS = 0. \quad (4.2)$$

The Maxwell stress tensor can reduce to [2] as

$$F = \frac{1}{2\mu_0} \int_S B^2 dS = \frac{A}{2\mu_0} B^2 = \frac{\mu_0 A N^2 i^2}{2(\frac{l_m}{\mu_r} + 2a)^2}, \quad (4.3)$$

where F is the force in each air gap (F_1 is the force in the upper air gap, F_2 is the force in the lower air gap. For this case $F = F_1 = F_2$), and A is the cross-sectional area.

4.2.2 Case 1 Derivation

In Case 1, the I-beam is subjected to a rotation in the z -axis resulting in asymmetric tilted air gaps as shown in Fig. 4.3. We obtain

$$g(y) = a + (b - y) \tan(\theta). \quad (4.4)$$

Then

$$dP_1(y) = \frac{-\mu_0 t dy}{\frac{c}{b} y - (a + c)} \quad (4.5)$$

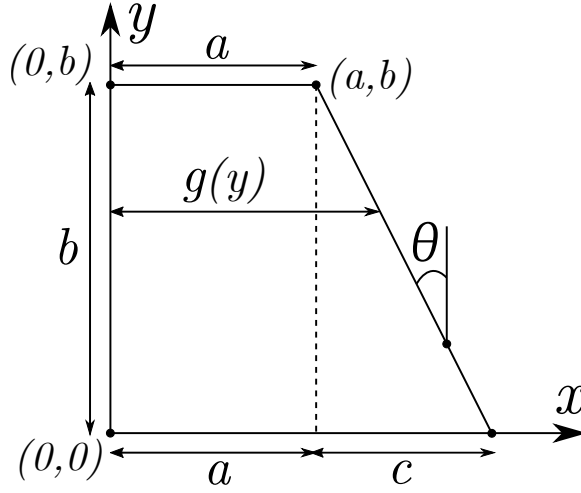


Figure 4.3: Geometric representation of tilted air gap for the Case 1 reluctance derivation, with a rotation in the z -axis of the I-beam.

and we can write

$$P_1 = \int_0^b \frac{-\mu_0 t}{\frac{c}{b}y - (a+c)} dy = \frac{\mu_0 A}{b \tan \theta} \ln \left(\frac{b \tan \theta}{a} + 1 \right) \quad (4.6)$$

and

$$R_1 = \frac{1}{P_1} = \frac{b \tan \theta}{\mu_0 A \ln \left(\frac{b \tan \theta}{a} + 1 \right)}, \quad (4.7)$$

where P_1 is the permeance of the top air gap, which is the reciprocal of the reluctance, R_1 . The reluctance in the second gap, R_2 , can be found by substituting a for $k = a + (h - b) \tan \theta$ as

$$R_2 = \frac{b \tan \theta}{\mu_0 A \ln \left(\frac{b \tan \theta}{k} + 1 \right)} \quad (4.8)$$

The reluctance in the C-Core, R_C , and the I-Beam, R_I , is found from the geometry as

$$R_C = \frac{h + 2(w - b)}{\mu_r \mu_0 A}, \quad R_I = \frac{h}{\mu_r \mu_0 A \cos \theta}. \quad (4.9)$$

Then the total reluctance of the system is then found to be the summation of all the reluctances since they are in series as

$$R_T = R_1 + R_2 + R_C + R_I. \quad (4.10)$$

Then based on (4.3), the force, F , through a section of area, A , in terms of the

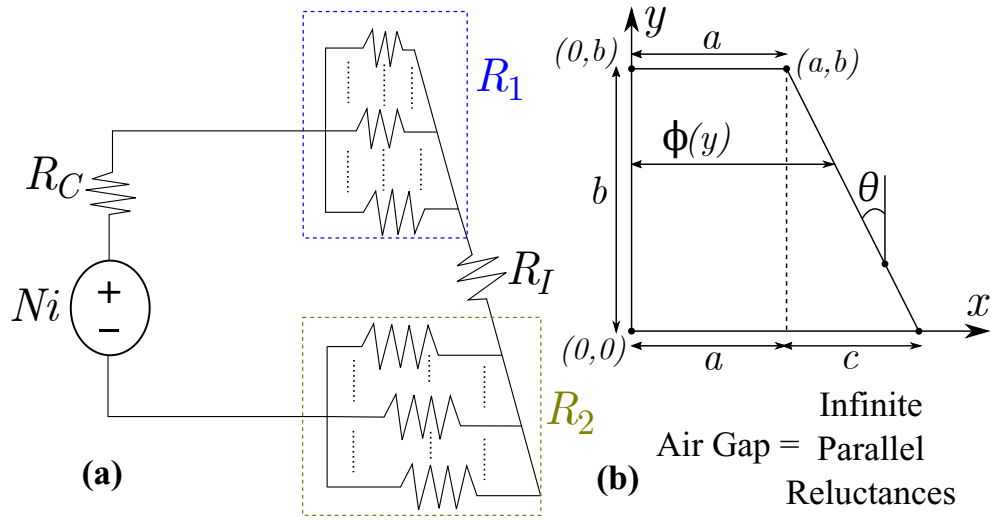


Figure 4.4: The RA is modelled as a magnetic circuit (a), with the air gaps being represented (b) as a set of infinite reluctances in parallel.

magnetic flux, $\phi = BA$, can be defined as:

$$F = \frac{\phi^2}{2\mu_0 A} \quad (4.11)$$

The flux through the air gaps is modelled as a set of infinite parallel paths. Therefore, the flux can be defined as

$$d\phi_1(y) = \frac{Ni}{R_T} R_1 dP_1(y) = \frac{-NiR_1\mu_0 t dy}{R_T(\frac{c}{b}y - (a + c))} \quad (4.12)$$

Combining (4.11) and (4.12) yields

$$dF_1(y) = \frac{d\phi_1^2}{2\mu_0 t dy} = \frac{N^2 i^2 R_1^2 \mu_0 t dy}{2R_T^2 \left(\frac{c}{b}y - (a+c)\right)^2} \quad (4.13)$$

and

$$F_1 = \int_0^b \frac{N^2 i^2 R_1^2 \mu_0 t}{2R_T^2 \left(\frac{c}{b}y - (a+c)\right)^2} dy = \frac{N^2 i^2 R_1^2 \mu_0 A}{2R_T^2 a (b \tan \theta + a)}, \quad (4.14)$$

where F_1 is the force in the top air gap. The force in the bottom air gap, F_2 , is found similarly by replacing a with k and R_1 with R_2 .

$$F_2 = \frac{N^2 i^2 R_2^2 \mu_0 A}{2R_T^2 k (b \tan \theta + k)}. \quad (4.15)$$

4.2.3 Case 2 Derivation

In Case 2 the rotation of the I-beam about the y -axis provides equal tilted air gaps in the upper and lower gap sections as shown in Fig. 4.5. The geometric representation

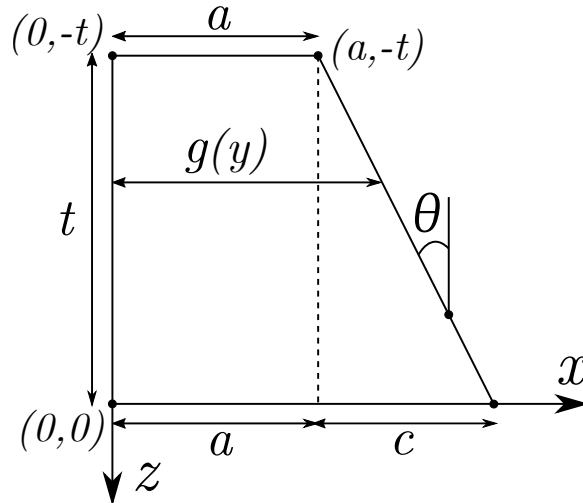


Figure 4.5: Geometric representation of tilted air gap for the Case 2 reluctance derivation, with a rotation in the y -axis of the I-beam.

for Case 2 follows the same layout as Case 1 assuming $t = b$. The upper and lower gaps are the same for Case 2, therefore the reluctance in both air gaps is the same, resulting in the same force produced. Using a similar derivation from Case 1, the upper and lower reluctance can be found:

$$R_1 = R_2 = \frac{b \tan \theta}{\mu_0 A \ln \left(\frac{b \tan \theta}{a} + 1 \right)} \quad (4.16)$$

Leading to the forces:

$$F_1 = F_2 = \frac{N^2 i^2 R_1^2 \mu_0 A}{2R_T^2 a (b \tan \theta + a)} \quad (4.17)$$

4.2.4 Case 3 Derivation

Case 3 is similar to Case 0, where the air gaps are symmetrical. However, the projected area that the magnetic flux flows through is changed with the rotation in the x -axis as shown in Fig. 4.6.

For Case 3, the projected gap area, A_G needs to be determined. This can be done as shown in Fig. 4.6, through the subtraction of A_s and A_T from the original as

$$A_G = b^2 - A_s - A_T. \quad (4.18)$$

The geometric parameters can then be found through trigonometry as

$$\chi = \frac{1}{2}(h - b \sin \theta) \tan \theta, \quad (4.19)$$

$$\varepsilon = \frac{1}{2}(h - b(2 + \sin \theta)) \tan \theta, \quad (4.20)$$

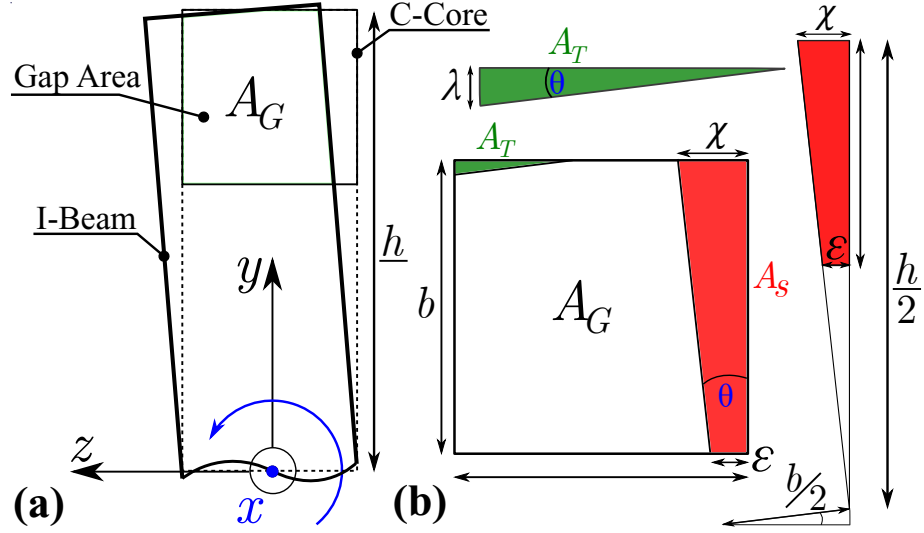


Figure 4.6: Geometric representation (a) of tilted cross-section for the Case 3 reluctance derivation, with a rotation in the x -axis of the I-beam. The air gap cross-section (b) is shown to not be square due to the tilted I-beam.

$$\lambda = \frac{h}{2}(1 - \sec \theta) - \frac{b}{2} \tan \theta, \quad (4.21)$$

$$A_T = \frac{\lambda^2}{2 \tan \theta}, \quad A_s = \frac{\chi^2 - \varepsilon^2}{2 \tan \theta}. \quad (4.22)$$

The gap area can then be found through (16) as

$$A_G = b^2 - \frac{\chi^2 - \varepsilon^2 - \lambda^2}{2 \tan \theta}. \quad (4.23)$$

Since the rotation is in the middle of the I-beam, the gap area will be equal due to symmetries. This leads to the force equation like in Case 0, just the area, A , is replaced by the gap area, A_G as

$$F_1 = F_2 = \frac{N^2 i^2 \mu_0 A_G}{8 \left(\frac{h+w-b}{\mu_r} + a \right)^2}. \quad (4.24)$$

This equation estimates the force more accurately for smaller air gaps. With a bigger

air gap, the flux will have room to travel, and the gap area, A_G , would be more similar to the standard area, A , from Case 0. However, the polynomial correction factor found in Section 4.3 fixes this issue for all cases and allows the force to match for all air gaps and angles.

4.3 Simulation Results

In order to verify the analytical model, the RA was built and verified using COMSOL, which is a finite element analysis (FEA) multiphysics modelling software engine. A similar approach was conducted in [116] and [123], by using FEA to find physics relationships for complex systems to obtain approximate governing equations. The RA to be examined features dimensions of $b = t = 25\text{mm}$, $w = 60\text{mm}$, $h = 140\text{mm}$, and $N = 400$ turns for all simulation and experimental models as based on the previous schematic in Fig. 4.2a.

The model material consists of Hiperco 50, annealed at 1411°F , which is an iron-cobalt vanadium alloy. The magnetic field density versus the magnetic field intensity curve or commonly known as the BH-curve was utilized as shown in Fig. 4.7. The analytical model can then be corrected considering this saturation using a lookup table of the given BH-curve of the material used when solving the derived equations.

4.3.1 Case 0

First, Case 0 is built and tested as shown in Fig. 4.8. Using the analytical solution from (4.3), the forces are found and compared to the COMSOL model with the current set to $i = 1\text{A}$ and the number of turns set to $N = 400$ for a gap range of $a = 0.25\text{mm}$ to 2mm . The results match very closely with a maximum error of 1.26% between models as shown in Fig. 4.9.

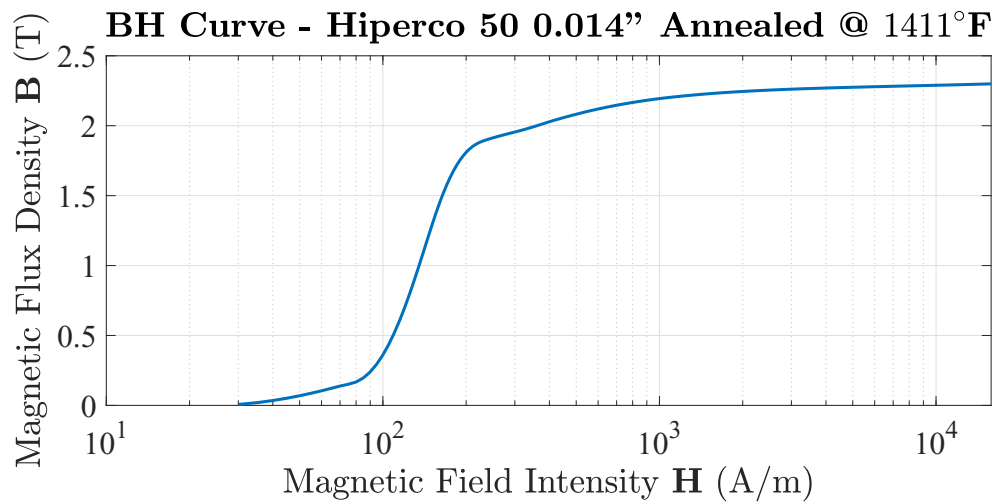


Figure 4.7: BH Curve for the Hiperco 50 0.014" annealed at 1411°F in which the I-beam and C-core are comprised of. This curve is used in the simulation and analytical models.

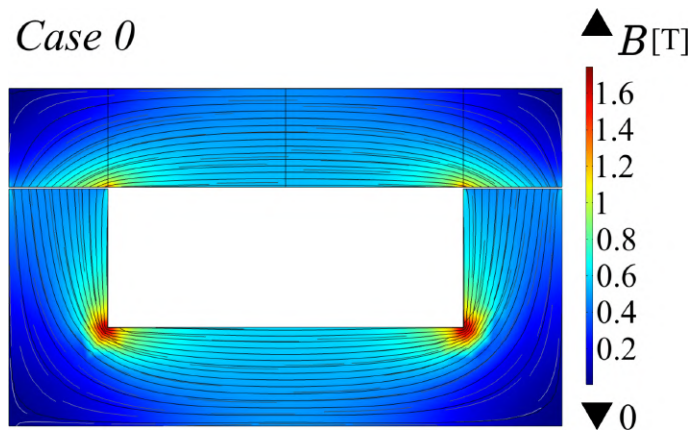


Figure 4.8: COMSOL model of the Case 0 RA, for an air gap separation of 0.5mm.

These results show good matching between COMSOL and the analytically derived solution. Next, the other cases will be evaluated with COMSOL to determine the simulated force responses.

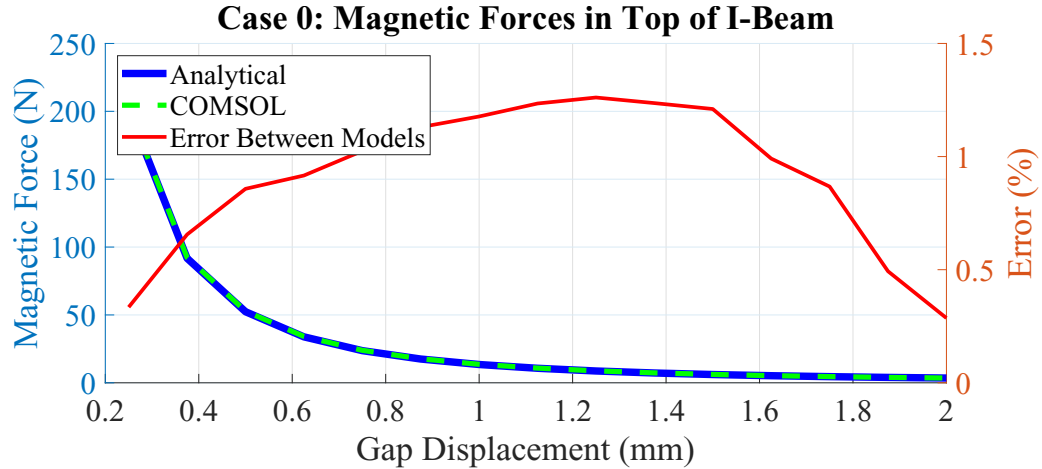


Figure 4.9: The analytical and COMSOL models for Case 0, are shown to match with a maximum error of 1.26% between forces in the top air gap, with a direct current of 1A and 0.25 – 2mm of gap separation.

4.3.2 Case 1

The next case is modelled in COMSOL and compared with the analytical model based on (4.14) and (4.15). When running the simulation, the area that the flux passes through is different from the original assumption since there is an angle, the flux is more concentrated near the area where the I-beam and C-core are close as shown in Fig. 4.10 and does not flow in a linear fashion. Due to the physical complexity of the asymmetry, the model needs to be corrected using a 3D surface map correction factor based on the angle and gap separation to provide better matching. The 3D correction map does not consider any approximations or assumptions and a polynomial equation for the effective area can be derived from the correction map with curve fitting tools to better match the ideal flux path.

The 3D surface of the COMSOL force versus z -angle and gap separation was generated and was compared to the analytical solution through a ratio and fitted to a 3D polynomial curve using Matlab as shown in Fig. 4.11. The correction factors to the top and bottom areas were then determined in order to 3D curve fit the data, to

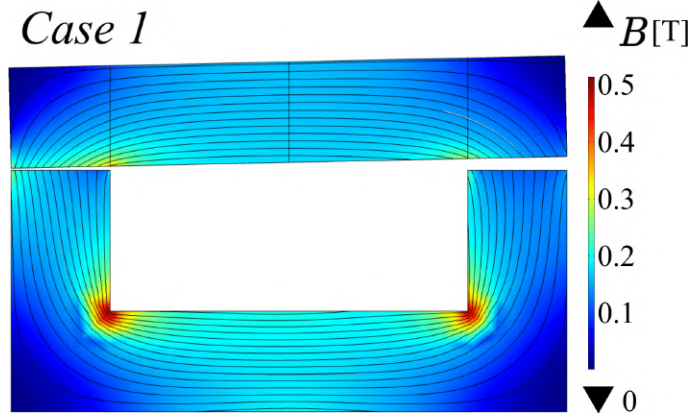


Figure 4.10: COMSOL model for Case 1 RA, for an air gap separation of 0.5mm and an angle of 1.2° in the z -axis.

the data from COMSOL. The new equation works well with various current also as shown in Fig. 4.12. The correction factors replace the original areas, A_1^* and A_2^* for the top and bottom air gap respectively, in each equation as follows:

$$A_1^* = (0.9993 + 0.7067\theta - 0.01683a - 0.01796\theta^2 - 0.7009\theta a + 0.08285a^2 - 0.03938\theta^3 + 0.1231\theta^2 a + 0.339\theta a^2 - 0.06827a^3 + 0.01575\theta^3 a - 0.04931\theta^2 a^2 - 0.05538\theta a^3 + 0.01582a^4)A$$

$$A_2^* = (0.9891 - 0.1223\theta + 0.02504a + 0.1897\theta^2 - 0.2571\theta a + 0.02204a^2 - 0.09227\theta^3 + 0.02859\theta^2 a + 0.1626\theta a^2 - 0.03298a^3 + 0.03301\theta^3 a - 0.03544\theta^2 a^2 - 0.02464\theta a^3 + 0.008659a^4)A$$

4.3.3 Case 2

For Case 2, the COMSOL model was built in 3D as shown in Fig.4.13, then tested and compared to analytical results through various y -angles to determine the polynomial correction factors following the same procedures as from Case 1. For this case, the forces in the top and bottom were found to be approximately the same since it behaves symmetrically. The correction factor would replace the area, A , in the equation by

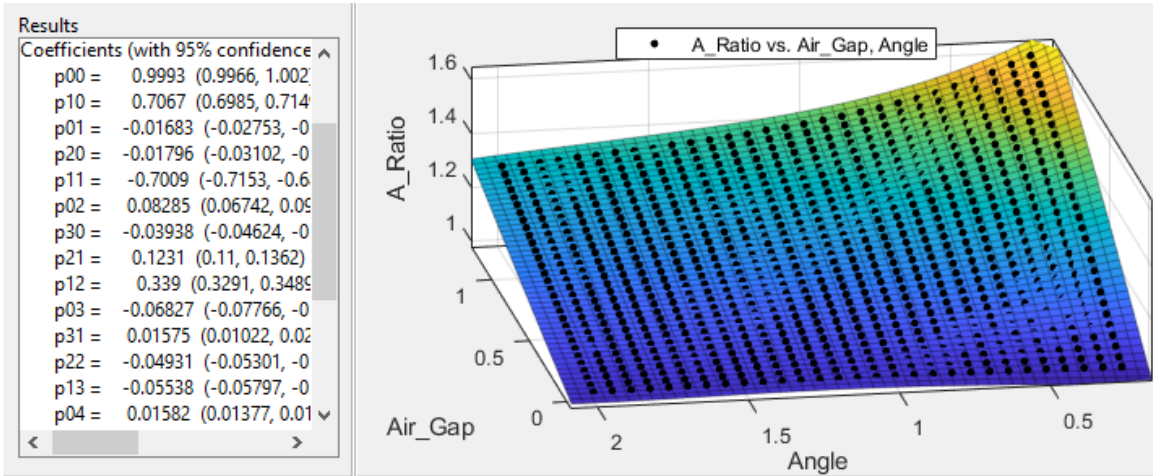


Figure 4.11: Comparing the COMSOL results with the analytically derived equation for the top force and fitting the ratio to a 3D surface with the use of Matlab’s Curve Fitting Toolbox, the correction factor equation for the new area can then be derived. The same is produced for the bottom force equation.

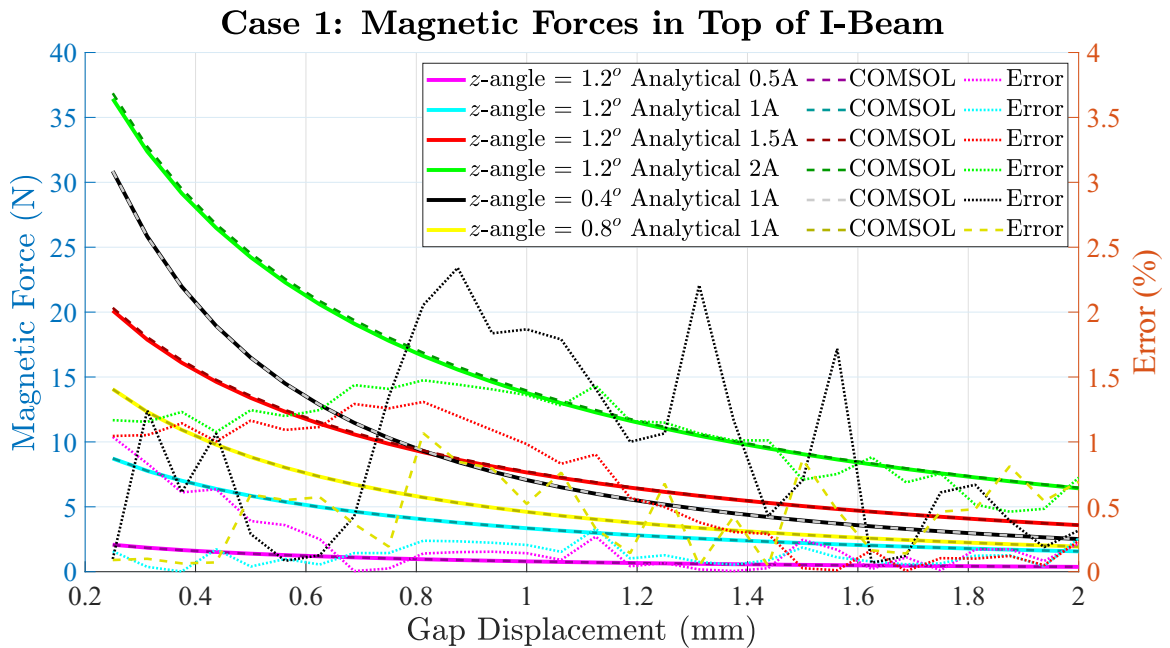


Figure 4.12: The COMSOL and analytical model of the top gap force of Case 1 are compared for various current ranging from 0.5 - 2A and z -angle disturbances. This confirms that the equations work for various current input with the biggest error being 2.3%.

A^* :

$$A^* = (0.9837 + 0.006107\theta + 0.07228a - 0.006254\theta^2 + 0.008648 - 0.03465a^2 + 0.0005082\theta^2a - 0.003761^2 + 0.005482a^3)A \quad (4.26)$$

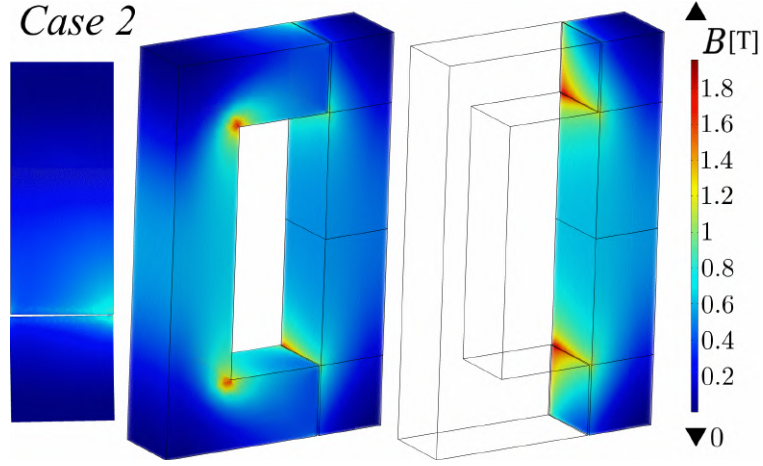


Figure 4.13: COMSOL model for Case 2, with a gap separation of 0.25mm and an angle of 1.2° in the y -axis.

4.3.4 Case 3

For Case 3, the COMSOL model was built in 3D and tested as shown in Fig.4.14, then compared to analytical results through various x -angles in order to find the polynomial correction factors on the area. Similar to Case 2, the forces in the top and bottom air gaps were found to be the same as also found in the original analytical derivation. The polynomial correction can then be applied by replacing area, A_G , with

A_G^* :

$$A_G^* = (0.9812 + 0.02393\theta + 0.07114a - 0.01678\theta^2 + 0.01281\theta a - 0.02272a^2) * A_G \quad (4.27)$$

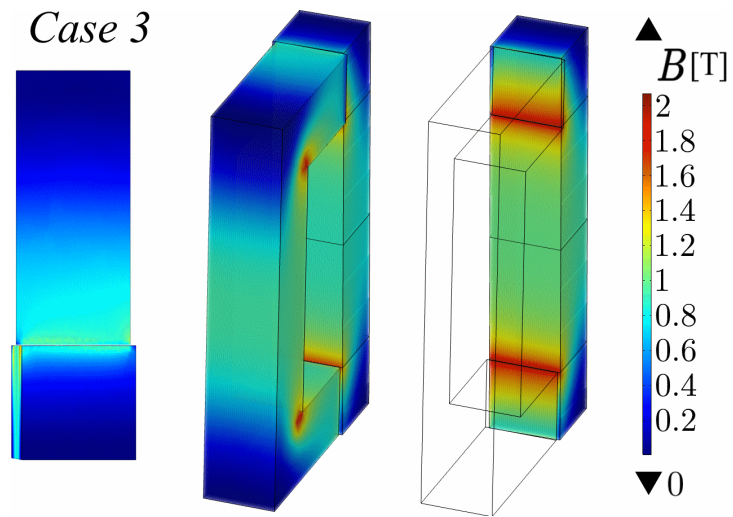


Figure 4.14: COMSOL model for Case 3, with a gap separation of 0.25mm and an angle of 1.2° in the x -axis.

4.3.5 Case 0F

For Case 0F, fillets are introduced to observe whether fillets can help improve the actuator performance. The case is the same as Case 0, however, 5mm fillets are introduced at the edges of the C-Core as shown in Fig.4.15.

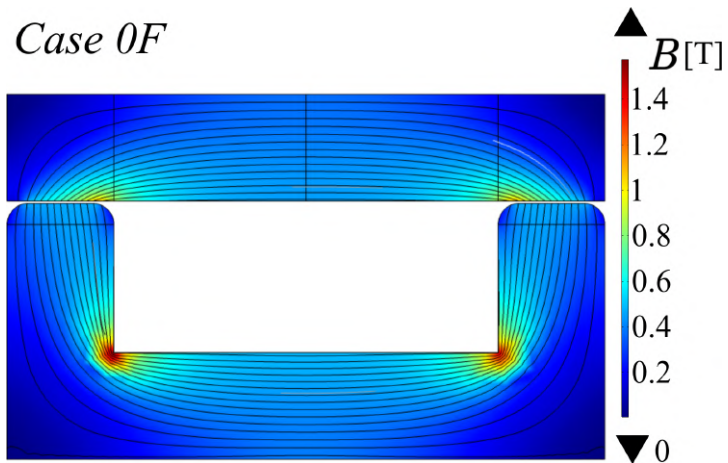


Figure 4.15: COMSOL model of the Case 0F RA, which features 5mm fillets, for an air gap separation of 0.5mm.

The COMSOL results are then compared to Case 0 results and a polynomial correction factor, \mathbf{A}_f^* , to replace the area, A , is found:

$$\mathbf{A}_f^* = (0.00716a^3 + -0.0586a^2 + 0.175a + 0.675)A \quad (4.28)$$

The analytical cases can then be compared to Case 0 to determine their effect as shown in Fig. 4.16.

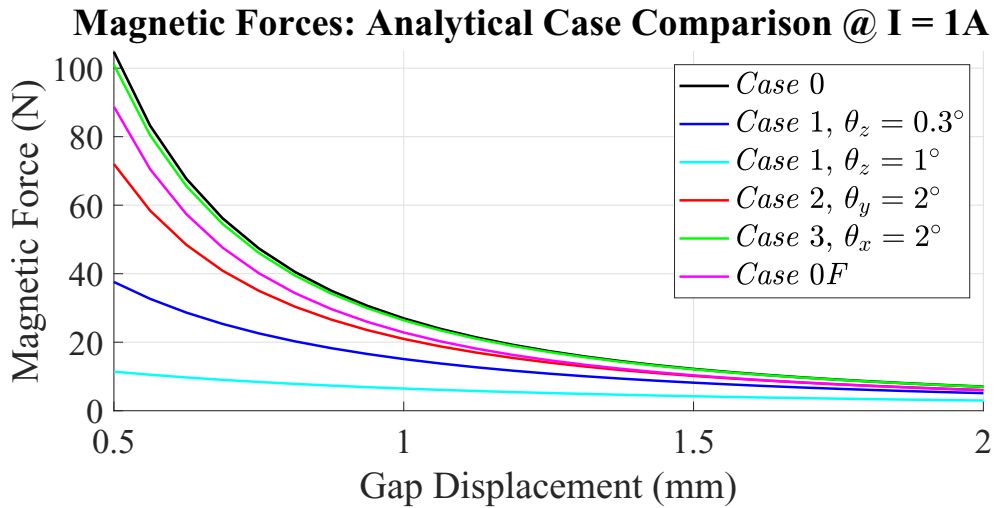


Figure 4.16: Total analytical I-beam output force comparison of all considered cases at a current of $I = 1A$ and a 0.5 – 2mm of gap separation.

4.3.6 Case 1+2

Since Case 2 has been modelled to Case 0 and since Case 1 is based off Case 0, the effective air gap, \bar{a} , and the influence on the reluctance can be introduced into Case 1 to form Case 1+2 as shown in Fig. 4.17.

The new equation would combine the polynomial correction functions on the effective area of Case 1 and Case 2 to get the new effective area, A_1^* , for the top air

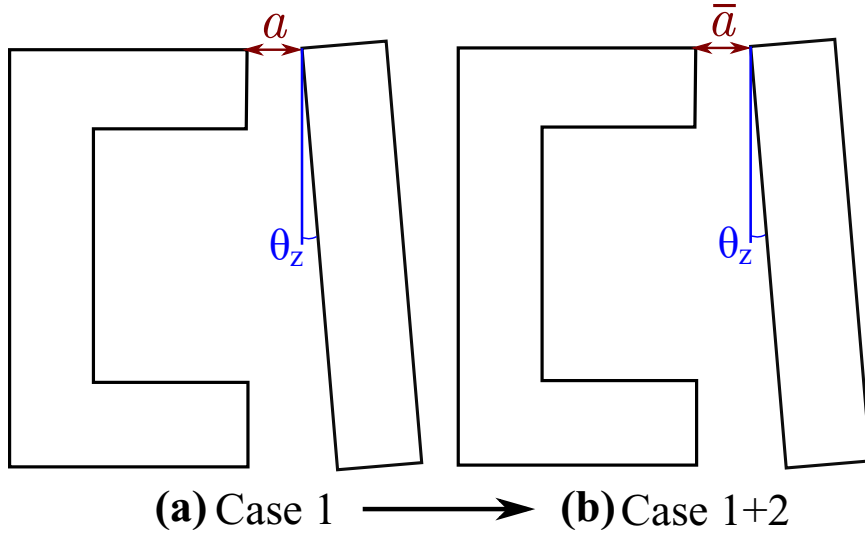


Figure 4.17: (a) Case 1 can be converted to the combination of Case 1+2 with the introduction of the effective air gap, \bar{a} , along with the derived polynomial correction factors and influence on the reluctance.

gap and, A_2^* , for the bottom air gap. The effective air gap, \bar{a} , is used and the effect of the air gap on the reluctance equation, a_R , is used in the reluctance equation. This forms the general equation for Case 1+2:

$$F_1 = \frac{N^2 i^2 R_1^2 \mu_0 A_1^*}{2R_T^2 \bar{a} (b \tan \theta_z + \bar{a})}. \quad (4.29)$$

$$F_2 = \frac{N^2 i^2 R_2^2 \mu_0 A_2^*}{2R_T^2 \bar{k} (b \tan \theta_z + \bar{k})}. \quad (4.30)$$

$$R_1 = \frac{b \tan \theta_z}{\mu_0 A \ln \left(\frac{b \tan \theta_z}{a_R} + 1 \right)} \quad (4.31)$$

$$R_2 = \frac{b \tan \theta_z}{\mu_0 A \ln \left(\frac{b \tan \theta_z}{k_R} + 1 \right)} \quad (4.32)$$

Where $\bar{k} = \bar{a} + (h - b) \tan \theta_z$ and $k_R = a_R + (h - b) \tan \theta_z$. θ_z is the angular offset

in the z -axis.

4.3.7 Case 1+2+3

Finally, all three augmented cases can be combined. The effect Case 3 has is to augment the overall air gap by A^G as outlined in Fig. 4.6. This would lead to the final augmented area, A_1^* , for the top air gap and, A_2^* for the bottom air gap, is the product of the polynomial correction functions for each rotational degree of freedom multiplied by A_G :

$$\begin{aligned} \mathbf{A}_1^*(\theta_x, \theta_y, \theta_z, a) = & (0.9993+0.7067\theta_z-0.01683a-0.01796\theta_z^2-0.7009\theta_z a+0.08285a^2- \\ & 0.03938\theta_z^3+0.1231\theta_z^2 a+0.339\theta_z a^2-0.06827a^3+0.01575\theta_z^3 a-0.04931\theta_z^2 a^2-0.05538\theta_z a^3+ \\ & 0.01582a^4)(0.9837+0.006107\theta_y+0.07228a-0.006254\theta_y^2+0.008648\theta_y a-0.03465a^2+ \\ & 0.0005082\theta_y^2 a-0.003761\theta_y a^2+0.005482a^3)(0.9812+0.02393\theta_x+0.07114a-0.01678\theta_x^2+ \\ & 0.01281\theta_x a-0.02272a^2)A_G \end{aligned}$$

$$\begin{aligned} \mathbf{A}_2^*(\theta_x, \theta_y, \theta_z, a) = & (0.9891-0.1223\theta_z+0.02504a+0.1897\theta_z^2-0.2571\theta_z a+0.02204a^2- \\ & 0.09227\theta_z^3+0.02859\theta_z^2 a+0.1626\theta_z a^2-0.03298a^3+0.03301\theta_z^3 a-0.03544\theta_z^2 a^2-0.02464\theta_z a^3+ \\ & 0.008659a^4)(0.9837+0.006107\theta_y+0.07228a-0.006254\theta_y^2+0.008648\theta_y a-0.03465a^2+ \\ & 0.0005082\theta_y^2 a-0.003761\theta_y a^2+0.005482a^3)(0.9812+0.02393\theta_x+0.07114a-0.01678\theta_x^2+ \\ & 0.01281\theta_x a-0.02272a^2)A_G \end{aligned} \tag{4.33}$$

Leading to the final force equations for Case 1+2+3:

$$F_1 = \frac{N^2 i^2 R_1^2 \mu_0 A_1^*}{2R_T^2 \bar{a}(b \tan \theta_z + \bar{a})}. \tag{4.34}$$

$$F_2 = \frac{N^2 i^2 R_2^2 \mu_0 A_2^*}{2R_T^2 \bar{k} (b \tan \theta_z + \bar{k})}. \quad (4.35)$$

$$F_T = F_1 + F_2 \quad (4.36)$$

Where F_T is the combined force of the top and bottom air gaps. Now this solution can be compared with COMSOL results in the following section for verification.

The model was then tested with the multi-axial cases between the stator and mover as seen in Table 4.1. An example of the COMSOL simulation is shown in Fig. 4.18 of Setup #3.

Table 4.1: Setup trials to simulate and compare with the analytic solution for verification.

heightSetup #	θ_x (mrad)	θ_y (mrad)	θ_z (mrad)
1	5	5	5
2	10	10	2
3	25	20	5
4	0	25	2
5	15	0	5

4.4 Experimental Design

In order to analyze the forces in the I-beam at various air gaps, two enclosures and a force bracket were built in SolidWorks and 3D printed. These enclosures will isolate and house the I-beam and the C-Core separately, allowing static measurements of the force induced at various gaps. These enclosures are shown in Fig. 4.19. The I-beam and C-Core were built using layered laminations of annealed Hiperc 50 iron-cobalt vanadium alloy.

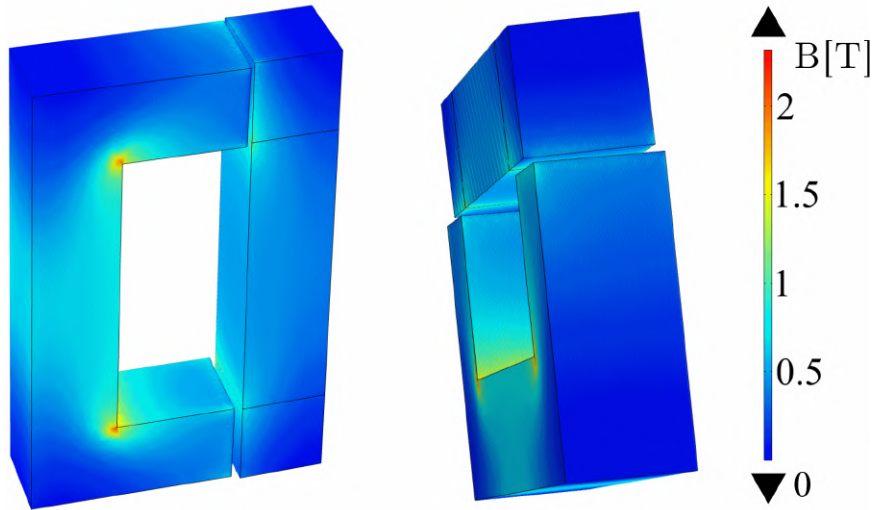


Figure 4.18: COMSOL model for Setup #3 which features $\theta_x = 25\text{mrad}$, $\theta_y = 20\text{mrad}$, and $\theta_z = 5\text{mrad}$.

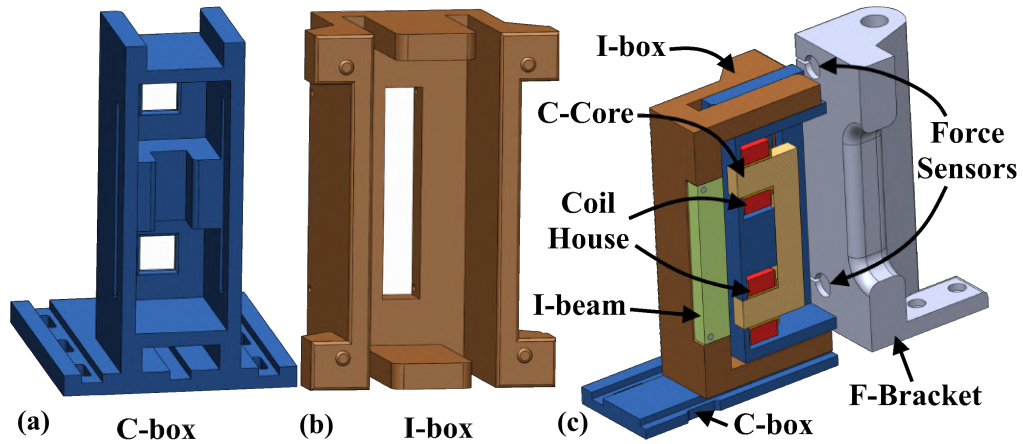


Figure 4.19: The (a) C-box and (b) I-box house the C-core and I-beam respectively. The F-bracket (c) houses the force sensors and is what the I-box pushes against. Solidworks cross-sectional model (c) of the experimental assembly is also shown. All housing components are 3D printed.

The I-beam is seated inside of the rectangular slot of the I-box and fixed with two aluminum pins that goes through both the I-beam and the I-box. The pin goes through a region with minuscule flux contribution, therefore not greatly affecting any of the calculations. From the analysis, at a 0.25mm gap, the force in the top and

bottom gap without the holes were found to be 201.57 and 201.49N respectively. Whereas, with the holes the forces were 201.54 and 201.44N respectively. Therefore, it was found that the holes do not affect the force in any substantial way.

There are two coils in this design that are seated on the two teeth of the C-core. Each coil has a 3D printed Coil House in which the coil wire wraps around. Each Coil features 200 turns, giving an $N = 400$. These Coil Houses are then slotted onto the C-core which is then seated into the C-box. The force bracket or, F-bracket, is designed to be mounted behind the C-box. The force from the I-box is pressed up against and measured through four compression sensors (FX293X-100A-0010-L) [124] that are connected to the vertical divots as seen in Fig. 4.19. The I-beam is attracted to the C-core, therefore pushing the I-box which then pushes against the F-bracket. The dimple extrusions of the I-box will press against the sensors. Each of the four sensors were calibrated individually with various weights and plotted to find out the sensitivity and offset required based on the voltage readings. Each sensor had slightly different sensitivities being 114.05, 115.38, 114.48, 114.91 mV/N, with an offset of -5.53 , -5.25 , -5.09 , -5.51 mV respectively. The experimental apparatus is shown in Figs. 4.20-4.21. These sensors are connected to a dSPACE DS1104 control board which reads the data and based off the voltage reading and the previous sensitivity analysis, the output force can then be evaluated.

To position the I-beam in various angular disturbance cases, a modular I-box design was built where the backing can be switched out for different cases and 3D-printed, as shown in Fig.4.22.

For Case 0F a filleted C-Core is utilized as shown in Fig. 4.23b along with the standard non-filleted design in 4.23a. The experimental results were then compared with the analytical solution to verify the equations as shown in Fig. 4.24-4.28. The results show relatively good matching with the analytical solutions for each of the

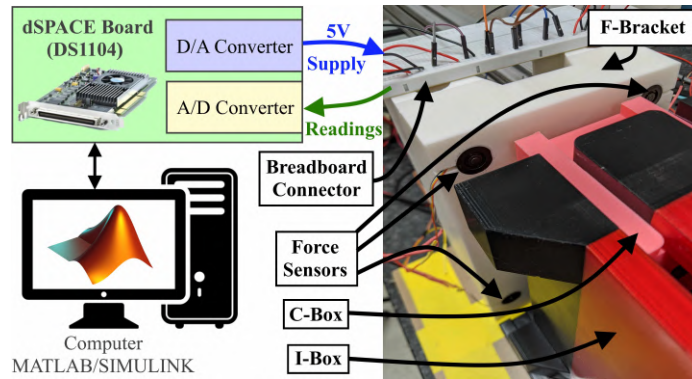


Figure 4.20: The experimental setup is shown with the 3D printed components F-Bracket, C-Box, and I-Box along with the 4 force sensors connected to the breadboard that is then connected to the dSPACE board (DS1104).

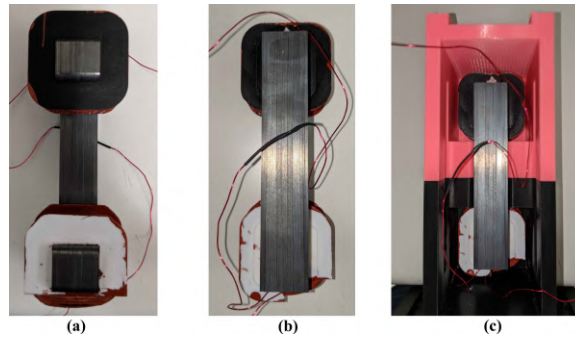


Figure 4.21: The (a) front, (b) back of C-Core element with the coils are shown and an inside view (c) of the C-Core inside the C-Box.

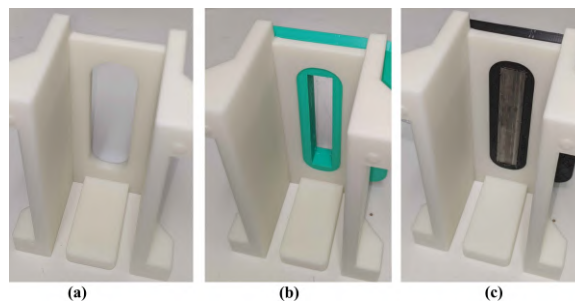


Figure 4.22: The modular I-box design (a) allows for certain I-beam cases to be inserted into the back (b), making experimenting easier for each case. The I-beam can then be inserted (c) and held in place with pins.

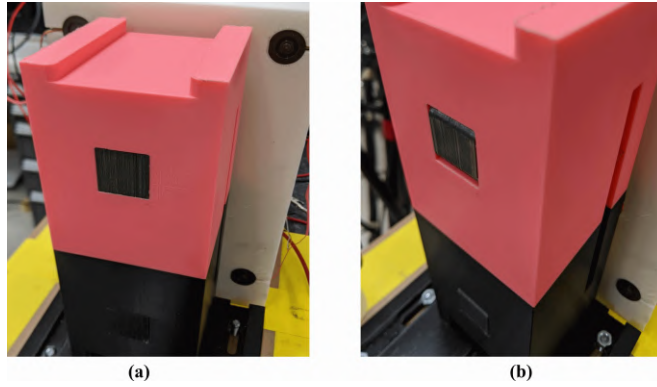


Figure 4.23: The C-Core setup (a) without fillets, and (b) with fillets.

cases. The experimental results are documented as force vs current as it was easier to adjust the input current during the experimentation rather than adjust the air gap displacement. All cases shown an error matching of less than 11.6%, with error shown to relatively decrease at higher forces. Some sources of potential error include systematic errors in the current measurements or force readings, 3D printing inaccuracies, hysteretic nonlinearities, flux fringing, and random errors from temperature variations.

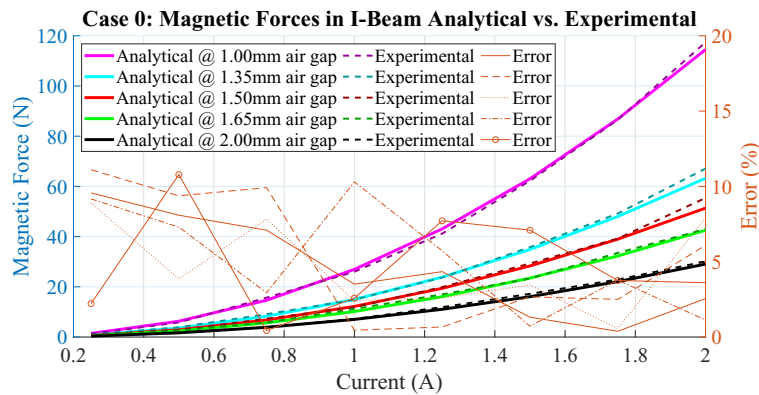


Figure 4.24: The experimental results are shown for Case 0 and compared to the analytical solution. The error is shown to be relatively low between the analytical and experimental model with a maximum error of 11.1%.

Next, the experimental findings with comparison to the analytical model are shown

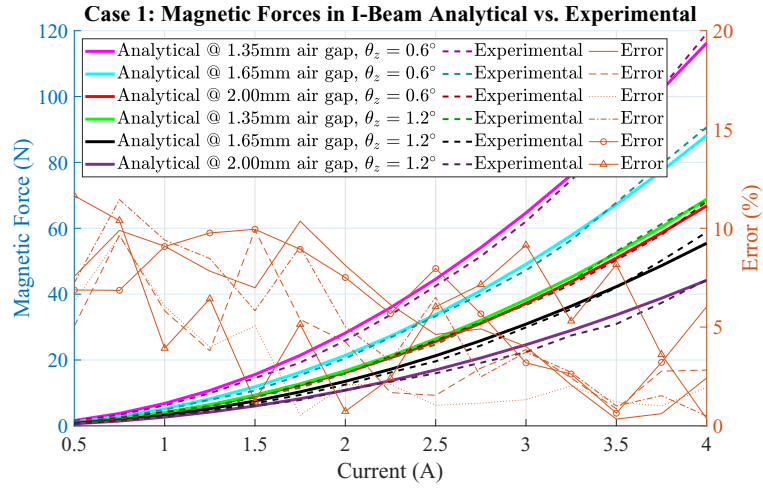


Figure 4.25: The experimental results are shown for Case 1 and compared to the analytical solution. The error is shown to be relatively low between the analytical and experimental model with a maximum error of 11.6%.

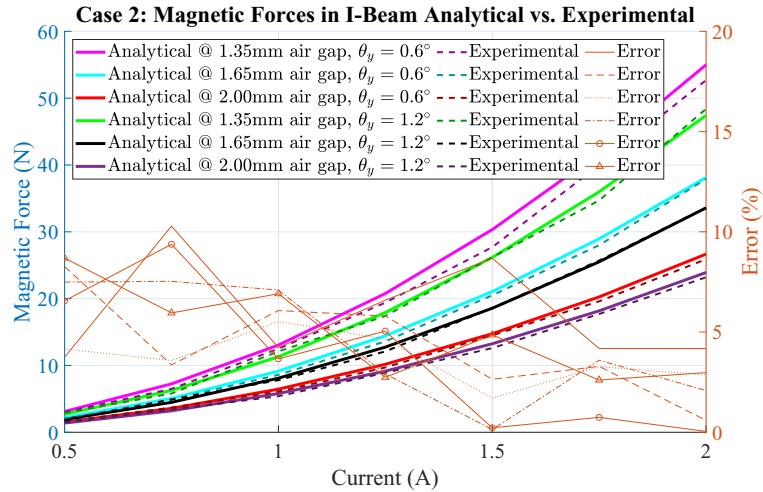


Figure 4.26: The experimental results are shown for Case 2 and compared to the analytical solution. The error is shown to be relatively low between the analytical and experimental model with a maximum error of 10.3%.

in Fig. 4.29. This shows that the analytical model can be used to evaluate forces when multi-axial offsets are considered and be within $\sim 10\%$.

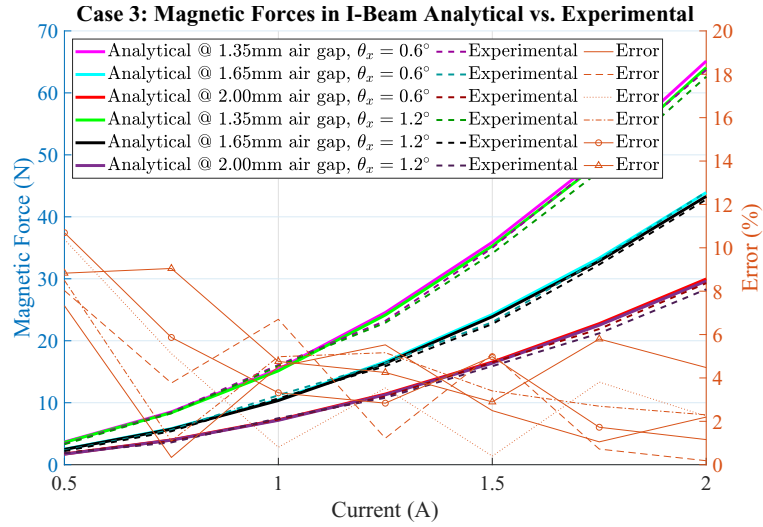


Figure 4.27: The experimental results are shown for Case 3 and compared to the analytical solution. The error is shown to be relatively low between the analytical and experimental model with a maximum error of 10.7%.

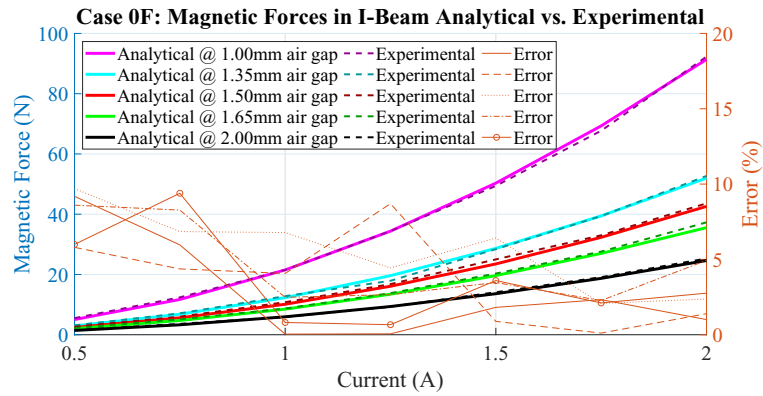


Figure 4.28: The experimental results are shown for Case 0F and compared to the analytical solution. The error is shown to be relatively low between the analytical and experimental model with a maximum error of 9.7%.

4.5 Discussion

The experimental model was found to match the analytical/FEA derived analytical equations for each case with an error below $\sim 11\%$. One key takeaway from the experiment was that the C-box enclosure could only take so much force before elastic deformation occurred, therefore, all cases besides Case 1, had to be limited to 2A

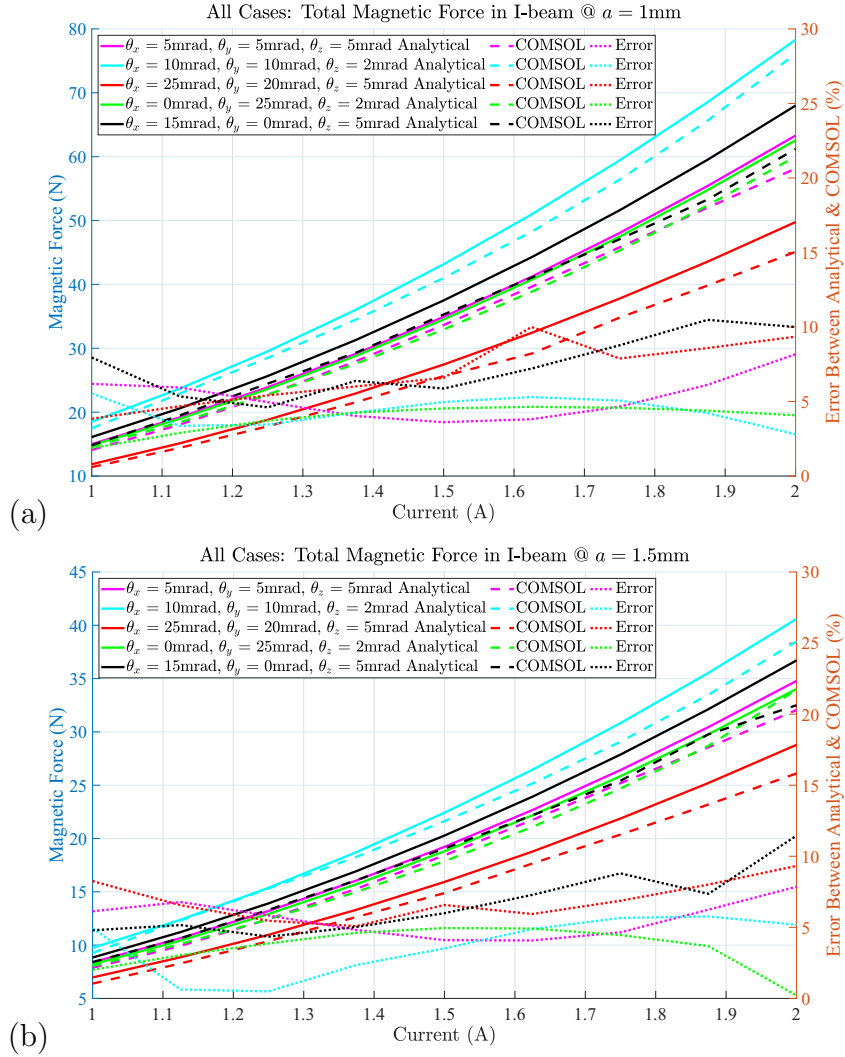


Figure 4.29: The analytical and experimental results for the multi-axis Case 1+2+3, are shown for (a) $a = 1\text{mm}$, (b) $a = 1.5\text{mm}$ to match with a maximum error of (a) 10.5%, (b) 11.4% for a range of 1-2A of current.

of current since the output forces were too high. A stronger material or a different design could extend the force range. Another takeaway is that Case 3 is very similar to that of Case 0, since angular offsets in the x axis has relatively small effects to the reluctance in the system as seen in 4.27. For all cases, an increase in angular offset decreases the overall output force of the RA as seen previously in Fig. 4.16. Case 1 is shown to have the greatest effect on the force since this case has the greatest effect on

the governing reluctance. Overall, using derived analytical equations combined with known FEA simulation results, allowed the force to be estimated within reasonable precision. The force sensors and displacement gauge used could also be improved for future experiments. Also, another consideration would be to use experimental data instead of FEA results for the 3D mapping correction factors to better match the real world system. However, experimental data may have systematic errors depending on the setup and precaution should be made. If the angular misalignment was not modelled, the positioning error can be off from the actual system depending on how drastic the angular offset is. The degree of error is shown previously in Fig. 4.16 where an offset of $\theta_z = 1^\circ$ is shown to reduce the overall force by approximately %90 which would change the dynamics of the system. Therefore it is important to model such angular offsets to obtain a more accurate RA model.

4.6 Conclusions of this Chapter

The next evolution of the photolithography machine requires a more efficient actuation system which can meet the high acceleration and precision demands in order to manufacture advanced semiconductor devices more efficiently and accurately. Currently, Lorentz actuators are utilized since they have a highly linear force-current dependency which leads to easier modelling and control. However, Lorentz actuators require efficient cooling systems because of thermal/power limitations. RAs on the other hand, can provide relatively high force output and are highly efficient, although they are harder to model due to their nonlinear nature. If there are any disturbances such as asymmetries, the force output can be significantly changed. This chapter has highlighted a successful method to model the forces when the mover parts of the C-core RA experiences various angular disturbances or if non-typical modelling needs

to be performed such as a filleted design. The method uses data obtained from FEA models from the COMSOL software to correct the rough derivations for each disturbance case using polynomial curve fitting which can predict the complex physics. The models were then found to match relatively well (within $\sim 11\%$) with the experimental findings. The results will enhance the development of control systems for precision motion systems to overcome these asymmetrical air gap disturbances. Future studies on machine learning of the FEA data will be conducted to better predict various cases of disturbances in the system followed by a feedforward control to improve the motion control of reluctance actuated systems. Also, multi-axis disturbances will be considered simultaneously such as having asymmetrical offsets in all angular degrees of freedom and a general analytical solution will be found.

Chapter 5

Conclusions and Future Work

This thesis provides background information and a review of the reluctance actuator (RA). It also showcases the importance of taking into account the mean path length (MPL) and asymmetrical air gaps between the mover and stator for multi-axial offset cases.

The RA mover accelerates because the stator generates the magnetic flux that produces an attractive magnetic attraction between the stator and mover. Hysteresis and other non-linearities in the magnetic flux have an impact on the force and have a nonlinear gap dependency. It is demonstrated that the RA has the capacity to produce a force that is effective and suitable for millimeter-range high-acceleration applications.

The RA is available in a wide variety of configurations, such as C-Core, E-Core, Hybrid, and Plunger-type designs. As seen in Chapter 2, each design offers certain advantages. The RA's complicated non-linear character and the need for precise models and controls to help linearize the RA system are its key problems. Hybrid dynamical models have been used by several researchers to accurately describe the

impacts of hysteresis, flux fringing, and eddy currents in order to advance the RA and find strategies to mitigate this nonlinear behaviour. The primary intended use is for photolithography machines, where great precision and acceleration are essential for the short-stroke stage.

This thesis also outlines a successful procedure in determining and modeling the force output for the RA when there are multi-axial offsets present in the system. This is important since the mover is mechanically separated from the stator and therefore some asymmetries can occur in the air gap separation which can affect the overall force output. It is very important to understand these effects and model it accurately to have a better control system. The derived analytical model was found to match experimental findings (within $\sim 10\%$). The experiment was performed by designing a 3D printed apparatus to allow for force measurements to be conducted on the RA system at specific air gap displacements and input currents. The design also allowed for various cases of angular offsets to be examined. The findings will improve the design of precision motion systems and their related control performance to eliminate these asymmetrical air gap disturbances.

Future research work will be to develop an artificial intelligence (AI) data-driven high-precision control system for semiconductor manufacturing lithography machines. AI has proven to be an effective tool to solve complex multistage decision-making problems [125]. It can be utilized under the assumption of having dynamics of unknown and nonlinear nature, while maintaining the desired throughput dictated by the supplied reference trajectories. AI can learn and evolve its controller parameters in real time to achieve the best performance for the motion stages in wafer scanners with the use of reinforcement learning [126, 127]. AI neural networks resemble a human brain and are built from layers of nodes or artificial neurons [128]. These networks rely on historical data to improve their accuracy over time and allow data to

be classified and optimized through received data. The main challenge with current wafer scanners is the nonlinearities and unknown dynamics that are encountered. With the use of AI, a prediction and mitigation algorithm can be developed that works on past performance measurements to learn and overcome these unknown dynamics and nonlinearities in wafer scanners [129, 130]. AI has been shown to exhibit better error reduction when compared to conventional control algorithms with the ability to counteract nonlinear disturbances more effectively, increasing overall system accuracy [131–133]. With better control systems for lithography machines it will lead to more affordable and better computational devices for the world as society progresses. If successful, this will include a timely contribution to the classical optimal control theory and will extend its application to other AI applications. This will enable lithography technology to produce smarter, and lighter integrated circuits faster which leads to the improved development of a wide variety of new technologies that have an essential role in daily life, including transportation, personal computers, mobile phones, and autonomous systems.

Bibliography

- [1] C. W. T. McLyman, *Transformer and inductor design handbook*. CRC press, 2004.
- [2] I. MacKenzie, “Design and control methods for high-accuracy variable reluctance actuators,” Ph.D. dissertation, Massachusetts Institute of Technology, 2015.
- [3] N. Vrijsen, J. Jansen, and E. Lomonova, “Comparison of linear voice coil and reluctance actuators for high-precision applications,” 10 2010, pp. S3–29.
- [4] A. van Lievenoogen, A. Toma, and U. Ummethala, “Challenges in the application of hybrid reluctance actuators in scanning positioning stages in vacuum with nanometer accuracy and mgauss magnetic stray field,” in *2013 American Control Conference*, 2013, pp. 5286–5289.
- [5] M. Pumphrey, N. Alatawneh, and M. Al Janaideh, “Modeling and analysis of reluctance motion system with asymmetrical air gaps,” *Review of Scientific Instruments*, vol. 93, no. 7, p. 075001, 2022.
- [6] M. Pumphrey, M. Al Saaideh, K. Kuchinka, N. Alatawneh, and M. Al, “Investigating the effect of the mean path length on reluctance actuator output force characterization.”

- [7] A. Katalenic, “Control of reluctance actuators for high-precision positioning,” Ph.D. dissertation, Electrical Engineering, 2013.
- [8] T. Kiong and S. Huang, *Modeling and Control of Precision Actuators*. <https://doi.org/10.1201/9781315216270>: CRC Press, 04 2016.
- [9] F. Cigarini, E. Csencsics, J. Schlarp, S. Ito, and G. Schitter, “Multiphysics finite element model for the computation of the electro-mechanical dynamics of a hybrid reluctance actuator,” *Mathematical and Computer Modelling of Dynamical Systems*, vol. 26, no. 4, pp. 322–343, 2020.
- [10] E. Csencsics, J. Schlarp, T. Schopf, and G. Schitter, “Compact high performance hybrid reluctance actuated fast steering mirror system,” *Mechatronics*, vol. 62, p. 102251, 10 2019.
- [11] E. Csencsics, J. Schlarp, and G. Schitter, “High-performance hybrid-reluctance-force-based tip/tilt system: Design, control, and evaluation,” *IEEE/ASME Transactions on Mechatronics*, vol. PP, pp. 1–1, 08 2018.
- [12] —, “Bandwidth extension of hybrid-reluctance-force-based tip/tilt system by reduction of eddy currents,” 07 2017, pp. 1167–1172.
- [13] M. Steinbuch, T. Oomen, and H. Vermeulen, “Motion control, mechatronics design, and moore’s law,” *IEEJ Journal of Industry Applications*, vol. 11, 08 2021.
- [14] E. H. Maslen and G. Schweitzer, *Magnetic bearings: theory, design, and application to rotating machinery*. Springer, 2009.

- [15] S. Circosta, R. Galluzzi, N. Amati, A. Bonfitto, L. Castellanos Molina, and A. Tonoli, “Improved 1-d model for semi-hard magnetic material-based electromagnets,” 05 2019, pp. 870–874.
- [16] K. Ono, “Curved i-core,” U.S. Patent 4 741 207, Jun, 2005.
- [17] A. Katalenic, C. M. M. van Lierop, and P. Bosch, “On hysteresis and air gap disturbance in current and voltage mode feed-forward control of variable reluctance actuators,” *Journal of Applied Physics - J APPL PHYS*, pp. 1608–1613, 12 2011.
- [18] E. Moya-Lasheras and C. Sagues, “Run-to-run control with bayesian optimization for soft landing of short-stroke reluctance actuators,” *IEEE/ASME Transactions on Mechatronics*, vol. PP, pp. 1–1, 04 2020.
- [19] P. Holmberg, “Modelling the transient response of windings, laminated steel cores and electromagnetic power devices by means of lumped circuits : With special reference to windings with a coaxial insulation system,” 01 2000.
- [20] H. Nabae, A. Karaguzel, G. Endo, and K. Suzumori, “Analytical and experimental study on actuation time of displacement amplified electromagnetic actuator,” 07 2017, pp. 963–968.
- [21] L. Li, “Linearizing magnetic bearing actuators by constant current sum, constant voltage sum, and constant flux sum,” *IEEE Transactions on Magnetics*, vol. 35, no. 1, pp. 528–535, 1999.
- [22] L. Zhou and L. Li, “Modeling and identification of a solid-core active magnetic bearing including eddy currents,” *IEEE/ASME Transactions on Mechatronics*, vol. 21, pp. 1–1, 12 2016.

- [23] A. Katalenic, J. De Boeij, H. Butler, and P. Van Den Bosch, "Linearization of a current-driven reluctance actuator with hysteresis compensation," *Mechatronics*, vol. 23, no. 2, pp. 163–171, 2013.
- [24] A. Katalenic, H. Butler, and P. P. Van Den Bosch, "High-precision force control of short-stroke reluctance actuators with an air gap observer," *IEEE/ASME Transactions on Mechatronics*, vol. 21, no. 5, pp. 2431–2439, 2016.
- [25] A. Katalenic, "Voltage based linearization of a reluctance actuator for high-precision applications," 04 2013, pp. 170–176.
- [26] Y.-P. Liu, K.-Z. Liu, and Y. Xiaofeng, "Nonlinear current control for reluctance actuator with hysteresis compensation," *Journal of Control Science and Engineering*, vol. 2014, 10 2014.
- [27] Y. Liu, K.-Z. Liu, and X. Yang, "Hysteresis compensation control for a current-driven reluctance actuator using the adaptive mnn," *Applied Mechanics and Materials*, vol. 643, pp. 60–65, 09 2014.
- [28] T. Braun, J. Reuter, and J. Rudolph, "Observer design for self-sensing of solenoid actuators with application to soft landing," *IEEE Transactions on Control Systems Technology*, vol. 27, no. 4, pp. 1720–1727, 2019.
- [29] Q.-s. CHEN, X.-f. YANG, and L.-w. WU, "Acceleration feedback in a stage having paired reluctance linear actuator with hysteresis," *DEStech Transactions on Engineering and Technology Research*, 03 2017.
- [30] D. Trumper, S. Olson, and P. Subrahmanyam, "Linearizing control of magnetic suspension systems," *IEEE Transactions on Control Systems Technology*, vol. 5, no. 4, pp. 427–438, 1997.

- [31] N. Vrijsen, J. Jansen, J. Compter, and E. Lomonova, "Measurement method for determining the magnetic hysteresis effects of reluctance actuators by evaluation of the force and flux variation," *The Review of scientific instruments*, vol. 84, p. 075003, 07 2013.
- [32] Y. Xu, X. Li, X. Yang, Z. Yang, L. Wu, and Q. Chen, "A two-stage model for rate-dependent inverse hysteresis in reluctance actuators," *Mechanical Systems and Signal Processing*, vol. 135, p. 106427, 2020.
- [33] I. MacKenzie and D. L. Trumper, "Real-time hysteresis modeling of a reluctance actuator using a sheared-hysteresis-model observer," *IEEE/ASME Transactions on Mechatronics*, vol. 21, no. 1, pp. 4–16, 2016.
- [34] J. Cale, S. Sudhoff, and L.-Q. Tan, "Accurately modeling ei core inductors using a high-fidelity magnetic equivalent circuit approach," *Magnetics, IEEE Transactions on*, vol. 42, pp. 40 – 46, 02 2006.
- [35] N. Vrijsen, J. Jansen, and E. Lomonova, "Prediction of magnetic hysteresis in the force of a pre-biased e-core reluctance actuator," vol. 50, 05 2013.
- [36] —, "Prediction of magnetic hysteresis in the force of a prebiased e-core reluctance actuator," *IEEE Transactions on Industry Applications*, vol. PP, pp. 1–1, 01 2014.
- [37] J. Lindlau and C. Knospe, "Feedback linearization of an active magnetic bearing with voltage control," *Control Systems Technology, IEEE Transactions on*, vol. 10, pp. 21 – 31, 02 2002.

- [38] Y.-P. Liu, K.-Z. Liu, and X. Yang, “Hysteresis compensation control for reluctance actuator force using neural network,” in *Proceedings of the 32nd Chinese Control Conference*. IEEE, 2013, pp. 3354–3359.
- [39] Q. Miao, Y. Liu, and J. Tan, “Precision flux control of linear reluctance actuator using the integral sliding mode method,” *Frontiers in Energy Research*, vol. 10, 08 2022.
- [40] S. A. J. Hol, “Actuator, positioning system and lithographic apparatus,” Jun 2013.
- [41] E. Ramirez-Laboreo, E. Moya-Lasheras, and C. Sagues, “Optimal open-loop control policies for a class of nonlinear actuators,” 06 2019.
- [42] —, “Real-time electromagnetic estimation for reluctance actuators,” *IEEE Transactions on Industrial Electronics*, vol. 66, no. 3, pp. 1952–1961, 2019.
- [43] J. van Dam, B. Gysen, E. Lomonova, and M. Dhaens, “Soft-landing control of low-energy solenoid valve actuators,” 04 2018, pp. 1–5.
- [44] J. Bao, N. Vrijsen, B. Gysen, R. Sprangers, and E. Lomonova, “Optimization of the force density for medium-stroke reluctance actuators,” *IEEE Transactions on Industry Applications*, vol. 50, pp. 3194–3202, 09 2014.
- [45] R. Clark, G. Jewell, P. Stewart, and D. Howe, “Tailoring force-displacement characteristics in medium-stroke linear variable reluctance actuators,” *Magnetics, IEEE Transactions on*, vol. 38, pp. 3267 – 3269, 10 2002.
- [46] E. Moya-Lasheras, C. Sagues, E. Ramirez-Laboreo, and S. Llorente, “Nonlinear bounded state estimation for sensorless control of an electromagnetic device,” 12 2017.

- [47] E. Ramirez-Laboreo and C. Sagues, “Reluctance actuator characterization via fem simulations and experimental tests,” *Mechatronics*, vol. 56, pp. 58–66, 12 2018.
- [48] E. Ramirez-Laboreo, M. Roes, and C. Sagues, “Hybrid dynamical model for reluctance actuators including saturation, hysteresis and eddy currents,” *IEEE/ASME Transactions on Mechatronics*, vol. 24, pp. 1396–1406, 06 2019.
- [49] D. Wu, X. Xie, and S. Zhou, “Design of a normal stress electromagnetic fast linear actuator,” *Magnetics, IEEE Transactions on*, vol. 46, pp. 1007 – 1014, 05 2010.
- [50] X. Zhang, L. Lai, L. Zhang, and L. Zhu, “Hysteresis and magnetic flux leakage of long stroke micro/nanopositioning electromagnetic actuator based on maxwell normal stress,” *Precision Engineering*, vol. 75, 01 2022.
- [51] S. Ito, F. Cigarini, and G. Schitter, “Flux-controlled hybrid reluctance actuator for high-precision scanning motion,” *IEEE Transactions on Industrial Electronics*, vol. 67, no. 11, pp. 9593–9600, 2020.
- [52] F. Cigarini, S. Ito, J. Konig, A. Sinn, and G. Schitter, “Compensation of hysteresis in hybrid reluctance actuator for high-precision motion,” *IFAC-PapersOnLine*, vol. 52, pp. 477–482, 01 2019.
- [53] S. Ito, S. Troppmair, B. Lindner, F. Cigarini, and G. Schitter, “Long-range fast nanopositioner using nonlinearities of hybrid reluctance actuator for energy efficiency,” *IEEE Transactions on Industrial Electronics*, vol. 66, no. 4, pp. 3051–3059, 2019.

- [54] F. Cigarini, S. Ito, S. Troppmair, and G. Schitter, “Comparative finite element analysis of a voice coil actuator and a hybrid reluctance actuator,” *IEEE Journal of Industry Applications*, vol. 8, pp. 192–199, 03 2019.
- [55] X. Zhang, L. Lai, L. Zhang, and L. Zhu, “Hysteresis and magnetic flux leakage of long stroke micro/nanopositioning electromagnetic actuator based on maxwell normal stress,” *Precision Engineering*, vol. 75, pp. 1–11, 2022. [Online]. Available: <https://www.sciencedirect.com/science/article/pii/S0141635922000034>
- [56] X. Zhang, L. Lai, P. Li, and L.-M. Zhu, “Data-driven fractional order feedback and model-less feedforward control of a xy reluctance-actuated micropositioning stage,” *Review of Scientific Instruments*, vol. 93, no. 11, p. 115002, 2022.
- [57] X. Zhang, L.-J. Lai, and L.-M. Zhu, “Data-driven fractional order phase-lead and proportional–integral feedback control strategy with application to a reluctance-actuated compliant micropositioning system,” *Sensors and Actuators A: Physical*, vol. 348, p. 113988, 2022. [Online]. Available: <https://www.sciencedirect.com/science/article/pii/S0924424722006239>
- [58] F. Cigarini, E. Csencsics, J. Schlarp, S. Ito, and G. Schitter, “Multiphysics finite element model for the computation of the electro-mechanical dynamics of a hybrid reluctance actuator,” *Mathematical and Computer Modelling of Dynamical Systems*, 05 2020.
- [59] G. Eaglin and J. Vaughan, “Model reference control with command shaping for a micro-electromagnetic actuator with input constraints,” 10 2019.

- [60] H. Nabae and T. Higuchi, “A novel electromagnetic actuator based on displacement amplification mechanism,” *IEEE/ASME Transactions on Mechatronics*, vol. 20, no. 4, pp. 1607–1615, 2015.
- [61] G. Stadler, E. Csencsics, S. Ito, and G. Schitter, “High precision hybrid reluctance actuator with integrated orientation independent zero power gravity compensation,” *IEEE Transactions on Industrial Electronics*, 2021.
- [62] R. Boll, “Soft magnetic materials : fundamentals, alloys, properties, products, applications : the vacuumschmelze handbook,” 1979.
- [63] E. Moya-Lasheras, C. Sagues, and S. Llorente, “An efficient dynamical model of reluctance actuators with flux fringing and magnetic hysteresis,” *Mechatronics*, vol. 74, p. 102500, 2021.
- [64] X. Lu, “Electromagnetically-driven ultra-fast tool servo for diamond turning,” Ph.D. dissertation, Massachusetts Institute of Technology, 2005.
- [65] A. Popović, B. Bojović, M. Suter, and D. Niederer, “Design parameters effect to magnetic flux distribution of the reluctance actuator,” *FME Transactions*, vol. 48, no. 3, pp. 504–510, 2020.
- [66] E. Ramirez-Laboreo, “Modeling and control of reluctance actuators,” Ph.D. dissertation, 10 2019.
- [67] E. Moya-Lasheras, E. Ramirez-Laboreo, and C. Sagues, “Probability-based optimal control design for soft landing of short-stroke actuators,” *IEEE Transactions on Control Systems Technology*, vol. 28, no. 5, pp. 1956–1963, 2020.
- [68] E. Moya-Lasheras, J. M. Schellekens, and C. Sagüés, “Rauch-tung-striebel smoother for position estimation of short-stroke reluctance actuators,” *IEEE*

- Trans. Control. Syst. Technol.*, vol. 30, no. 4, pp. 1641–1653, 2022. [Online]. Available: <https://doi.org/10.1109/TCST.2021.3120909>
- [69] D. L. Trumper, “Nonlinear compensation techniques for magnetic suspension systems,” *NASA, Langley Research Center, Aerospace Applications of Magnetic Suspension Technology, Part 2*, 1991.
- [70] I. Burgstaller, S. Ito, H. Fujimoto, and G. Schitter, “Development of reluctance actuator for high-precision positioning and scanning motion,” in *2021 IEEE International Conference on Mechatronics (ICM)*, 2021, pp. 1–6.
- [71] I. Rotariu, B. Dijkstra, and M. Steinbuch, “Standard and lifted approaches of iterative learning control applied on a motion system,” 01 2004.
- [72] L. O. Chua and K. A. Stromsmoe, “Mathematical model for dynamic hysteresis loops,” *International Journal of Engineering Science*, vol. 9, no. 5, pp. 435–450, 1971. [Online]. Available: <https://www.sciencedirect.com/science/article/pii/0020722571900462>
- [73] D. Jiles and D. Atherton, “Ferromagnetic hysteresis,” *IEEE Transactions on Magnetics*, vol. 19, no. 5, pp. 2183–2185, 1983.
- [74] D. Helmick and W. Messner, “Higher order modeling of hysteresis in disk drive actuators,” in *42nd IEEE International Conference on Decision and Control (IEEE Cat. No.03CH37475)*, vol. 4, 2003, pp. 3712–3716 vol.4.
- [75] Q. Miao, Y. Liu, and J. B. Tan, “Precision flux control of linear reluctance actuator using the integral sliding mode method,” *Frontiers in Energy Research*, vol. 10, 2022. [Online]. Available: <https://www.frontiersin.org/articles/10.3389/fenrg.2022.949782>

- [76] W. S. Galinaitis, “Two methods for modeling scalar hysteresis and their use in controlling actuators with hysteresis,” 1999.
- [77] F. Ikhouane, “A survey of the hysteretic duhem model,” *Archives of Computational Methods in Engineering*, vol. 25, no. 4, pp. 965–1002, Nov 2018. [Online]. Available: <https://doi.org/10.1007/s11831-017-9218-3>
- [78] S. Mittal and C.-H. Menq, “Hysteresis compensation in electromagnetic actuators through preisach model inversion,” *Mechatronics, IEEE/ASME Transactions on*, vol. 5, pp. 394 – 409, 01 2001.
- [79] I. Mayergoyz, “Mathematical models of hysteresis,” *Magnetics, IEEE Transactions on*, vol. 22, pp. 603 – 608, 10 1986.
- [80] V. Hassani, T. Tjahjowidodo, and T. N. Do, “A survey on hysteresis modeling, identification and control,” *Mechanical Systems and Signal Processing*, vol. 49, 12 2014.
- [81] M. Al Janaideh, J. Mao, S. Rakheja, W. Xie, and C.-Y. Su, “Generalized prandtl-ishlinskii hysteresis model: Hysteresis modeling and its inverse for compensation in smart actuators,” in *2008 47th IEEE Conference on Decision and Control*, 2008, pp. 5182–5187.
- [82] M. Brokate and J. Sprekels, *Hysteresis and phase transitions*. Springer Science & Business Media, 1996, vol. 121.
- [83] L. Chua and S. Bass, “A generalized hysteresis model,” *IEEE Transactions on Circuit Theory*, vol. 19, no. 1, pp. 36–48, 1972.

- [84] M. Loganathan, A. Al-Ogaidi, and D. A. Bristow, “Design and control of a dual-probe atomic force microscope,” *IEEE/ASME Transactions on Mechatronics*, vol. 23, no. 1, pp. 424–433, 2017.
- [85] B. Voigtländer, V. Cherepanov, S. Korte, A. Leis, D. Cuma, S. Just, and F. Lüpke, “Invited review article: Multi-tip scanning tunneling microscopy: Experimental techniques and data analysis,” *Review of scientific instruments*, vol. 89, no. 10, pp. 1–23, 2018.
- [86] A. Katalenic, H. Butler, and P. P. van den Bosch, “High-precision force control of short-stroke reluctance actuators with an air gap observer,” *IEEE/ASME Transactions on Mechatronics*, vol. 21, no. 5, pp. 2431–2439, 2016.
- [87] M. Lahdo, T. Ströhla, and S. Kovalev, “Design and implementation of an new 6-dof magnetic levitation positioning system,” *IEEE Transactions on Magnetics*, vol. 55, no. 12, pp. 1–7, 2019.
- [88] R.-H. M. Schmidt, “Ultra-precision engineering in lithographic exposure equipment for the semiconductor industry,” *Philosophical Transactions of the Royal Society A: Mathematical, Physical and Engineering Sciences*, vol. 370, no. 1973, pp. 3950–3972, 2012.
- [89] X. Wu, S. Chen, W. Chen, M. Yang, and W. Fu, “Large angle and high linearity two-dimensional laser scanner based on voice coil actuators,” *Review of Scientific Instruments*, vol. 82, no. 10, pp. 1–7, 2011.
- [90] M. Steinbuch, T. Oomen, and H. Vermeulen, “Motion control, mechatronics design, and Moore’s law,” *IEEJ Journal of Industry Applications*, pp. 1–11, 2021.

- [91] T. Tuma, W. Haeberle, H. Rothuizen, J. Lygeros, A. Pantazi, and A. Sebastian, “Dual-stage nanopositioning for high-speed scanning probe microscopy,” *IEEE/ASME Transactions on Mechatronics*, vol. 19, no. 3, pp. 1035–1045, 2013.
- [92] D. B. Hiemstra, G. Parmar, and S. Awtar, “Performance tradeoffs posed by moving magnet actuators in flexure-based nanopositioning,” *IEEE/ASME Transactions on Mechatronics*, vol. 19, no. 1, pp. 201–212, 2012.
- [93] I. MacKenzie and D. L. Trumper, “Real-time hysteresis modeling of a reluctance actuator using a sheared-hysteresis-model observer,” *IEEE/ASME Transactions on Mechatronics*, vol. 21, no. 1, pp. 4–16, 2016.
- [94] M. Al Saaideh, N. Alatawneh, and M. Al Janaideh, “Multi-objective optimization of a reluctance actuator for precision motion applications,” *Journal of Magnetism and Magnetic Materials*, vol. 546, pp. 1–16, 2022.
- [95] —, “Design parameters of a reluctance actuation system for stable operation conditions with applications of high-precision motions in lithography machines,” *IET Electric Power Applications*, vol. 16, no. 1, pp. 68–85, 2022.
- [96] N. Vrijsen, J. Jansen, and E. Lomonova, “Comparison of linear voice coil and reluctance actuators for high-precision applications,” in *Proceedings of 14th International Power Electronics and Motion Control Conference EPE-PEMC 2010*, 2010, pp. 29–36.
- [97] T. Oomen, R. van Herpen, S. Quist, M. van de Wal, O. Bosgra, and M. Steinbuch, “Connecting system identification and robust control for next-generation motion control of a wafer stage,” *IEEE Transactions on Control Systems Technology*, vol. 22, no. 1, pp. 102–118, 2013.

- [98] T. Braun, J. Reuter, and J. Rudolph, “Observer design for self-sensing of solenoid actuators with application to soft landing,” *IEEE Transactions on Control Systems Technology*, vol. 27, no. 4, pp. 1720–1727, 2018.
- [99] Y. Xu, X. Li, X. Yang, Z. Yang, L. Wu, and Q. Chen, “A two-stage model for rate-dependent inverse hysteresis in reluctance actuators,” *Mechanical Systems and Signal Processing*, vol. 135, pp. 1–18, 2020.
- [100] A. Popović, B. Bojović, M. Suter, and D. Niederer, “Design parameters effect to magnetic flux distribution of the reluctance actuator,” *FME Transactions*, vol. 48, no. 3, pp. 504–510, 2020.
- [101] F. Cigarini, E. Csencsics, J. Schlarp, S. Ito, and G. Schitter, “Multiphysics finite element model for the computation of the electro-mechanical dynamics of a hybrid reluctance actuator,” *Mathematical and Computer Modelling of Dynamical Systems*, vol. 26, no. 4, pp. 322–343, 2020.
- [102] E. Ramirez-Laboreo, C. Sagues, and S. Llorente, “A new model of electromechanical relays for predicting the motion and electromagnetic dynamics,” *IEEE Transactions on Industry Applications*, vol. 52, no. 3, pp. 2545–2553, 2016.
- [103] I. Burgstaller, S. Ito, H. Fujimoto, and G. Schitter, “Development of reluctance actuator for high-precision positioning and scanning motion,” in *Proceedings of 2021 IEEE International Conference on Mechatronics (ICM)*, 2021, pp. 1–6.
- [104] E. Ramirez-Laboreo and C. Sagues, “Reluctance actuator characterization via fem simulations and experimental tests,” *Mechatronics*, vol. 56, pp. 58–66, 2018.

- [105] E. Moya-Lasheras, C. Sagues, and S. Llorente, “An efficient dynamical model of reluctance actuators with flux fringing and magnetic hysteresis,” *Mechatronics*, vol. 74, pp. 1–10, 2021.
- [106] I. MacKenzie and D. L. Trumper, “Real-time hysteresis modeling of a reluctance actuator using a sheared-hysteresis-model observer,” *IEEE/ASME Transactions on Mechatronics*, vol. 21, no. 1, pp. 4–16, 2016.
- [107] A. Katalenic, J. Boeij, de, H. Butler, and P. Bosch, van den, “Linearization of a current-driven reluctance actuator with hysteresis compensation,” *Mechatronics*, vol. 23, no. 2, pp. 163–171, 2013.
- [108] N. Vrijsen, J. Jansen, J. Compter, and E. Lomonova, “Measurement method for determining the magnetic hysteresis effects of reluctance actuators by evaluation of the force and flux variation,” *The Review of scientific instruments*, vol. 84, p. 075003, 07 2013.
- [109] Proto Lam LLC., “Material properties spreadsheet,” [Online], Available: <http://www.protolam.com/page5.html>, 2017.
- [110] H. Butler, “Position control in lithographic equipment,” *IEEE Control Systems Magazine*, vol. 31, no. 5, pp. 28–47, 2011.
- [111] Y. Otsu, K. Somaya, and S. Yoshimoto, “High-speed stability of a rigid rotor supported by aerostatic journal bearings with compound restrictors,” *Tribology International*, vol. 44, no. 1, pp. 9–17, 2011.
- [112] R. Dupont, “Robust rotor dynamics for high-speed air bearing spindles,” *Precision Engineering*, vol. 40, pp. 7–13, 2015.

- [113] Y. Ye, X. Chen, Y. Hu, and X. Luo, “Effects of recess shapes on pneumatic hammering in aerostatic bearings,” *Proceedings of the Institution of Mechanical Engineers, Part J: Journal of Engineering Tribology*, vol. 224, no. 3, pp. 231–237, 2010.
- [114] T. Aoyama, K. Koizumi, Y. Kakinuma, and Y. Kobayashi, “Numerical and experimental analysis of transient state micro-bounce of aerostatic guideways caused by small pores,” *CIRP annals*, vol. 58, no. 1, pp. 367–370, 2009.
- [115] R. J. Meléndez H., “A reluctance actuator gap disturbance testbed,” Master’s thesis, Massachusetts Institute of Technology, 2014.
- [116] E. Moya-Lasheras, C. Sagues, and S. Llorente, “An efficient dynamical model of reluctance actuators with flux fringing and magnetic hysteresis,” *Mechatronics*, vol. 74, p. 102500, 04 2021.
- [117] N. Vrijsen, J. Jansen, and E. Lomonova, “Comparison of linear voice coil and reluctance actuators for high-precision applications,” 10 2010, pp. S3–29.
- [118] I. Burgstaller, S. Ito, H. Fujimoto, and G. Schitter, “Development of reluctance actuator for high-precision positioning and scanning motion,” in *2021 IEEE International Conference on Mechatronics (ICM)*, 2021, pp. 1–6.
- [119] S. Ito, F. Cigarini, and G. Schitter, “Flux-controlled hybrid reluctance actuator for high-precision scanning motion,” *IEEE Transactions on Industrial Electronics*, vol. 67, no. 11, pp. 9593–9600, 2020.
- [120] A. Katalenic, H. Butler, and P. P. J. van den Bosch, “High-precision force control of short-stroke reluctance actuators with an air gap observer,” *IEEE/ASME Transactions on Mechatronics*, vol. 21, no. 5, pp. 2431–2439, 2016.

- [121] N. H. Vrijsen, J. W. Jansen, and E. A. Lomonova, “Prediction of magnetic hysteresis in the force of a pre-biased e-core reluctance actuator,” in *2013 International Electric Machines Drives Conference*, 2013, pp. 1450–1457.
- [122] R. Schmidt, G. Schitter, A. Rankers, and J. Eijk, *The Design of High Performance Mechatronics: High-Tech Functionality by Multidisciplinary System Integration*, 3rd ed., 02 2020.
- [123] E. Ramirez-Laboreo, M. Roes, and C. Sagues, “Hybrid dynamical model for reluctance actuators including saturation, hysteresis and eddy currents,” *IEEE/ASME Transactions on Mechatronics*, vol. 24, pp. 1396–1406, 06 2019.
- [124] *FX29 Compact Compression Load Cell*, TE, 2020.
- [125] D. Bertsekas, *Dynamic programming and optimal control: Volume I*. Athena scientific, 2012, vol. 1.
- [126] B. Recht, “A tour of reinforcement learning: The view from continuous control,” *arXiv preprint arXiv:1806.09460*, 2018.
- [127] T. Bian, Y. Jiang, and Z.-P. Jiang, “Adaptive dynamic programming and optimal control of nonlinear nonaffine systems,” *Automatica*, vol. 50, no. 10, pp. 2624–2632, 2014.
- [128] S. Walczak and N. Cerpa, “Artificial neural networks,” in *Encyclopedia of Physical Science and Technology (Third Edition)*, third edition ed., R. A. Meyers, Ed. New York: Academic Press, 2003, pp. 631–645. [Online]. Available: <https://www.sciencedirect.com/science/article/pii/B0122274105008371>

- [129] D. P. Bertsekas and J. N. Tsitsiklis, “Neuro-dynamic programming: an overview,” in *Proceedings of 1995 34th IEEE conference on decision and control*, vol. 1. IEEE, 1995, pp. 560–564.
- [130] M. L. Puterman, *Markov decision processes: discrete stochastic dynamic programming*. John Wiley & Sons.
- [131] Y.-L. Yeh and P.-K. Yang, “Design and comparison of reinforcement-learning-based time-varying pid controllers with gain-scheduled actions,” *Machines*, vol. 9, no. 12, 2021. [Online]. Available: <https://www.mdpi.com/2075-1702/9/12/319>
- [132] D. Lee, S. Koo, I. Jang, and J. Kim, “Comparison of deep reinforcement learning and pid controllers for automatic cold shutdown operation,” *Energies*, vol. 15, p. 2834, 04 2022.
- [133] J. Conradt, “A comparison between a traditional pid controller and an artificial neural network controller in manipulating a robotic arm,” 2019.

Appendix A

Configurations and Setups of the Reluctance Actuator Examples

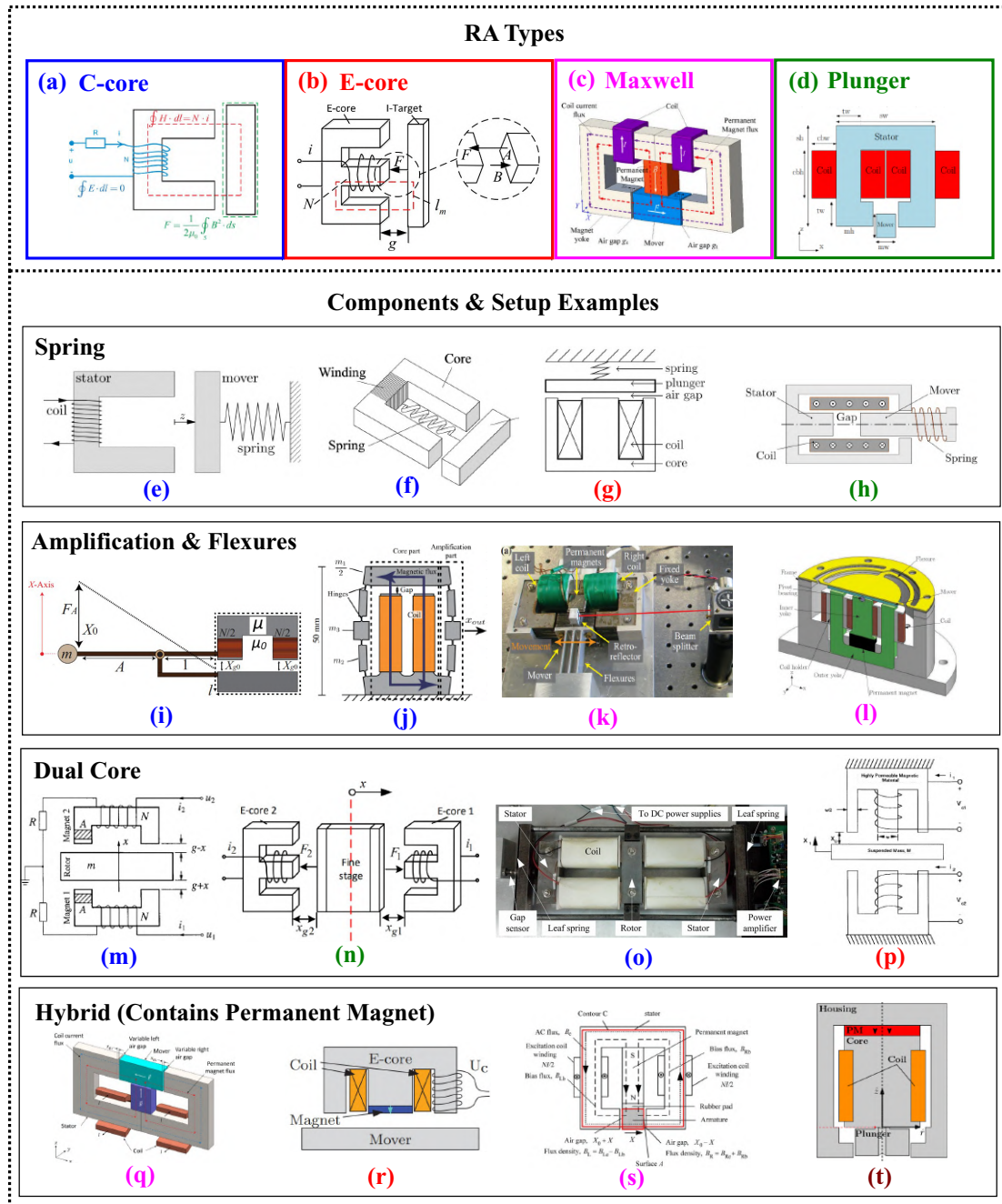


Figure A.1: The four standard types of RA are the (a) C-core [50], (b) E-core [26,27], (c) Maxwell [50], and (d) the plunger type [3]. Components can be added also such as springs in (e) [18], (f) [19], (g) [28], and (h) [41,42]. Mechanical amplification systems such as levers or flexures can be added such as (i) [20], (j) [59,60], (k) [51–53], and (l) [9–12]. Two RAs can be used for a dual-core setup as seen in (m) [21], (n) [29], (o) [22], and (p) [30] to allow bidirectional motion of the mover between the cores. Permanent magnets can be added for a hybrid setup which incorporates additional flux as shown in (q) [54], (r) [31], (s) [49], and (t) [43].